

NUMERICAL STUDY OF ELECTROMAGNETIC
SCATTERING FROM THREE-DIMENSIONAL
WATER WAVES

By

ZHIQIN ZHAO

Bachelor of Science
University of Electronic Science and Technology of China
Chengdu, China
1990

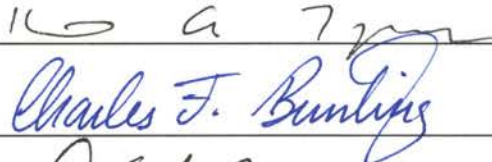
Master of Science
University of Electronic Science and Technology of China
Chengdu, China
1993

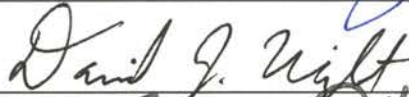
Submitted to the Faculty of
the Graduate College of the
Oklahoma State University
in Partial Fulfillment of
the Requirements for
the Degree of
DOCTOR OF PHILOSOPHY
December, 2002

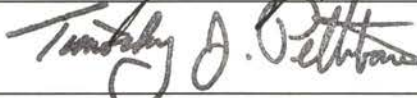
NUMERICAL STUDY OF ELECTROMAGNETIC
SCATTERING FROM THREE-DIMENSIONAL
WATER WAVES

Thesis Approved:


Thesis Advisor







Dean of the Graduate College

ACKNOWLEDGEMENTS

I wish to extend my sincere thanks and appreciation to my thesis advisor Dr. James C. West in Electrical Engineering Department of Oklahoma State University for his guidance, helpful suggestions, encouragement, and expertise. I would also like to thank my committee members, Dr. Keith A. Teague, Dr. Charles F. Bunting and Dr. David J. Wright, for their many helpful suggestions and support during this effort.

This dissertation is dedicated to my parents Junhua Zhao and Manxiu Yin, my parents in law Xiangfu Huang and Lianjie Chen, my wife Shen Huang and my son Pinyi. Their unfailing love and encouragement have inspired me to reach this goal. Thanks for their love, understanding and support!

This work is supported by the Office of Naval Research under grant N00014-00-1-0082 (program manager: Dr. Ronald Radlinski).

TABLE OF CONTENTS

1 INTRODUCTION	1
1.1 Breaking Wave Scattering	2
1.1.1 Definition of 2-D and 3-D Surfaces	4
1.1.2 Previous Work	5
1.1.3 Spilling Breaker Water Wave	6
1.1.4 Plunging Breaker Water Wave	11
1.2 Existing Scattering Models	11
1.2.1 Analytical Models	12
1.2.2 Numerical Methods	15
1.3 Edge Treatment in Numerical Methods	17
1.4 Overview	18
2 REVIEW OF NUMERICAL TECHNIQUE FOR 2-D SURFACES	19
2.1 Moment Method for Perfectly Conducting Surfaces	19
2.2 Moment Method for Imperfectly Conducting Surfaces	23
2.3 Hybrid MM/GTD Technique	26
2.4 2-D Scattering	28
2.4.1 Spilling Breaker	28
2.4.2 Plunging Breaker	29
3 REVIEW OF SCATTERING MODELS	31
3.1 Random Surface Generation- Pierson-Moskowitz Spectrum	32
3.1.1 Pierson-Moskowitz Spectrum	32
3.1.2 Generation of Sample Surfaces	34
3.2 Two Scale Model	34
3.2.1 Kirchhoff's Approximation	35
3.2.2 Small Perturbation Model	36
3.2.3 Two Scale Model	37
3.2.4 Application	40
3.3 Small Slope Approximation	41
3.4 Extended Geometrical Optics/Geometrical Theory of Diffraction	42
4 NUMERICAL CODE FOR 3-D SURFACE SCATTERING	46
4.1 Review of RWG Basis	46
4.1.1 Perfectly Conducting Surfaces	47
4.1.2 Numerical Implementation	50

4.1.3	Imperfectly Conducting Surfaces	51
4.1.4	Implementation Testing	54
4.2	Fast Multipole Method	59
4.3	Implementation of Fast Multipole Method (FMM)	63
4.3.1	Implementation Steps of FMM	63
4.3.2	Iterative Algorithm	68
4.3.3	Test Cases for FMM	68
4.4	Multilevel Fast Multipole Algorithm (MLFMA)	71
4.4.1	Implementation of MLFMA	72
4.3.2	Test Cases for MLFMA	75
5	TWO-DIMENSIONAL EDGE TREATMENT	80
5.1	Approaches	80
5.1.1	Illumination Windows	81
5.1.2	Resistive Loading of Edges	82
5.2	Preconditioning	84
5.3	Test Cases	84
5.3.1	Surface Setup	84
5.3.2	Gaussian Illumination Plus Resistive Loading	86
5.3.3	2D Resistive Taper Window	88
6	SPILLING BREAKER SCATTERING	94
6.1	Scattering Surface	94
6.2	Calculated Scattering	97
6.3	Analysis of Scattering	99
6.3.1	2-D Synthesis of 3-D Results	99
6.3.2	Two-Scale Treatment	109
7	PLUNGING BREAKER SCATTERING	118
7.1	Scattering Surface	118
7.2	MLFMA Scattering	120
7.2.1	Scattering of the Complete Surface	120
7.2.2	Initial Breaking	121
7.3	EGO/GTD in Breaker Water Wave	123
7.3.1	2-D EGO/GTD in Plunging breaker	124
7.3.2	3-D EGO/GTD in Plunging Breaker	132
8	SUMMARY AND CONCLUSIONS	137
	BIBLIOGRAPHY	142

LIST OF TABLES

7.1 Parameters of reflection points	133
---	-----

LIST OF FIGURES

1.1 Time history plot of the spilling wave	7
1.2 Some individual surface profiles of spilling wave	8
1.3 Time history plot of the plunging wave	9
1.4 Some individual surface profiles of plunging wave	10
2.1 Geometry of 2-D surface	20
2.2 Current approximation using pulse basis functions	23
2.3 Equivalent principle with high loss dielectric scatter	24
2.4 Illustration for MM/GTD technique	26
2.5 Backscattering of spilling water wave using MM/GTD	29
2.6 Backscattering of plunging water wave using MM/GTD	30
3.1 Schematic of PM surface generation	34
3.2 Statistic results of small perturbation model	41
3.3 Reflection from a curved surface	43
3.4 Geometry for diffraction by a curved edge	45
4.1 Triangle pair and geometrical parameters associate with interior edge	48
4.2 Relationship between source triangle T^q and observation point in triangle T^P ...	48
4.3a Segmentation of flat plate	54
4.3b Results of a PEC square with different segmentation numbers	55

4.4a	Segmentation of a disk	55
4.4b	Results of PEC disk with different radius	56
4.5a	Segmentation of a sphere	57
4.5b	Monostatic scattering cross section for PEC spheres as a function of ka	57
4.5c	Monostatic scattering cross section for impedance spheres as a function of ka using 120 patches	58
4.5d	Monostatic scattering cross section for purely imaginary impedance spheres as a function of ka using 120 patches	58
4.6	Relationship between vector \mathbf{r}' , \mathbf{r} , \mathbf{x} and \mathbf{d}	60
4.7a	Relationship between groups and edges	64
4.7b	Groups for 3-D arbitrary surface	64
4.8	Comparison between BICGSTAB and GMRES	69
4.9a	Results with different D for a flat plate	70
4.9b	Results of PEC sphere by using FMM	70
4.10	Tree structure of multi-level grouping	72
4.11	The interpolation and shifting step for moving up tree, and the inverse shifting and filtering step for moving down tree	74
4.12	Testing results of PEC sphere by using MLFMA	76
4.13	Comparison of SPM and MLFMA for “cosine” surface	77
4.14	Comparison of SPM and MLFMA for one deterministic 3-D PM surface	78
4.15	Comparison of Monte-Carlo results of SPM and MLFMA for 3-D PM surfaces.	79
5.1a	LONGTANK profiles	85
5.1b	Profile 9 and 13 with extension in range	85
5.1c	3-D profile with 4λ extension in azimuth from profile 9	86

5.2	Resistive loading in azimuth for 3-D surface	87
5.3	Backscattering of profile 9 (PEC, 10GHz)	89
5.4	Backscattering of profile 9 with impedance (SEA, 10GHz)	90
5.5	Backscattering of profile 13 (PEC, 10GHz)	91
5.6	Backscattering of profile 13 with impedance (SEA, 10GHz)	92
5.7	Two-dimensional resistive loading	93
6.1	Spilling breaker full surface	95
6.2	Backscattering from complete spilling breaker using MLFMA	98
6.3	Comparison of 2-D synthesis and 3-D MLFMA results of the full spilling breaker	100
6.4	Pre-breaking spiller surface	101
6.5	Backscattering from pre-breaking spilling breaker by using MLFMA	102
6.6	Post-breaking spiller surface	103
6.7a	Backscattering from post-breaking spilling breaker by using MLFMA	104
6.7b	Comparison of 2-D backscattering for post-breaking spilling with different extension angles	105
6.8	Comparison of 2-D synthesis and 3-D MLFMA results of the pre-breaking spiller	108
6.9	Comparison of 2-D synthesis and 3-D MLFMA results of the post-breaking spiller	108
6.10	Separation of large-scale and small-scale surface in TSM.....	111
6.11	TSM scattering from complete spilling-breaker using $K_T = k/1.0$	113
6.12	TSM scattering from complete spilling-breaker using $K_T = k/2.0$	114
6.13	TSM scattering from post-breaking spiller using $K_T = k/0.8$	115
6.14	TSM scattering from post-breaking spiller using $K_T = k/1.2$	116

6.15	TSM scattering from post-breaking spiller using $K_T = k/1.6$	117
7.1	Plunging breaker surface	119
7.2	Backscattering from complete plunging breaker by using MLFMA	121
7.3	Single-overturning plunging breaker	122
7.4	Backscattering from initial-breaking surface by using MLFMA	123
7.5	Surfaces used in 2-D EGO/GTD.....	125
7.6	Profile 160 with extensions at both sides	125
7.7	Enlarged profile 160 with reflection points and diffraction point	126
7.8	Comparison of MM/GTD and EGO/GTD of profile 130	127
7.9	Comparison of MM/GTD and EGO/GTD of profile 150	129
7.10	Comparison of MM/GTD and EGO/GTD of profile 160	130
7.11	Comparison of MM/GTD and EGO/GTD of profile 160 with different smooth length.....	131
7.12	Surface used for 3-D EGO	135
7.13	Comparison of 3-D EGO and MLFMA results	136

NOMENCLATURE

BICGSTAB	bi-conjugate gradient-stable
dB	decibels
ε	permittivity
η	intrinsic impedance
\mathbf{E}^i, E^i	incident electric field
\mathbf{E}^s, E^s	scattered electric field
EFIE	electric field integral equation
FMM	fast multipole method
Γ	reflection coefficient
GMRES	generalized minimal residual
GO	geometrical optics
GTD	geometrical theory of diffraction
\mathbf{H}^i, H^i	incident magnetic field
\mathbf{H}^s, H^s	scattered magnetic field
HH	horizontal transmit and receive
HV	horizontal transmit, vertical receive
IE	integral equation

\mathbf{J}, J	electric surface current density
k	wavenumber
KA	Kirchoff approximation
LGA	low grazing angle
λ	illuminating field wavelength
\mathbf{M}, M	magnetic surface current density
MFIE	magnetic field integral equation
MLFMA	multilevel fast multipole algorithm
MM	moment method
μ	permeability
PEC	perfectly electric conducting
PM	Pierson-Moskowitz
PO	physical optics
RCS	radar cross section
RMS	root mean square
RWG	Rao, Wilton and Glisson's basis function
SPM	small perturbation model
SSA	small slope approximation
TSM	two-scale model
VH	vertical transmit, horizontal receive
VV	vertical transmit and receive

CHAPTER 1

INTRODUCTION

Microwave scattering from the ocean surface is of great interest in both military and civilian applications [2,6-12,99,100]. Radar scattering from the surface is usually considered “clutter” which can mask targets of interest on or near the surface. Understanding the surface scattering process will aid in the development of methods to detect target signals from within the clutter. In other applications, the sea scatter itself is used to extract useful information. Sea scatter can be used to measure surface waves, internal waves, current boundaries, temperature gradients, and biological and man-made slicks. The first civilian high-resolution spaceborne synthetic aperture imaging radar, SEASAT, was launched specifically for sea surface remote sensing applications [99]. With the increasing resolution and the development of multi-band and multi-polarization SAR systems, remote sensing radar images are becoming more useful in both military and civilian application [100]. No matter what the application, the mechanisms that lead to backscattering energy when microwave interacts with sea surface must be thoroughly understood.

Sea surface backscattering is reasonably well understood when the radar signal is incident on the surface at moderate incidence angles (30° - 60°). The scattering is dominated by the Bragg resonance effect at moderate angles [2]. However as the

incidence angle approaches grazing (low grazing angle, or LGA illumination), the character of the backscattering changes. In particular, it is characterized by brief bursts of backscatter known as “sea spikes”. Sometimes, this gives rise to “super events”, where HH backscatter exceeds VV [7-9, 74-75]. (HH means that both the transmitted and received polarization is horizontal, while VV indicates vertical polarization in each case.) This behavior is not consistent with the Bragg mechanism, which predicts approximately constant scattering over time with VV significantly exceeding HH [2]. Strong sea spikes can raise the HH backscatter to 10 dB or more above VV [45]. The HH sea spike echoes typically have de-correlation times of several hundred milliseconds, while at VV the order is only of ten milliseconds. Sea spikes can last up to a few hundred milliseconds.

The scattering from the sea surface at low grazing angle has been characterized by the “Doppler splitting” effect in studies [86,87]. The Doppler spectra of both vertical and horizontal backscattering are almost the same at small and moderate incidence angles. When the incidence angle tends to grazing, the spectral peak of VV appears at a lower Doppler frequency than that of HH. The “slow peak” of HH gradually disappears from the HH spectrum while the “fast peak” dominates. Conversely, the fast peak diminishes and slow peak dominates in VV. The higher Doppler-shifted energy has sometimes been called “fast” scattering associated with “fast” surface scatterers while the lower shifted energy has been referred to as “slow” scattering.

1.1 Breaking Wave Scattering

Breaking waves have been suggested as a strong contributor to the backscattering from the sea surface at low-grazing-angle (LGA) (high incidence) illumination [43-45, 78, 79, 82, 83], and particularly are thought to be responsible for strong sea spikes. Specular

reflection from very steep features on the crest of breaking waves has also been suggested as the cause of fast-scatterer signals faster than that expected from Bragg scattering [85]. For this reason, most theoretical and numerical studies of the scattering from breakers have focused primarily on the steep features and the multipath interference that may give rise to the sea-spike phenomena [78,79,82].

There are several models to explain sea spikes. The most popular theory is multipath scattering that scatters off the crest and then reflects from the front surface of wave. Wetzel [78] proposed steep features on the crest of breaking wave as the dominant scatterers. Some energy scatters directly back to the radar from the front face, while some scatters toward the front face of the wave and reflects toward the radar. Interference between the direct and multipath scattering leads to the $HH > VV$ signatures typical of sea spikes. Trizna [79] refined this model to include the effects of the finite conductivity of the surface, which tends to dampen the VV multipath through Brewster angle effects.

Plant [86] introduced a “bound-Bragg” model to explain the fast scattering signals. In this theory, it assumed that small waves that are Bragg-resonant with the incident electromagnetic energy are bound to the front face of steep, large-amplitude waves. The local incidence angle for these Bragg scatterers is greatly reduced due to the tilt of the front face. The HH scattering cross-section predicted by Bragg theory increases dramatically as the local incidence angle decreases. Thus, the scattering from the bound waves would dominate that from untilted roughness. As the bound waves do not freely propagate but move with the much higher velocity large waves, this gives the fast-scatter signal. VV Bragg scatter is much less sensitive to the local tilt, so the bound-wave signatures do not dominate and the fast scatter signal does not appear.

Numerical studies of rough surface scattering have typically been performed statistically. Numerous samples of rough surfaces are generated numerically from the same roughness spectrum and the scattering from the individual surfaces are combined to estimate the scattering statistics. This is known as Monte-Carlo analysis. The disadvantage of this technique is that it is difficult to distinguish the contributions of individual scatterers. This work will therefore rely upon deterministic treatment of breaking wave profiles.

1.1.1 Definition of 2-D and 3-D Surfaces

In this paper, two kinds of surfaces are considered. One is a surface that is uniform in one dimension. The surface height can be expressed as $z = f(x)$. As it is a function of only x , this is sometimes referred to as a one-dimensionally (1-D) rough surface. However, this surface type yields a two-dimensional (2-D) radar-cross section, and requires a 2-D electromagnetic analysis. Thus, it is sometimes termed a 2-D surface. To avoid confusion, this paper refers to this type of surface as a two-dimensional scattering problem throughout. This is particularly important since overturning surfaces are considered, where the term “one-dimensionally rough” loses its meaning. The second type of surface is not uniform in one dimension. It can be described by $z = f(x, y)$ in the absence of overturning. This surface type leads to three-dimensional (3-D) scattering cross-sections and requires a 3-D electromagnetic analysis. For consistency, this is termed a “3-D surface” and “3-D problem”, although it may sometimes be termed as a “2-D rough” surface in the literature in the absence of overturning.

1.1.2 Previous Work

Numerical investigation of breaking waves has been performed by Ja [43], Ja et al. [44] and West and Ja [17]. A 2-D electromagnetic technique, moment method/geometrical theory of diffraction (MM/GTD), was applied to 2-D surfaces representing the time evolution of breaking waves measured in the University of Maryland wave tank [88]. Ja et al. used a time-dependent Fourier analysis technique to relate calculated scattering signatures to specific features on the wave surface [44]. As the wave steepens and a bulge forms on the forward face of the crest prior to breaking, horizontal-to-vertical polarization backscattering (HH/VV) ratios up to 0 dB appeared with gently spilling breakers. With more energetic plunging breakers, HH/VV as high as 20 dB was observed when jetting features appeared on the crest [45]. The time-dependent Fourier analysis also revealed differences in the Doppler signatures at the two polarizations. The HH spectra showed strong signals at the higher frequencies associated with the phase velocity of the wave, but much weaker signals at lower Doppler shifts. At VV the signals at higher and lower shifts were approximately equal. The highest shifts observed were associated with the jetting features, while lower shifts were correlated with the turbulent “scar” that remains on the surface after breaking.

West and Ja [17] applied the two-scale scattering model to the wave tank breakers at low grazing angles. They found that two-scale-model (TSM) was unable to consistently predict the scattering from the very steep and/or multivalued features that form on the wave crest immediately before breaking. After the initial breaking, the accuracy of TSM depended upon the nature of the roughness in the turbulent scar left behind on the crest. TSM gave a fairly good prediction of the backscattering while the scar roughness

appeared primarily on the front face of the wave, but accuracy was quickly lost as the wave overtook the scar and the roughness moved to the top of the crest and the back face of the wave.

As mentioned, the previous numerical work was limited to scattering from 2-D waves. This significantly limits the analysis of the scattering. In the work that follows a full 3-D scattering code will be applied to 3-D profiles that were synthesized from the measured 2-D wave tank profiles. The measured wave profiles are therefore reviewed here.

1.1.3 Spilling Breaker Water Wave

Fig. 1.1 shows the measured time history plot of the spilling wave that was considered by Ja and West [44]. The wave was mechanically generated by a vertical oscillating wedge at the end of a 14.8 m long, 1.22 m wide and 1.0 m deep wave tank [88]. A video camera was mounted on a carriage that moved along the tank at the same speed as the wave crest. The camera viewed the wave crest from the side, looking down at 5° from horizontal. Two light-emitting diodes were attached to the carriage which illuminated a florescent dye on the surface that was imaged. The camera operated at a sampling ratio of 472 frames/second.

The consecutive profiles were stacked vertically to form Fig. 1.1. The vertical axis therefore gives increasing time. Since the camera was moving at the long wave phase velocity, a surface feature shifting toward left or right with increasing time indicates that it moves faster or slower than the camera, respectively. 329 frames were measured for this wave, corresponding to a time duration of 697 ms. The measured surface profiles are 117 mm long in range direction (left to right in the figure). Initially, the surface is

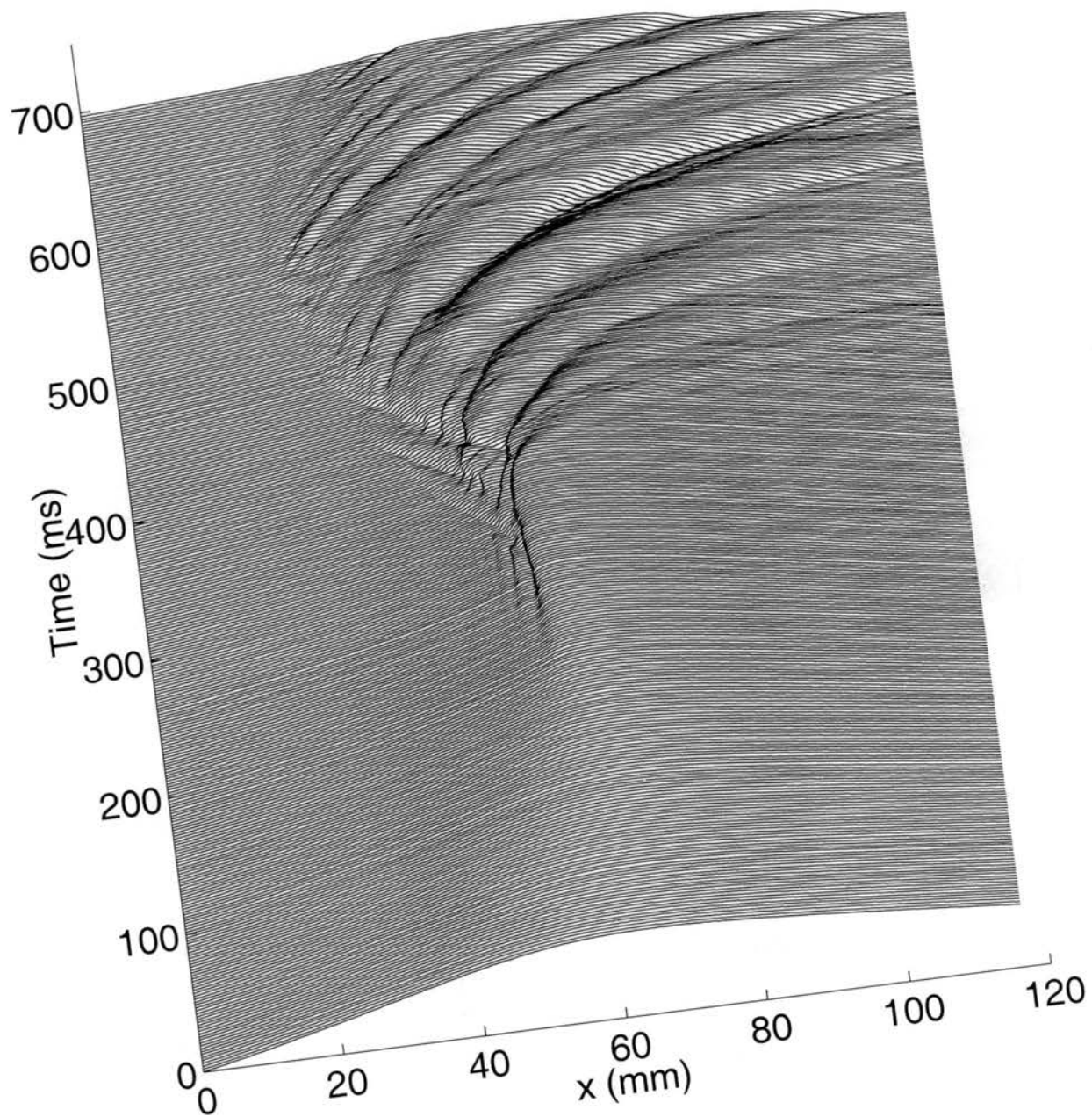


Fig. 1.1: Time history plot of the spilling wave.

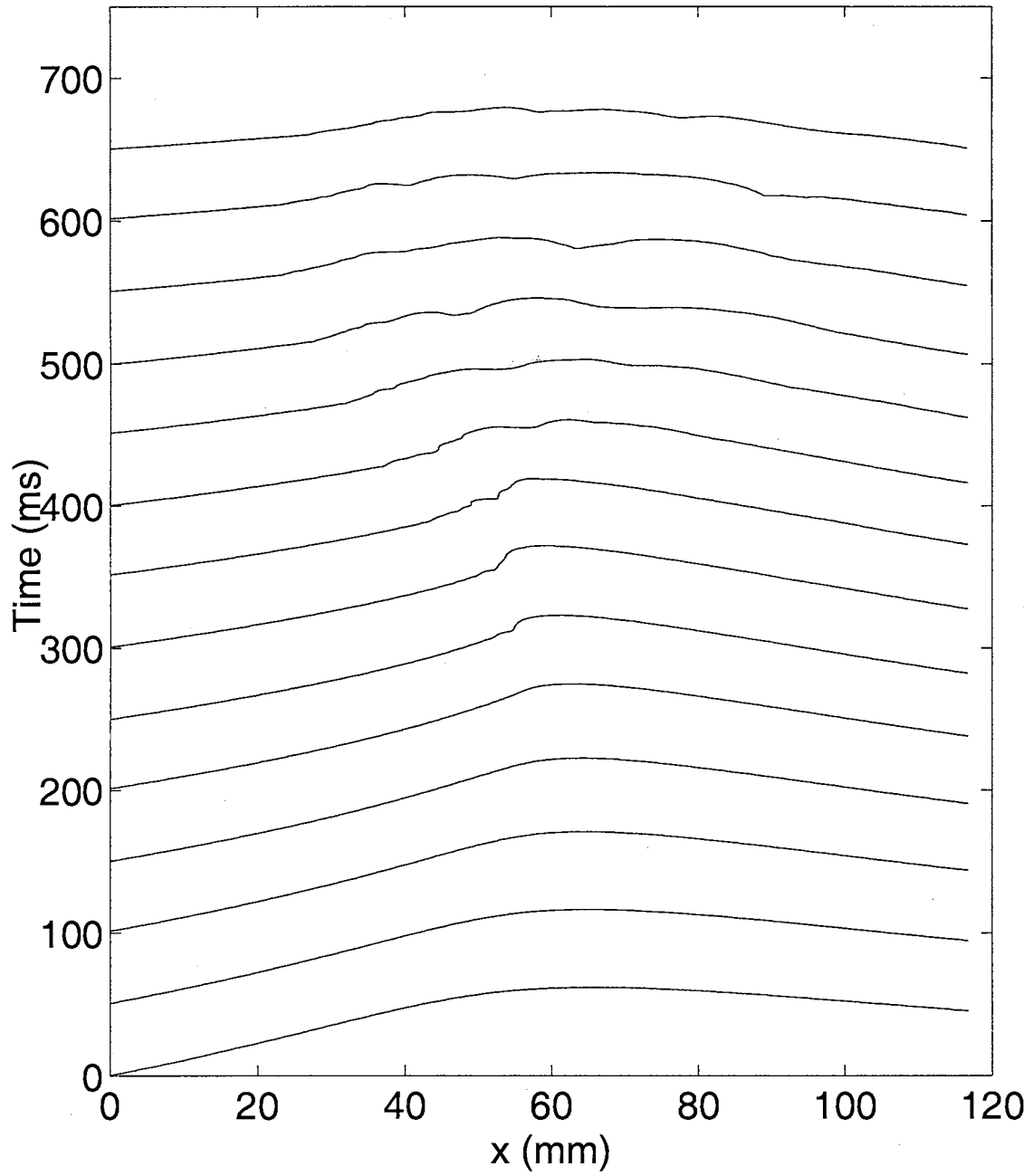


Fig. 1.2: Some individual surface profiles of spilling wave.

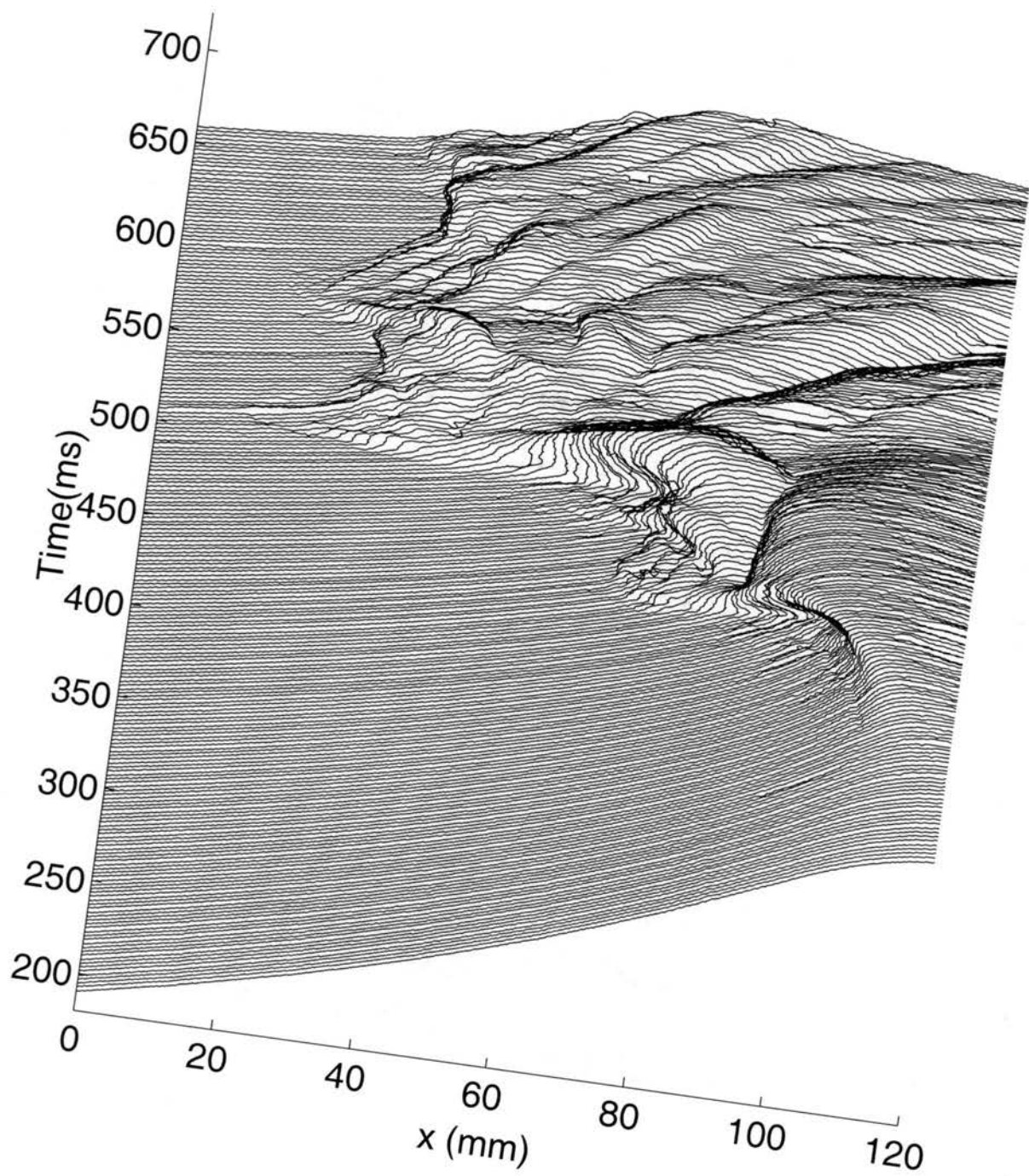


Fig. 1.3: Time history plot of the plunging wave.

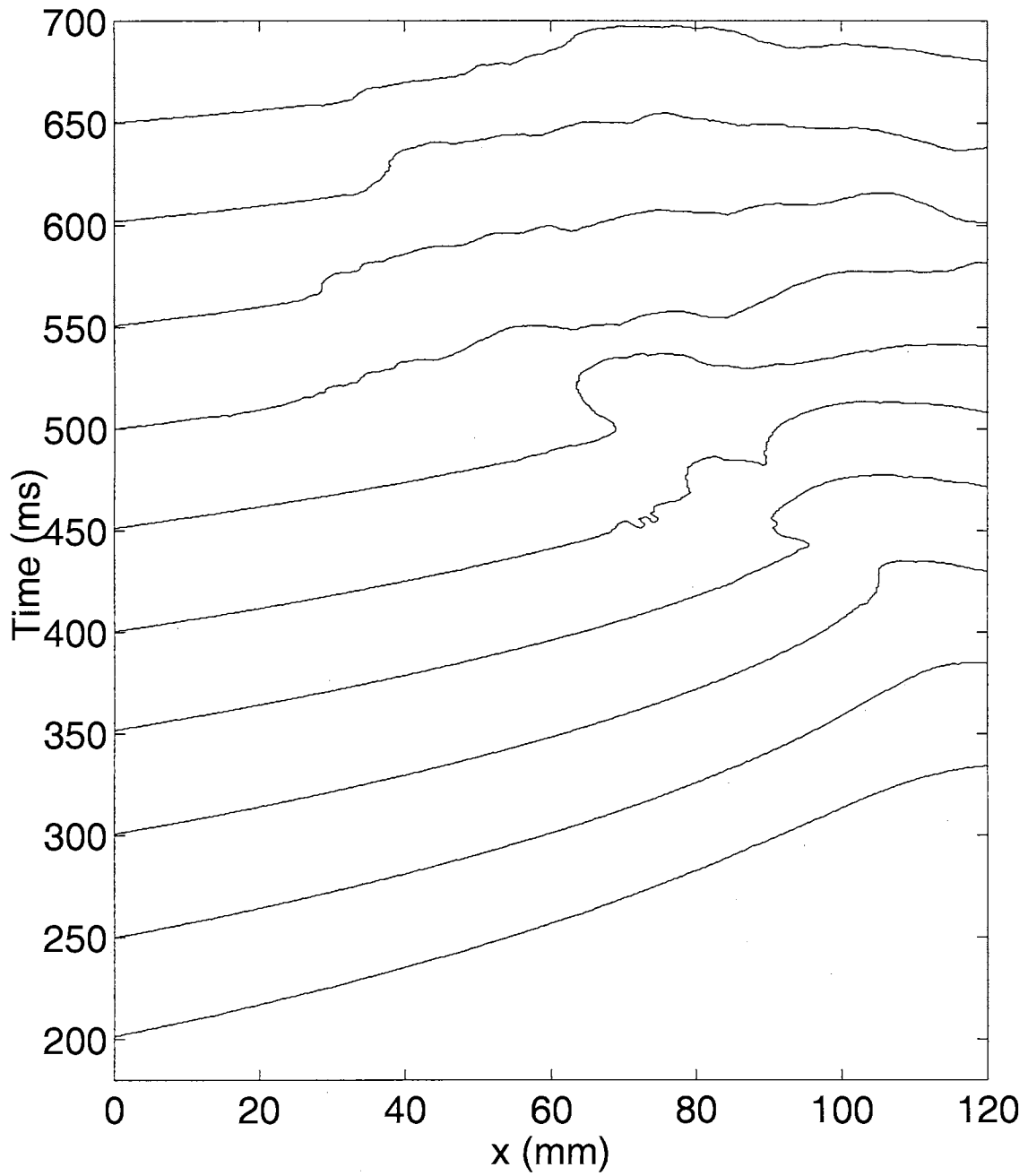


Fig. 1.4: Some individual surface profiles of plunging wave.

relatively smooth, with the crest then steepening. The height reaches a maximum of 35 mm at 190 ms (profile 90). A plume starts to appear around 210 ms (profile 99). Parasitic capillary waves of about 5 mm in length form just below the “toe” of the plume from 210 ms to 310 ms. This waves breaks at 370 ms (profile 175). After breaking, the plume collapses and turbulent regions are generated on the front face of the wave. The turbulence is carried by the orbital motion of the long wave, so is passed by the crest. New turbulent regions then form continuously. Fig. 1.2 shows individual sample surface profiles from the complete spilling breaker history.

1.1.4 Plunging Breaker Water Wave

Fig. 1.3 shows a plunging breaker wave that was generated under similar conditions to previous the spilling wave. However, a high concentration of a soluble surfactant, Triton X-100, was added to the water. Surfactants reduce the surface tension of the water, changing the behavior of the breaking. In particular, the breaking is more energetic than in the previous spilling case, giving intervals where jets form. This wave has 222 frames (profile 90 to profile 311), corresponding to a time history from 190 ms to 659 ms. This surface has two overturning points, occurring at 370 ms and 460 ms. This breaker was used in [45]. Super-events were identified during the two overturning points, giving HH-to-VV ratios of 20 dB and 10 dB, respectively. Fig. 1.4 shows sample individual surface profiles of this plunging breaker.

1.2 Existing Scattering Models

Wave scattering from rough surfaces was first examined theoretically by Rayleigh in 1907, and has been intensely studied since the development of radar and sonar in the

middle of the 20th century. Initially the approaches were limited to analytical models that include various approximations to allow closed-form approximate solutions to Maxwell's equations. Unfortunately, the approximations introduce limitations in the conditions under which the models are valid. The ranges of validity are not always obvious from the development. As computer technology has developed, the analytical studies have been supplemented by numerical scattering studies. Numerical scattering approaches, when properly implemented, yield the "exact" solution to which the models can be compared and tested. However, they tend to be computationally very expensive. Their primary use is therefore to test the models under controlled conditions to identify their ranges of validity, so that the models may be used to construct computationally efficient algorithms that are valid under all ranges of conditions.

1.2.1 Analytical Models

The two "classical" rough surface scattering models are the Kirchhoff approximation (KA) [2] and the small-perturbation method (SPM) [10, 14]. KA uses the physical optics (PO) current on planes tangent to the scattering surface to approximate the true induced current. This current is then re-radiated to give the scattered field. KA has several approximations that limit its application. First, KA assumes that the radius of curvature of the surface is large compared with the radar wavelength. This is required for the tangent plane approximation to be valid. It also uses the optical shadowing approximation, so ignores diffraction and multipath scattering into shadow regions at small grazing angles. It therefore is valid only for gently undulating surfaces, although the surface displacement can be large compared to the electromagnetic wavelength. Thorsos [35] and Chen et al. [39] have numerically examined KA, and showed it is accurate only for for-

ward scattering near the specular direction. It performs poorly for backscattering.

Perturbation theory was first introduced by Rayleigh [6], and was formulated as the small-perturbation method (SPM) by Rice in 1951 [10]. It has been thoroughly studied by others since the 1960s [2,11-15]. SPM assumes that the surface roughness is small compared to the electromagnetic wavelength. SPM predicts “Bragg resonant” scattering, which results from a resonance between the electromagnetic energy and short surface waves roughness at about the same wavelength [2].

The two-scale-model (TSM) is a combination of the KA and SPM models that retains the advantages of both. Introduced by Wright [12], TSM separates the surface roughness into two different components. Ideally the small-scale component is sufficiently small in displacement that SPM applies. The other component of the roughness is considered large-scale, meaning that the KA model will apply. TSM therefore requires that the actual surface be separated into the large- and small- scale components. It is not always possible to define a criterion where both the small-scale and large-scale surface requirements are met. The results may therefore depend upon the separation scheme used. TSM also suffers from the same limitations as KA when surface self-shadowing occurs. Wright [12] showed that TSM can describe most sea surface backscattering at small and moderate incidence angles.

Recently two models have been introduced that are variations on standard perturbation theory: the small slope approximation (SSA) [6] and the phase perturbation technique (PPT) [32, 33]. These methods have the advantage of not requiring a scale separation of the surface roughness, which is regarded as the main drawback of TSM. SSA was introduced by Voronovich [6]. It represents an expansion of the scattered field

in terms of the roughness slope rather than height. SSA is therefore appropriate for scattering from large-scale (the Kirchhoff regime), intermediate-scale and small-scale (the Bragg regime) roughness. The slopes of sea surface roughness are generally small except at the crest of steep breaking waves. Berman [26] has numerically demonstrated the effectiveness of SSA for both deterministic and statistical 2-D rough random surfaces. Broschat and Thorsos applied SSA to 2-D rough surfaces that approximate the sea surface without steep breaking waves using a “Pierson-Moskowitz” (PM) sea surface spectrum [27-28]. They found that SSA works well over a broad range of scattering angles for small to moderate slopes. Ewe et al [30] compared SSA with numerical calculations for 3-D Gaussian correlated surfaces. They found that the computationally simple 1st order SSA is correct only for low incidence angles. 2nd order SSA appeared accurate up to 70° incidence angles at the expense of much greater computational load. Voronovich and Zavorotny [22] compared statistical SSA (both 1st order and 2nd order) results with experimental scattering from rough sea surfaces at Ku- and C-bands. Good agreement was obtained at moderated angles for 2nd order SSA. Soriano et al [25] compared SSA and KA with reference moment method results. SSA proved the superior to KA for surfaces with Gaussian spectra and single valued, moderate slope for all the incidence angles at both statistical and deterministic cases. For more complicated surfaces, higher order was suggested. To date, no SSA results for scattering from 3-D breaking wave surfaces have been reported.

The phase perturbation technique (PPT) was first suggested by Winebrener and Ishimaru [32, 33]. It is based on a perturbation expansion of the phase of the field. This technique was derived by only using Dirichlet boundary condition, so it is only suitable

for horizontal polarization (HH) backscattering from perfectly conducting surfaces. Broschat [34] applied it to scattering from 3-D rough statistical surfaces following the Pierson-Moskowitz wave height spectrum [37].

Another recently introduced model is EGO/GTD [91-96]. Geometrical optics (GO) and the geometrical theory of diffraction (GTD) are high frequency methods. They can only be applied to structures whose features are large compared to wavelength. Voltmer [94] demonstrated that with a modification of GO it can be applied to reflection from surfaces with radii of curvature as small as $1/3\lambda$. This was termed extended GO (EGO) by West [91]. West [91] also showed that EGO corrections could be applied to GTD diffraction coefficients, and applied EGO/GTD to a numerically generated 2-D time history of a plunging breaker. EGO is useful in modeling the scattering from steep and jetting surfaces.

1.2.2 Numerical Methods

The analytical models mentioned above can provide a good approximation for wave scattering only under certain conditions. Numerical methods provide the opportunity to test the ranges of validity of the models, and to allow the treatment of multivalued overturning surfaces.

The moment method (MM) is typically used to find the reference scattering in rough surface scattering studies. Introductions to MM for electromagnetic problems are given by Harrington [3] and Bancroft [4]. MM is used to discretize continuous integral equations into forms easily solvable by computer. Two integral equations commonly used in electromagnetic scattering problems are the electric field integral equation (EFIE) and the magnetic field integral equation (MFIE). MM discretizes these equations to produce a

linear matrix equation that can be easily solved to give the surface current. Once the unknown surface current density is found, the scattered field can be calculated by evaluating radiation integrals. MM was first used with perfectly conducting surfaces. It has been further applied to imperfectly conducting surfaces by Senior and Volakis [84] using the concept of impedance boundaries. West et al. [41], Johnson et al [15] and Holliday et al. [8] have implemented impedance boundary moment methods for sea surface scattering.

The main limitation of the moment method is that the computational complexity grows dramatically as the size of the scattering surface increases. The order of the solution time increases by N^2 when iterative solution is used, and N^3 when direct solution is used, where N is the number of unknowns in the discretization. This is clearly the limiting factor when three-dimensional problems are considered, where doubling the dimensions of the surface gives a four-fold increase in the number of unknowns. The basic moment method must be refined to allow application to general, large rough surfaces.

Rokhlin developed a method to rapidly solve integral equations (IE) that arise in classical potential theory known as the fast multipole method (FMM). This was then adapted to treat acoustical wave scattering problems [53], and 2-D electromagnetic scattering problems. It was extended to the full 3-D EM scattering problem by Rokhlin [55]. FMM can be seen as an extension of the moment method that uses a multipole expansion of the MM interaction matrix to accelerate the matrix-vector multiplications that are needed in an iterative solution. The computational cost of FMM is of order $O(N^{1.5})$. A multi-level extension of FMM was applied by Lu and Chew [58] to 3-D

electromagnetic problems. Termed the multi-level fast multipole algorithm (MLFMA), it reduces the computational complexity of iterative solution to $O(N \log N)$. MLFMA has been applied to numerous EM problems [59-67].

Other algorithms that have been developed to accelerate the standard moment method are the banded matrix iterative approach/canonical grid (BMIA/CGA) introduced by Tsang et al [68,69] and the novel spectral acceleration technique introduced by Chou and Johnson [90]. These approaches are limited to single valued surfaces, so are less general than FMM/MLFMA.

1.3 Edge Treatment in Numerical Methods

When numerically modeling the electromagnetic scattering from surface, the surface must be artificially truncated due to finite computer resources. The truncated edges introduce non-physical diffraction that can mask the scattering from the actual surface features if the edge is not properly treated. Several approaches have been used to treat the edges in moment method based method, including illumination windowing [35], a hybrid technique combining the moment method with geometrical theory of diffraction (MM/GTD) [43-45], and resistive loading of the edges [74-77]. The Thorsos illumination window has proven quite popular [35]. However, as the incidence angle tends to grazing, the surface must be very large to give realistic illumination. This approach becomes quite expensive at LGA, particularly for arbitrary 3-D surfaces. MM/GTD on the other hand can be applied at arbitrarily small grazing angles, but is limited to 2-D surfaces.

Compared with other methods, resistive loading of the edges has the advantage of very low computational overhead, while not requiring the surface to be modified at low grazing angle. It appears to be a promising approach for treating scattering from arbitrary

3-D rough surfaces. West [76] showed that a resistive taper introduced by Haupt and Liepa [74] was effective in reducing the edge effects in scattering from 2-D surfaces that approximate breaking water waves.

1.4 Overview

The purpose of this work is to study the scattering from rough surfaces representing the crests of breaking water waves at low grazing angle illumination. A full 3-D MLFMA with impedance boundary conditions and resistive edge treatment has been implemented to provide the reference scattering calculations. The test 3-D breaking crests are synthesized from the existing 2-D wave measurements. The predictions of the existing scattering models are compared with the reference scattering under various conditions, identifying the ranges of validity under the specific test conditions.

Chapter 2 gives a review of the numerical MM/GTD technique used in previous 2-D breaking wave studies. This technique will be used to calculate reference 2-D scattering, which will be compared with 3-D results. Different analytical scattering models, including KA, SPM, TSM, and EGO/GTD are reviewed in Chapter 3. Details of the implementation of the MLFMA numerical code are presented in Chapter 4. In chapter 5, the treatment of edges using resistive loading in general 3-D surface scattering will be considered. In Chapters 6 and 7, the scattering from 3-D surfaces modeling breaking wave crests will be examined. The effectiveness of the analytical models is evaluated, as is the potential use of 2-D results to synthesize the 3-D scattering. Chapter 6 focuses on the gently spilling breaker while Chapter 7 considers the more energetic plunging crest.

CHAPTER 2

REVIEW OF NUMERICAL TECHNIQUE FOR 2-D SURFACES

The numerical scattering code used by Ja et al [43,44] and West and Ja [17] for scattering from two-dimensional surfaces will be used as a reference to which the three-dimensional surface techniques will eventually be compared. A brief review of this approach, known as the hybrid moment-method/geometrical-theory-of-diffraction technique (MM/GTD) is given here. A complete description of the code is given in West et al [41] and Sturm and West [42].

2.1 Moment Method for Perfectly Conducting Surfaces [1,3]

The core of the MM/GTD 2-D scattering code is based on the moment method. The moment method was developed in the 1960's as a technique to solve linear integral equations (IE) through a discretization process. When used for electromagnetic scattering, the moment method is first used to solve an integral equation derived from the field boundary conditions, giving the surface current. The surface current is then re-radiated into space to give the scattered field.

The geometry for scattering from a 2-D surface when the incident illumination is horizontally polarized is shown in Fig. 2.1a. Since the magnetic field is everywhere orthogonal to the z dimension, this is often referred to as transverse magnetic (TM)

polarization. When the surface is a perfectly electric conducting (PEC), a true surface current density will be induced on the surface that has only a z component, designated by J_z . The boundary condition $(\hat{n} \times (\mathbf{E}^i + \mathbf{E}^s)) = 0$ can be used in the TM case to give

$$E_z^i(\boldsymbol{\rho}) = -E_z^s(\boldsymbol{\rho}) = \frac{k\eta}{4} \int_c J_z(l') H_0^{(2)}(k|\boldsymbol{\rho} - \boldsymbol{\rho}'|) dl' = L_E[J_z(l)], \quad (2.1)$$

where $\boldsymbol{\rho}'$ is the vector from the origin to a source point on the surface, $\boldsymbol{\rho}$ is the vector from the origin to an observation point on the surface, k is the electromagnetic wave number, η is the intrinsic impedance of medium above the surface ($\eta = \eta_0 = 120\pi \Omega$ for free space), l is the distance along the arc-length of the surface, and $H_0^{(2)}(\cdot)$ is the Hankel function of the second kind of order zero. (2.1) is known as an electric field integral equation (EFIE) since the electric field boundary conditions are met.

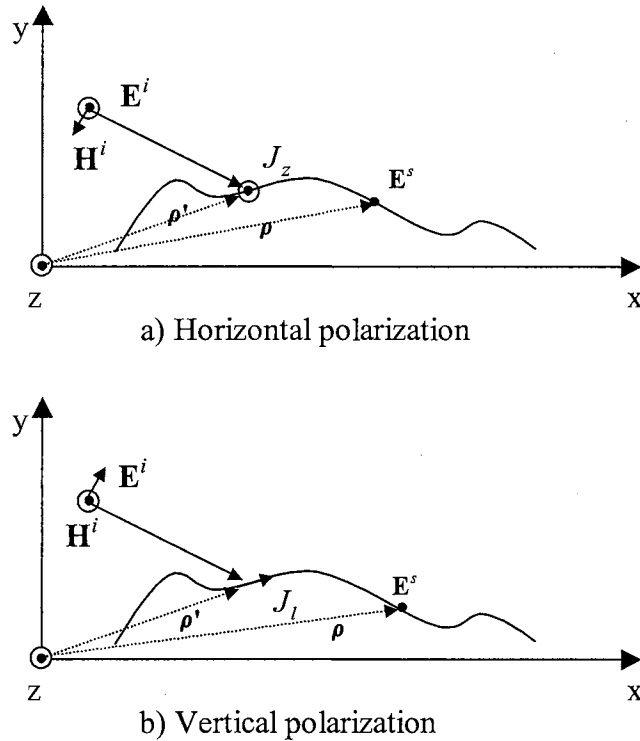


Fig. 2.1: Geometry of 2-D surface.

Fig. 2.1b shows the geometry for the vertically (or transverse electric (TE)) polarized case. In this case, the surface current on a PEC surface is along the arclength of the surface, designated by $J_l(l)$. In this case, the magnetic field boundary condition $\hat{n} \times (\mathbf{H}^i + \mathbf{H}^s) = \mathbf{J}$ can be used to derive the magnetic field integral equation (MFIE), given by

$$H_z^i = -H_z^s = - \left\{ \frac{J_l(l')}{2} + j \frac{k}{4} \int_c J_l(l') \left(\hat{n}' \cdot \frac{\boldsymbol{\rho} - \boldsymbol{\rho}'}{|\boldsymbol{\rho} - \boldsymbol{\rho}'|} \right) H_1^{(2)}(k|\boldsymbol{\rho} - \boldsymbol{\rho}'|) dl' \right\} = L_M[J_l(l)], \quad (2.2)$$

where \hat{n}' is the unit vector normal to the surface at the source point, and $H_1^{(2)}()$ is the Hankel function of the second kind of order 1.

Both the TM EFIE and the TE MFIE can be written in the generic form.

$$F_z^i = L_X[J_s(l)], \quad (2.3)$$

where F is either the electric field E or magnetic field H , X is either E or M , and s is either z or l . To discretize this equation, the surface current is first approximated by a finite series

$$\hat{J}_s = \sum_{n=1}^N I_n f_n, \quad (2.4)$$

where the f_n 's are basis (or expansion) functions and the I_n 's are unknown coefficients to be found. This expansion is substituted into (2.3) to give the residual

$$R(l) = F_z^i(l) - L_X \left[\hat{J}_s \right] = F_z^i - \sum_{n=1}^N I_n L_X[f_n(l)]. \quad (2.5)$$

The last step makes use of the fact that the field integral equations use linear operators. Since (2.4) uses a finite basis expansion, the residual in (2.5) is non-zero. The moment

method minimizes the residual by defining N weighted residuals as

$$R_m(l) = \langle w_m(l), R(l) \rangle = \langle w_m(l), F_z^i(l) \rangle - \sum_{n=1}^N I_n \langle w_m(l), L_X[f_n(l)] \rangle, \quad (2.6)$$

where $w_m(l)$ is a weighting function and $\langle w_m(l), g(l) \rangle$ is the inner product defined by

$$\langle w_m(l), g(l) \rangle = \int w_m(l) g(l) dl, \quad (2.7)$$

Setting the weighted residual equal to zero gives

$$\sum_{n=1}^N I_n \langle w_m(l), L_X[f_n(l)] \rangle = \langle w_m(l), F_z^i(l) \rangle. \quad (2.8)$$

(2.8) represents a linear algebraic system of N equations and N unknowns (I_n 's), which can be written as

$$[Z_{mn}][I_n] = [V_m]. \quad (2.9)$$

$[Z_{mn}]$ is often termed as the MM interaction matrix. The unknown $[I_n]$ vector can be found using standard linear algebra techniques, completing the moment-method solution.

The usual approach for scattering from 2-D surfaces is to use sub-domain pulse basis functions. The sub-domain approach involves subdivision of the surface current into N non-overlapping segments. The basis function (f_n) in each subdivision is

$$f_n(l) = \begin{cases} 1 & l_{n-1} \leq l \leq l_n \\ 0 & \text{elsewhere} \end{cases}. \quad (2.10)$$

Dirac delta functions are typically used as weighting functions applied at the center of each basis function. This choice forces the residuals to be exactly zero at discrete points, so is often referred to as ‘‘point matching’’.

Pulse basis functions yield piecewise constant approximations of the current, as shown in Fig. 2.2. The far field scattering is found by integrating the current, so the

piecewise constant approximation does not give significant error, and accuracy improves with decreasing segment lengths. Segment lengths of 0.05λ have been shown to give sufficiently accurate results even at the small scattering cross-sections [43].

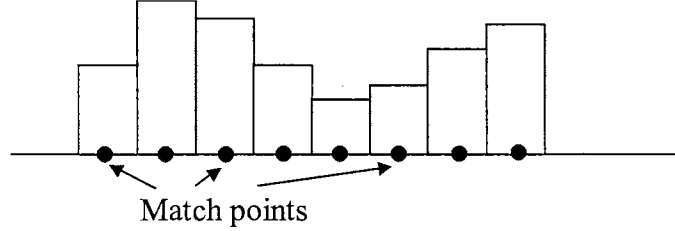


Fig. 2.2: Current approximation using pulse basis functions.

The far field scattering is found by using,

$$E^s = -\frac{k\eta}{4} \int_c J_z(l') H_0^{(2)}(k|\boldsymbol{\rho} - \boldsymbol{\rho}'|) dl', \quad \text{for HH polarization.} \quad (2.11a)$$

$$H^s = j\frac{k}{4} \int_c J_l(l') \left(\hat{n}' \cdot \frac{\boldsymbol{\rho} - \boldsymbol{\rho}'}{|\boldsymbol{\rho} - \boldsymbol{\rho}'|} \right) H_1^{(2)}(k|\boldsymbol{\rho} - \boldsymbol{\rho}'|) dl', \quad \text{for VV polarization.} \quad (2.11b)$$

The 2-D radar cross-section of scattering from 2-D surface is defined as [1]

$$\sigma_{2-D} = \lim_{\rho \rightarrow \infty} \left[2\pi\rho \left| \frac{F^s}{F^i} \right|^2 \right] \quad (2.12)$$

2.2 Moment Method for Imperfectly Conducting Surfaces [1]

When the scattering surface is perfectly conducting, a true surface current is induced on the surface which the moment method finds directly. With finite conductivity media such as seawater, however, the field penetrates the surface and a volume current is induced. Treating volume currents directly with the moment method is very expensive. Instead, an equivalent problem may be solved since the scattering medium is homogeneous. Fig. 2.3 shows the application of the equivalence principle to an arbitrary scatterer [3]. Both the

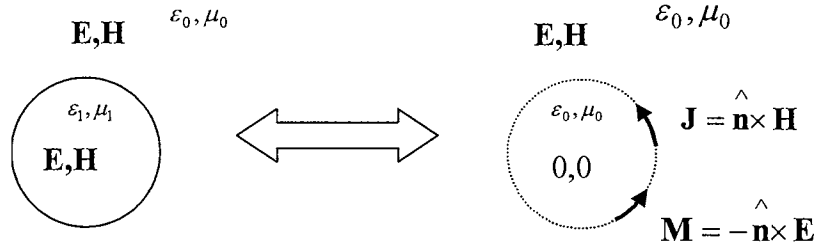


Fig.2.3: Equivalent principle with high loss dielectric scatter.

electric equivalent surface current density \mathbf{J} and a magnetic surface current density \mathbf{M} must be found by the moment method. This may be accomplished by expanding both the electric surface current \mathbf{J} and magnetic surface current density \mathbf{M} in finite series of the form in (2.5) [42]. This doubles the number of unknowns to be found compared to the perfectly conducting case. However, if the conditions

$$\left| \sqrt{\varepsilon_r} \right| \gg 1, \quad \left| \text{Im}(\sqrt{\varepsilon_r}) k \rho_l \right| \gg 1 \quad (2.13)$$

are met, where ε_r is the complex dielectric constant and ρ_l is the radius of curvature of the interface, the problem may be simplified. In this case, the field transmitted into the scattering medium will be refracted to nearly normal to the interface, and the magnetic current can be accurately represented by the impedance boundary condition [49,84]

$$\mathbf{M} = -Z_s \hat{\mathbf{n}} \times \mathbf{J}, \quad (2.14)$$

where Z_s is the intrinsic impedance of the scatterer. For seawater at 10 GHz, $\varepsilon_r \approx 56.26 - j37.47$, so the conditions of (2.13) are satisfied for all test conditions to be considered. Impedance boundary conditions are therefore used throughout.

For horizontal polarization (TM), the magnetic current will be induced along the surface arclength, so is designated M_l . The scattered field will include contributions from both J_z and M_l .

$$E^s = E^s(J_z) + E^s(M_l). \quad (2.15)$$

$E^s(J_z)$ is given by (2.11a). $E^s(M_l)$ is obtained by applying duality [3] to (2.2), yielding

$$\begin{aligned} E^s(M_l) &= \frac{M_l(l')}{2} + j\frac{k}{4} \int_c M_l(l') \left(\hat{n}' \cdot \frac{\rho - \rho'}{|\rho - \rho'|} \right) H_1^{(2)}(k|\rho - \rho'|) dl' \\ &= L_M[M(l)] \end{aligned} \quad (2.16)$$

Using the impedance boundary condition of (2.14) in (2.16) gives

$$E^s(M_l) = -Z_s L_M[J_z(l')]. \quad (2.17)$$

Applying the field boundary condition and using (2.15), gives the impedance boundary EFIE:

$$E^i = -\left(E^s(J_z) + E^s(M_l)\right) = L_E[J_z(l')] + Z_s L_M[J_z(l')]. \quad (2.18)$$

The impedance boundary MFIE for vertically polarized scattering is found by applying duality to (2.18), yielding

$$H^i = L_M[J_z(l')] + \frac{Z_s}{\eta_0^2} L_E[J_z(l')]. \quad (2.19)$$

Equations (2.18) and (2.19) require only J_z be discretized, so applying the moment method to the large, but finite conductivity case is only slightly more expensive than the PEC case. In particular, the size of the linear system that must be solved, the most expensive step, is unchanged. The MM solution follows the same steps followed in Section 2.1.

2.3 Hybrid MM/GTD Technique [40-42]

The impedance boundary integral equations in (2.18) and (2.19) apply only to closed surfaces or infinitely extending open surfaces. Due to finite computer resources, the infinite surface must be truncated in the moment method treatment. If the surface was simply truncated with no further treatment, this would introduce artificial edges that would affect the scattering. One technique for edge diffraction suppression is the hybrid MM/GTD that was developed by Burnside et al [40] and numerically implemented for rough surface scattering by West et al [41] and Sturm and West [42]. The MM/GTD approach avoids the edge effects by infinitely extending the truncated surface as shown in Fig. 2.4.

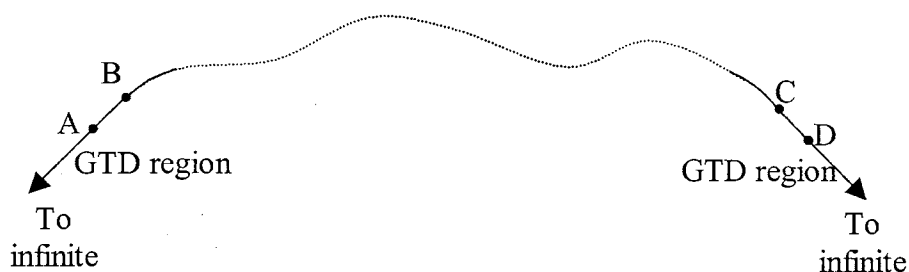


Fig. 2.4: Illustration for MM/GTD technique.

The dotted line shows the actual (truncated) rough surface, while the solid line is the extension. The surface is rounded off at each side and extended planarly to infinity. With the infinite extensions the impedance boundary integral equations may be used. However, attempting to apply the moment method directly to the full infinite surface would have the same limitations as the original surface. Instead, the geometrical theory of diffraction (GTD) is used to limit the number of unknowns that must be determined. The extensions outside of point B on the left and point C on the right are ideally planar. Moreover, the angles of the planar sections to horizontal are chosen so that all points on the extension

are shadowed from all points on the rough surface. The field at the face of the planar section is therefore fully described by the incident field (if the section is not shadowed), plus a field diffracted from the connection point B or C. Sufficiently far from the diffraction point (beyond points A or D) the diffracted field is ray optical, so may be described by GTD. The MM/GTD approach therefore uses a single basis function derived from the GTD field to describe the unknown current everywhere on the infinite extensions beyond points A and D. Traditional pulse basis functions are used between A and D. Thus, a finite number of basis functions are used to represent the current on the infinite surface, so the system may be treated with finite computer resources.

The electric current in the GTD region can be written as

$$\mathbf{J}_{\text{GTD}} = \begin{cases} \mathbf{J}_{\text{d}} + \mathbf{J}_{\text{KA}} & \text{GTD region} \\ 0 & \text{otherwise} \end{cases}, \quad (2.20a)$$

$$\mathbf{J}_{\text{d}} = \begin{cases} \hat{a}_z J_0 \frac{e^{-jk\rho}}{\rho^{1.5}} & \text{HH} \\ \hat{a}_l J_0 \frac{e^{-jk\rho}}{\sqrt{\rho}} & \text{VV} \end{cases}, \quad (2.20b)$$

$$\mathbf{J}_{\text{KA}} = (1 - \Gamma) \hat{n} \times \mathbf{H}^i, \quad (2.20c)$$

where \mathbf{J}_{d} is the current induced by the diffracted field, \mathbf{J}_{KA} is the known Kirchoff approximation current due to the directly incident field \mathbf{H}^i , J_0 is an unknown coefficient to be found using the moment method, and Γ is the reflection coefficient at the interface. The surface current between A and D is expanded using standard MM technique. Therefore A to D can be regarded as the standard MM region. The current on the entire surface can be expressed as

$$\mathbf{J} = \begin{cases} \hat{a} \sum_{n=1}^N I_n f_n, & \text{for HH } \hat{a} = \hat{a}_z, \text{ for VV } \hat{a} = \hat{a}_l & \text{MM region} \\ \mathbf{J}_{\text{GTD}} = \mathbf{J}_d + \mathbf{J}_{\text{KA}} & & \text{GTD region} \end{cases} \quad (2.21)$$

The moment method is used to find the unknown I_n and J_0 coefficients. The additional cost of the MM/GTD approach over the standard moment method is modest.

2.4 2-D Scattering

Fig. 2.5 and Fig. 2.6 show the scattering from the time histories of the spilling and plunging breaker waves shown in Fig. 1.1 and Fig. 1.3, respectively, found using MM/GTD. The incidence angle was set at 80° , and the frequency was 10 GHz. This is duplicated from Ja [43] and Ja et al [44]. The GTD planar extensions were angled 30° from horizontal. Pulse basis functions of width 0.03λ were used. The figures were generated by applying MM/GTD to the individual profiles in Figs. 1.1 and 1.3 and plotting with the profile number as the abscissa. VV backscattering is plotted as a solid line and HH is shown as a dashed line.

2.4.1 Spilling Breaker

Fig. 2.5 shows the scattering from the spilling breaker. Initially the profiles are quite round, up to profile 50. The scattering is therefore very small. The crest steepens and a plume forms from profile 50 to profile 175. The scattering increases at both polarizations in this time. The wave breaks after profile 175. At this point, the plume collapses and the surface becomes more random. This is reflected by oscillating scattering with increasing profile number. After breaking, the scattering is primarily due to the Bragg mechanism. The peaks of the VV scattering therefore remain approximately constant after breaking,

HH however decreases as the roughness moves across the crest to the backside of the wave, increasing the local incidence angle. No super event is evident in the spilling breaker backscattering.

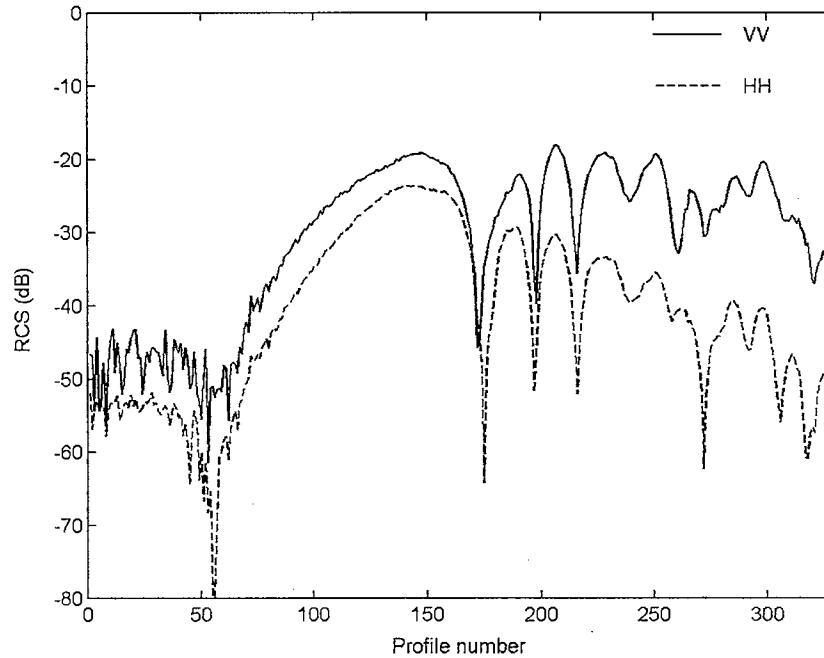


Fig. 2.5: Backscattering of spilling breaker water wave using MM/GTD.

2.4.2 Plunging Breaker

Fig. 2.6 shows the scattering from the plunging breaker. The plunging breaker is more energetic than spilling breaker, with two large overturnings. One is around profile 190, the other is around profile 206. The crest of the surface is overall steeper, giving larger backscattering at both polarizations. Initially the wave crest is round and the cross-sections are small. The cross-section increases as the crest steepens. HH exceeds VV beginning around profile 140, giving a super event through profile 172. HH exceeds VV by as much as 20 dB in this time. The second overturning is centered at profile 206. This gives a lower magnitude super event. VV exceeds HH with all profiles after 220. The

surface is more random after breaking than the spilling breaker, giving more rapid oscillation.

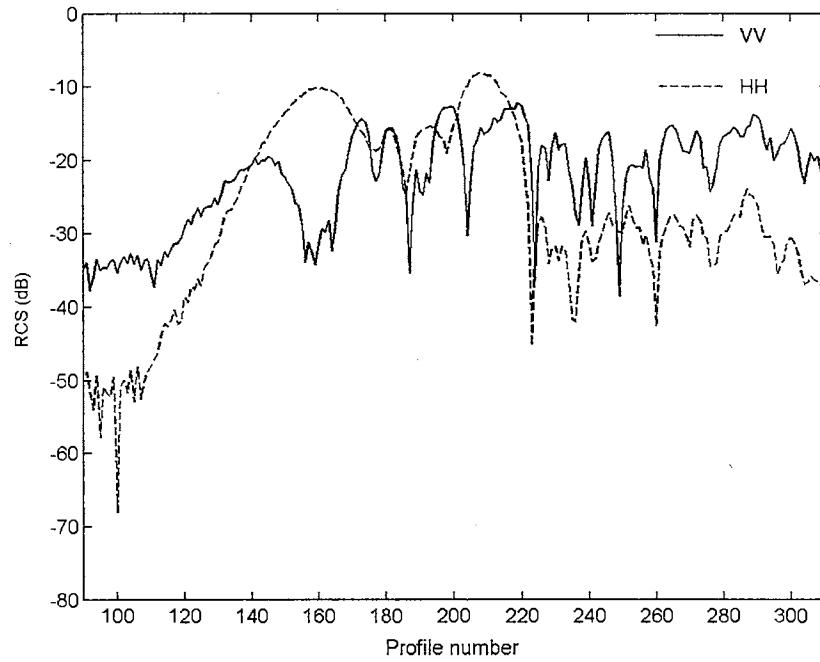


Fig. 2.6: Backscattering of plunging breaker water wave using MM/GTD.

CHAPTER 3

REVIEW OF SCATTERING MODELS

Radar scattering from rough surfaces is typically modeled using analytically based techniques that use different approximations in their development. Analytical models provide direct physical insight into the scattering mechanisms, and can be applied very rapidly. This gives a large advantage in real time applications. However, the approximations used in developing the models limit the ranges of accuracy. These limitations must be fully understood for the models to be used effectively. Numerical methods provide a tool to check these analytical models.

The most commonly used models to describe sea-surface scattering are the two-scale-model (TSM), the small slope approximation (SSA) and the phase perturbation technique (PPT). TSM is a combination of the Kirchhoff approximation (KA) and the small-perturbation model (SPM). These models will be briefly reviewed in this chapter. Although the scattering models will be ultimately applied to the deterministic breaking wave profiles of Fig. 1.1 and Fig. 1.3, they are typically used to find the scattering from statistically rough surfaces that can be described by linear wave spectra. Sample cases will therefore first be tested using the approximate Pierson-Moskowitz wave spectrum and presented in this chapter. Issues related to application to deterministic surfaces will be considered in later chapters.

Extended geometrical optics/geometrical theory of diffraction (EGO/GTD) is another useful and simple mode in analyzing the scattering mechanisms. It was recently introduced for use in overturning cases [91].

3.1 Random Surface Generation--Pierson-Moskowitz (PM) Spectrum

The Pierson-Moskowitz surface model was developed as a method to describe the sea surface roughness statistically. It assumes that the roughness is an ideal, linear, stationary, two-dimensional random process, so can be described by a simple linear power spectral density (typically termed the “Pierson-Moskowitz spectrum”). Being linear, it ignores wave-wave interactions, and can not predict overturning or breaking waves. It also does not include the effects of surface tension on the smallest scale features. However, it does include a dependence on wind speed, allowing the generation of surfaces with both small and large RMS roughness that approximates the roughness of the actual sea. Moreover, the temporal changes of the surface can be predicted using wave dispersion relations. It therefore has proven to be useful in generating test cases where analytical scattering may be tested under controlled conditions. Note that the one-dimensional Pierson-Moskowitz yields a two-dimensional profile under the nomenclature adopted in this paper while the two-dimensional spectrum yields a three-dimensional profile.

3.1.1 Pierson-Moskowitz Spectrum [37,15]

The one-dimensional Pierson-Moskowitz wave number spectrum is given by

$$W_1(K) = \frac{\alpha}{4|K|^3} \exp\left[\frac{-\beta g^2}{K^2 U^4}\right], \quad (3.1)$$

where α and β are dimensionless constants given by 8.1×10^{-3} and 0.74, respectively, g is the gravitational acceleration constant ($g = 9.81 \text{ m/s}^2$), U is the wind speed measured at 19.5m above the mean sea surface and K is the surface-wave spatial wave number (which is different than the radar wave number k). This wave number spectrum is found by applying the deep-water wave dispersion relation to the original P-M frequency spectrum [37]. The variance of surface height h of the surface is therefore

$$\langle h^2 \rangle = \int_{-\infty}^{+\infty} W_1(K) dK = \frac{\alpha U^4}{4\beta g^2}, \quad (3.2)$$

and the peak in the spectrum occurs at

$$K_{peak} = \sqrt{2\beta/3g} U^2. \quad (3.3)$$

Equation (3.1) gives a one-dimensional spectrum that assumes all wave energy on the surface is propagating in the same direction. This is not realistic for a real sea. The directional dependence can be added by forming a two-dimensional spectrum:

$$W_2(\mathbf{K}, \phi) = \Phi(K, \phi) W_1(K) / K, \quad (3.4)$$

where $\mathbf{K} = \hat{a}_x K_x + \hat{a}_y K_y = \hat{a}_x K \cos \phi + \hat{a}_y K \sin \phi$, $K = |\mathbf{K}|$, and $\Phi(K, \phi)$ describes the azimuthal dependence. It is normalized such that

$$\int_0^{2\pi} \Phi(K, \phi) d\phi = 1, \quad (3.5)$$

so the one-dimensional spectrum is recovered from $W_1(K) = \int_0^{2\pi} W_2(\mathbf{K}, \phi) K d\phi$.

Assuming a uniform azimuthal dependence, the isotropic 2-D Pierson-Moskowitz distribution is

$$W_2(K) = \frac{\alpha}{8\pi|K|^4} \exp\left[\frac{-\beta g^2}{K^2 U^4}\right]. \quad (3.6)$$

3.1.2 Generation of Sample Surfaces

The analytical models are applied to sample surfaces generated from the PM spectrum. The surface generation is accomplished using the procedure shown in Fig. 3.1. First, the data array that will contain the surface height is filled with Gaussian white noise that has a variance of 1.0. The noise is then passed through a filter whose transfer function is given by (3.6). The filtering is usually performed using FFT's as shown in the figure.

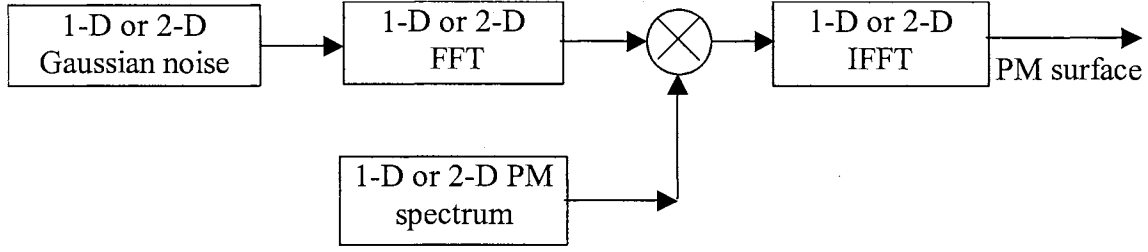


Fig. 3.1: Schematic of PM surface generation.

The RMS height of the resulting surface can be set by using a proper wind speed. For the 2-D case, the sampling interval in the Fourier-transformed wave number domain is

$\frac{2\pi}{N_x \Delta_x}$ in x direction, and is $\frac{2\pi}{N_y \Delta_y}$ in the y direction, where Δ_x , Δ_y are sampling

intervals in the spatial domain and N_x , N_y are the number of samples. The discrete

wavenumbers range over $-\frac{\pi}{\Delta_x} < K_x \leq \frac{\pi}{\Delta_x}$ and $-\frac{\pi}{\Delta_y} < K_y \leq \frac{\pi}{\Delta_y}$.

3.2 Two Scale Model

The two-scale scattering model (TSM) is the combination of two simple scattering models. It consists of a small-scale perturbation of the Kirchhoff-approximation scattered

field, so is a combination of the SPM and KA models. It was introduced in the 1960s and has been widely used to describe ocean surface scattering at small and moderate incidence angles. It has been extensively applied to scattering from statistical surfaces, and recently was applied to 2-D rough deterministic breaking waves by West and Ja [17].

3.2.1 Kirchhoff's Approximation

The Kirchhoff approximation (KA) uses the tangent plane approximation to estimate the currents on the scattering surface, which are then reradiated to give the scattered field.

The equivalent electric current and magnetic surface currents are approximated as

$$\mathbf{J}_{\text{KA}} = \begin{cases} (1 - \Gamma) \hat{n} \times \mathbf{H}^i; & \text{illuminated area,} \\ 0; & \text{shadowed area} \end{cases} \quad (3.7a)$$

$$\mathbf{M}_{\text{KA}} = \begin{cases} -(1 + \Gamma) \hat{n} \times \mathbf{E}^i; & \text{illuminated area,} \\ 0; & \text{shadowed area} \end{cases} \quad (3.7b)$$

in which Γ is the surface reflection coefficient. For a perfectly conducting surface, $\Gamma = -1$. Once the KA current is found, the far-field scattering can be calculated numerically via the radiation equations.

KA has serious inherent limitations. First, it assumes that the radius of curvature of surface is everywhere large relative to the radar wavelength. Only then may the currents be found from (3.7a) and (3.7b), which assumes the incident field illuminates on an infinite flat plate. Second, surface self-shadowing can only be modeled by setting the currents in the shadowed areas to exactly zero. This is not ideal due to diffraction and multipath scattering of the incident energy into the shadow area. Therefore KA is only a coarse approximation. Thorsos [35] has investigated the validity of KA for random one-dimensional rough surfaces with Gaussian roughness spectra. KA proved to have good

performance around specular scattering angles, but has very poor performance at large incident (small grazing) angles even with shadowing corrections. For backscattering, KA is only valid when the incident angle is very small and the surface is relatively smooth.

3.2.2 Small Perturbation Model

The small perturbation model (SPM) was introduced by Rice [10] for scattering from slightly rough planar surfaces. SPM is suitable for surfaces that have electromagnetically small height displacement. The fields can be expanded in a perturbation series in the surface wave number domain. SPM directly gives the field scattered, and then an ensemble average is performed to give the backscattering coefficient. More details are described in section 12.5 of [2] and [14]. The ensemble averaged scattering coefficient is

$$\sigma_{pp'} = 4\pi k^4 \Gamma_{pp'}^2 W(-2k \sin \theta \cos \phi, -2k \sin \theta \sin \phi), \quad (3.8a)$$

where θ is the incident angle and ϕ is the azimuth look angle with respect to x-axis. p and p' represent the polarizations of incident and scattered fields respectively. They can be either H polarization or V polarization. $\Gamma_{pp'}^2$ is a polarization dependent coefficient given by

$$\Gamma_{pp'}^2 = \begin{cases} 0, & p = H, p' = V \text{ or } p = V, p' = H \\ \cos^4 \theta, & \alpha = H, \beta = H \\ \left(1 + \sin^2 \theta\right)^2, & \alpha = V, \beta = V \end{cases} \quad (3.8b)$$

Note that after ensemble averaging first-order SPM predicts that the backscatter depends only on the surface roughness energy at $\mathbf{K} = 2k \sin \theta \left(\hat{a}_x \cos \phi + \hat{a}_y \sin \phi \right)$. This roughness energy resonates with the incident field giving the backscatter. This is known

as Bragg-resonant scattering. The perturbational analysis used in developing SPM fails when the surface roughness height is significant compared to the electromagnetic wavelength.

3.2.3 Two Scale Model (TSM)

TSM was formulated to bridge the gap between SPM and KA. First the surface is separated into large-scale and small-scale roughness components. KA is first applied to the large-scale roughness, while SPM is used to perturb the KA fields using the small-scale roughness. Usually TSM is implemented statistically. The approach is to incoherently add the scattering due to the large-scale roughness using the Kirchhoff approximation to the scattering from first order SPM applied to the small-scale roughness. The local angle of incidence in the SPM application is adjusted to account for the tilt of the surface by the large-scale roughness [12]. However, Brown gave an explicit expression for the deterministic TSM field for perfectly conducting rough surfaces prior to ensemble averaging that can be directly compared with a numerically calculated field [14].

The deterministic TSM field can be regarded as the coherent summation of the large-scale and the small-scale fields. The two-scale model is applied by first dividing the surface roughness into large-scale and small-scale components, given by $\zeta_l(x, y)$ and $\zeta_s(x, y)$ respectively. The full roughness is recovered by simple addition: $\zeta(x, y) = \zeta_s(x, y) + \zeta_l(x, y)$. The large-scale scattered field is given by

$$\delta^0 E_{pp'} = -j \frac{E_0 k_0 \delta_{pp'}}{2\pi r} \exp(-jk_0 r) \iint \exp(-2j\vec{k}_i \cdot \vec{r}_0) dx dy, \quad (3.9a)$$

while the first order SPM field is

$$\delta^1 E_{pp'} = \frac{E_0 k_0^2}{\pi r'} \exp(-jk_0 r) \iint \left[2 \left(\hat{n}_l \cdot \hat{e}_p \right) \left(\hat{n}_l \cdot \hat{e}_{p'} \right) + \left(\hat{n}_l \cdot \hat{k}_i \right)^2 \left(\hat{e}_p \cdot \hat{e}_{p'} \right) \right] \exp(-2j\vec{k}_i \cdot \vec{r}_0) \zeta_s (1 + \zeta_{lx}^2 + \zeta_{ly}^2)^{1/2} dx dy, \quad (3.9b)$$

where \hat{n}_l is the unit vector normal to the unperturbed large-scale surface, and

$\vec{r}_0 = \hat{a}_x x + \hat{a}_y y + \hat{a}_z \zeta_l$. \vec{k}_i is the incident wave vector given by

$$\vec{k}_i = \frac{2\pi}{\lambda} \left[\hat{a}_x (-\sin\theta \cos\phi) + \hat{a}_y (-\sin\theta \sin\phi) + \hat{a}_z (-\cos\theta) \right], \quad (3.10)$$

\hat{e}_p and $\hat{e}_{p'}$ are polarization vectors that may be either

$$\hat{e}_H = -\hat{a}_x \sin\phi + \hat{a}_y \cos\phi \quad (3.11a)$$

for horizontal polarization or

$$\hat{e}_V = -\hat{a}_x \cos\theta \cos\phi - \hat{a}_y \cos\theta \sin\phi + \hat{a}_z \sin\theta \quad (3.11b)$$

for vertical polarization. \hat{e}_p and $\hat{e}_{p'}$ will be different for cross-polarized scattering.

$\delta_{pp'} = 1$ ($p = p'$) or 0 ($p \neq p'$),

(3.9) gives the expression for a PEC surface. For imperfectly conducting surfaces, the field can be expressed as

$$E_{\text{impedance}} = E_{\text{PEC}} a_{pp'}. \quad (3.12a)$$

$a_{pp'}$ is a polarization dependent coefficient given by [2, 97]

$$a_{VV} = -(\varepsilon_r - 1) \frac{\sin^2 \theta_i - \varepsilon_r (1 + \sin^2 \theta_i)}{\left[\varepsilon_r \cos \theta_i + \sqrt{\varepsilon_r - \sin^2 \theta_i} \right]^2} \frac{\cos^2 \theta_i}{1 + \sin^2 \theta_i}, \quad (3.12b)$$

$$a_{HH} = -\frac{\cos \theta_i - \sqrt{\varepsilon_r - \sin^2 \theta_i}}{\cos \theta_i + \sqrt{\varepsilon_r - \sin^2 \theta_i}}, \quad (3.12c)$$

where θ_i is the local incident angle with respect to the external normal vector of the large

surface, defined by $\cos \theta_i = -\hat{n}_l \bullet \hat{k}_i$.

SPM has the same shadowing limitations as KA. Usually shadowing is incorporated by assuming the scattering from surface sections that are shadowed is zero. Some studies have investigated shadowing from two-scale statistical surfaces [18-21]. These results cannot be directly applied to deterministic scattering due the averaging that may mask shadow region scattering.

As noted, TSM requires that the surface roughness be divided into small-scale and large-scale components. This is typically accomplished by defining a wave number threshold K_T in the roughness spectrum. All energy below the threshold is considered large-scale and all energy above is considered small-scale. The threshold must be carefully chosen so that both the small- and large-scale components meet the limitations of SPM and KA respectively. Often it is not possible to ideally satisfy both conditions, and the scattering predicted will depend on the exact threshold K_T used. This is a primary limitation of TSM.

Performing the separation can also prove difficult. Simply using a numerical “brick-wall” filter at the threshold K_T would lead to Gibb’s phenomenon ringing. Instead, the approach used by West and Ja [43,44] is used. In this, N passes of the three point moving

average are applied to filter out the small-scale energy and yield the large-scale surface. This weighted moving average (MA) filter can be described as

$$h^{m+1}(n) = 0.25h^m(n-1) + 0.5h^m(n) + 0.25h^m(n+1), \quad (3.13)$$

where $h^m(n)$ is the height at the n th sample point after m filter passes. This requires the surface be sampled evenly in the horizontal dimension. The small-scale roughness is obtained by subtracting the large-scale surface from the original surface. The effective threshold wave number for this procedure is [43,44]

$$K_T = \int_0^\pi \left(\frac{1 + \cos K}{2} \right)^N dK / \Delta. \quad (3.14)$$

where Δ is the horizontal sampling step size. The filter is applied along one dimension first, and then along the other with 3-D surfaces.

3.2.4 Application

Use of SPM is now demonstrated through the application to statistically rough surfaces generated from the Pierson-Moskowitz wave height spectrum. The RMS height of surface was set to 0.005λ . The sample surfaces were therefore electromagnetically slightly rough, so the SPM results may be directly compared to analytically averaged cross-sections in (3.8a). There is no large-scale effect. 200 sample surfaces 128 by 128 points generated numerically using the procedure in Section 3.1.2. The sampling was 0.1λ in both directions. The field scattered from each surface was then found using equations (3.9) through (3.12). Finally, the fields from all 200 surfaces were averaged and normalized by illuminated area A_{ill} . This gives a scattering coefficient defined by [14].

$$\sigma_{pp'} = \lim_{r \rightarrow \infty} \frac{4\pi r^2 \overline{|E_{pp'}|^2}}{A_{ill} E_0^2}. \quad (3.15)$$

This is known as a Monte-Carlo study. The comparison of the Monte-Carlo simulations with the analytically averaged cross-sections is shown in Fig. 3.2. Excellent agreement is obtained above 15° incidence. Below 15° there is small scattering that cannot be predicted by first-order SPM. This could be better represented using second-order SPM [6] and the Kirchhoff approximation [2]. However, we are concerned only with large incidence scattering, so this was not considered.

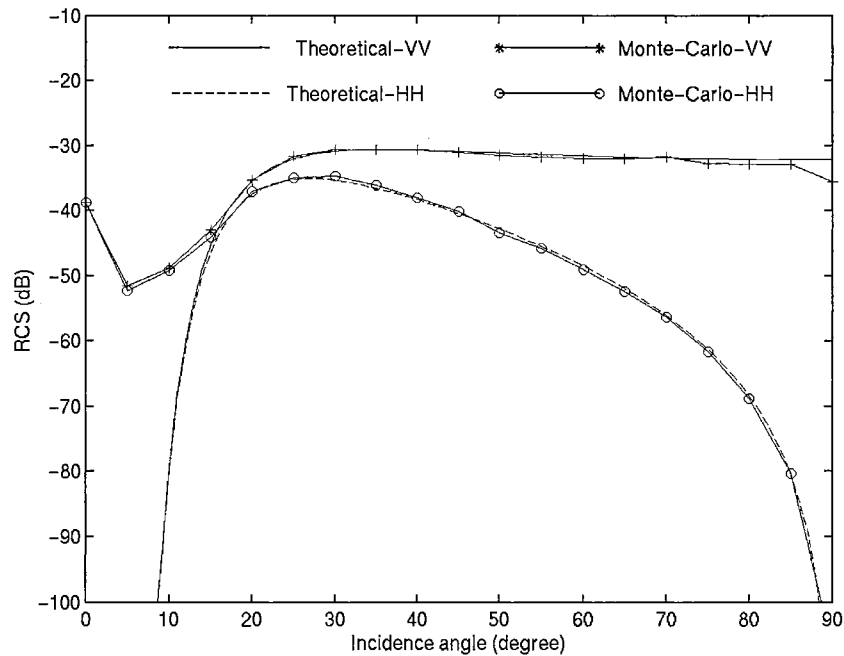


Fig. 3.2: Statistic results of small perturbation model.

3.3 Small Slope Approximation (SSA)

The small-slope approximation (SSA) was introduced by Voronovich [6] to avoid the artificial scale-separation required by TSM. As suggested by the name, the field

equations are expanded in surface slope rather than height and therefore a scale separation is not needed. SSA may therefore be applied directly to multiscale surfaces. SSA can be shown to reduce to SPM or KA in the proper small- or large-scale roughness limits. Broschat and Thorsos [28] investigated SSA when applied to surfaces whose roughness spectra were described by Gaussian envelopes, and correlated the accuracy to the RMS surface slope and incidence angle. Full details of the development of SSA are given in [6]. Recently SSA was applied to the 2-D profiles and performed more poorly than TSM at large incidence, even considering the TSM thresholding problem [98]. Therefore it was not considered further for the 3-D rough case.

3.4 Extended Geometrical Optics/Geometrical Theory of Diffraction

Geometrical Optics (GO) and the geometrical theory of diffraction (GTD) are approximate high-frequency methods. GO is based on ray tracing. It is an optical model that only gives specular reflection, and it can only be used to find the reflection from the structures with large radii of curvature. However a modification, GO can be applied to reflection from surfaces with radii of curvature as small as $\lambda/3$ [94]. This approach was termed as extended GO (EGO) in [91]. GTD can be used to predict the diffractive scattering of discontinuities in surface derivatives [1]. Standard GTD also expects the surface curvature to be large compared to the wavelength. West [91] showed that the EGO correction term can also be applied to GTD diffraction terms to extend its usefulness to smaller surface radii. It was used to find the scattering from steep and jetting surfaces. The details of EGO/GTD are reviewed now.

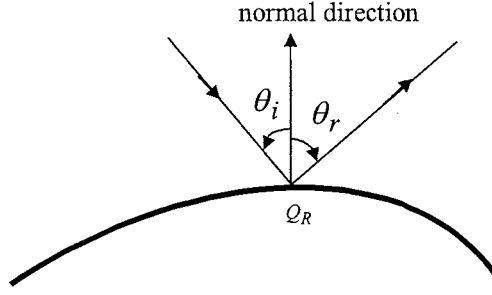


Fig. 3.3: Reflection from a curved surface.

The geometry of a reflection from a curved surface is illustrated in Fig. 3.3. Q_R is reflection point, and θ_i and θ_r are the local incident and reflection angle with respect to the normal direction, respectively. $\theta_i = \theta_r$. The reflected field $\mathbf{E}^r(r)$ at a distance r from Q_R can be expressed as [1]

$$\mathbf{E}^r(r) = \mathbf{E}^i(Q_R) \cdot \Gamma \sqrt{\frac{\rho_1^r \rho_2^r}{(\rho_1^r + r)(\rho_2^r + r)}} e^{-jkr}, \quad (3.16)$$

where $\mathbf{E}^i(Q_R)$ is the field at the reflection point, Γ is the reflection coefficient at the reflection point, and ρ_1^r and ρ_2^r are the principal radii of curvature of the reflected wave front at the point of reflection. The principal radii of curvature are related to the curvature of the reflecting surface at Q_R and the principal radii of curvature of the incident wave front. For plane wave incidence, the principal radii of curvature of the incident wave front are infinite. Therefore, ρ_n^r can therefore be written as

$$\rho_n^r = \frac{\rho_{a_n} \cos \theta_i}{2}, \quad n=1,2, \quad (3.17)$$

where ρ_{a_n} is the radius of curvature of the reflecting surface at Q_R . For specular backscatter, $\theta_r = \theta_i = 0$. ρ_{a_n} is defined to be positive for convex curvature and negative for concave curvature at the reflecting point.

Classical GO is valid when the curvature of the surface is large compared with the incident wavelength. An extended GO (EGO) was given by Voltmer [94]. In EGO, the scattered field of (3.16) is multiplied by a correction term M . For back-reflection [95],

$$M = \begin{cases} 1 + j \frac{11}{16(k\rho_a)} - \frac{353}{512(k\rho_a)^2}, & VV \\ 1 - j \frac{5}{16(k\rho_a)} + \frac{127}{512(k\rho_a)^2}, & HH \end{cases} \quad (3.18)$$

Voltmer [94] and Stutzman and Theile [95] showed that EGO yields accurate cross sections for reflection from circular cylinders with radii as small as $1/3\lambda$.

As GO is limited to specular reflection, it does not predict diffractive scattering from surface discontinuities. The geometrical theory of diffraction (GTD) was introduced by Keller [92] to add the diffracted field component. Since then, numerous diffraction coefficients have been introduced to treat edges [91], creeping waves [93], curvature discontinuities [96], and other diffraction mechanisms [96]. Here we are concerned with diffraction from surface curvature discontinuities. An illustration of the diffraction point is shown in Fig. 3.4. Q_D is the diffraction point and R_1 and R_2 are the surface radii to either side of Q_D . The diffracted field can be represent by

$$\mathbf{E}^d(r) = \mathbf{E}^i(Q_D) \cdot \Gamma \cdot \bar{D} \cdot A e^{-jkr}, \quad (3.19)$$

where $\mathbf{E}^i(Q_D)$ is the incident field at the diffraction point, \bar{D} is the diffraction coefficient and A is a spatial attenuation factor. For plane wave incidence and a 2-D

profile, $A = \frac{1}{\sqrt{r}}$. The uniform theory of diffraction (UTD) diffraction coefficient can be obtained from equations (4.55) through (4.59) of McNamara [96]. The diffraction coefficients were derived from the uniform GTD for curved-face edges introduced by Kouyoumjian and Pathak [93]. At the diffraction point, discontinuous curvature was treated as a wedge with 180° internal angle, giving a wedge-angle parameter of $n = 1$. EGO is applied to individual diffraction fields associated with reflection from the two faces. Full details were described in West [91].

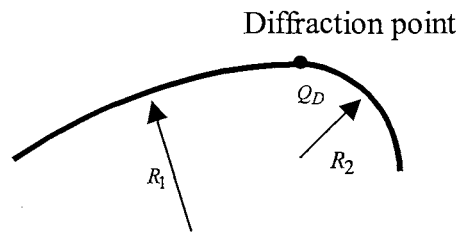


Fig. 3.4: Geometry for diffraction by a curved edge.

The complete EGO/GTD scattered field is obtained from the coherent summation of the reflected and diffracted fields.

CHAPTER 4

NUMERICAL CODE FOR 3-D SURFACE SCATTERING

The numerical scattering code described in Chapter 2 was limited to the 2-D problem. In this chapter the development of a numerical technique for scattering from arbitrary 3-D surfaces will be described. The foundation of the technique is the Rao-Wilton-Glisson (RWG) basis function that was developed by Rao et al. for scattering from arbitrary 3-D closed scatterers [47,48]. The theory of the RWG-based moment method is reviewed for both perfectly conducting and impedance boundary surfaces. The solution of the RWG moment method is accelerated using the multi-level fast multipole algorithm (MLFMA), which allows a very large number of unknowns to be considered [52-67]. MLFMA is also reviewed, and the performances of two different iterative solution methods are compared. Some test cases are given to demonstrate the implementation of MLFMA. The initial scalar MLFMA code was written by James C. West. This was extended to the full vector code using RWG basis functions and impedance boundary conditions by the author.

4.1 Review of RWG Basis

RWG basis functions are specialized sub-domain basic functions that were developed to describe the current on pairs of adjacent triangular patches. Because arbitrarily shaped 3-

D surfaces can be accurately modeled using triangular patches, RWG basis functions are well suited to scattering from arbitrary surfaces. Note that because the current is not limited to flowing in a specific direction, the RWG basis function is a vector basis function.

4.1.1 Perfectly Conducting Surfaces

When an incident electric field \mathbf{E}^i impinges on a perfectly conducting (PEC) surface, the scattered electric field \mathbf{E}^s can be expressed as

$$\mathbf{E}^s = -j\omega\mathbf{A} - \nabla\Phi, \quad (4.1)$$

in which \mathbf{A} is the magnetic vector potential and Φ is the electric scalar potential. The vector potential is given by

$$\mathbf{A}(\mathbf{r}) = \frac{\mu}{4\pi} \int_S \mathbf{J}(\mathbf{r}') \frac{e^{-jkR}}{R} dS', \quad (4.2)$$

and the scalar potential is

$$\Phi(\mathbf{r}) = j \frac{1}{\omega\mu\epsilon} \nabla \cdot \mathbf{A}, \quad (4.3)$$

where \mathbf{r} is the vector from the origin to the observation point, \mathbf{r}' is the vector from the origin to the source, and $R = |\mathbf{r} - \mathbf{r}'|$. Note that \mathbf{J} is a surface current. For a perfectly conducting surface, the boundary condition is $\hat{\mathbf{n}} \times (\mathbf{E}^i + \mathbf{E}^s) = 0$ on the interface S , giving

$$\mathbf{E}_{\text{tan}}^i = (j\omega\mathbf{A} + \nabla\Phi)_{\text{tan}}, \quad (4.4)$$

where $\mathbf{E}_{\text{tan}}^i$ is the tangential component of the incident field.

Equation (4.4) is referred to as the electric field integral equation (EFIE). Rao et al employed a special vector basis function set \mathbf{f}_n (the ‘‘RWG’’ basis set) to solve the

equation with the moment method. Fig. 4.1 shows two arbitrary adjacent triangles, T_n^+ and T_n^- . ρ_n^+ is the vector from the free vertex of T_n^+ to the position vector \mathbf{r} on T_n^+ and ρ_n^- is the vector from the position vector \mathbf{r} to the free vertex of T_n^- . Their common edge n is the n th interior edge on the surface. The RWG vector basis function associated with edge n is defined as

$$\mathbf{f}_n(\mathbf{r}) = \begin{cases} \frac{l_n}{2A_n^+} \rho_n^+ & , \mathbf{r} \text{ in } T_n^+ \\ \frac{l_n}{2A_n^-} \rho_n^- & , \mathbf{r} \text{ in } T_n^- \\ 0, & \text{otherwise} \end{cases} \quad (4.5)$$

where l_n is the length of the edge and A_n^\pm is the area of triangle T_n^\pm . This definition forces the component of current normal to the n th edge to be constant and continuous across the edge.

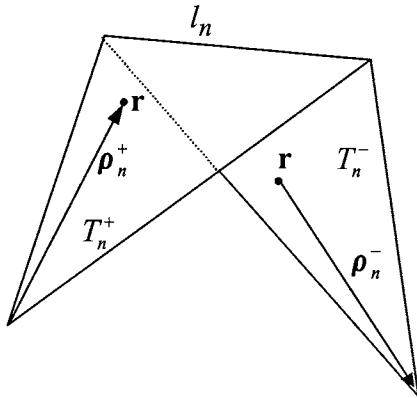


Fig. 4.1: Triangle pair and geometrical parameters associate with interior edge.

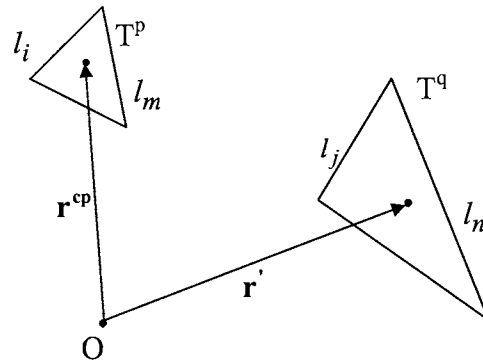


Fig. 4.2: Relationship between source triangle T^q and observation point in triangle T^p .

The complete current on S can be approximated in terms of an expansion of the RWG basis functions for all internal edges:

$$\mathbf{J} \approx \sum_{n=1}^N I_n \mathbf{f}_n(\mathbf{r}), \quad (4.6)$$

where N is the total number of interior edges of the complete surface S . Each coefficient I_n can be interpreted as the normal component of current density flowing across the n th edge. The current tangential to the edge is obtained from the basis functions associated with the other two edges of the patch. The I_n 's found using the moment method therefore describe the vector current everywhere on the surface. Note that the total current on a single triangular patch is the sum of three different basis function components.

The moment method is applied using Galerkin's method, where the testing functions are the same set $\mathbf{f}_n(\mathbf{r})$ as the basis functions. Setting the weighted residuals to zero as described in Section 2.1, yields

$$\langle \mathbf{E}^i, \mathbf{f}_m \rangle = j\omega \langle \mathbf{A}, \mathbf{f}_m \rangle + \langle \nabla \Phi, \mathbf{f}_m \rangle. \quad (4.7)$$

The inner product represents surface integration over the two triangles in which $\mathbf{f}_m(\mathbf{r})$ is defined. (4.7) gives N equations with N unknowns, which can be represented as

$$[\mathbf{Z}_{mn}][I_n] = [\mathbf{V}_m], \quad (4.8)$$

where $[\mathbf{Z}_{mn}]$ is an $N \times N$ matrix and $[I_n]$ and $[\mathbf{V}_m]$ are column vectors of length N .

Using the approximate relation

$$\int_{T_n^+ + T_n^-} \mathbf{f}_n dS \approx \frac{l_n}{2} (\rho_n^{c+} + \rho_n^{c-}) = l_n (r_n^{c+} + r_n^{c-}), \quad (4.9)$$

the elements of \mathbf{Z} and \mathbf{V} are given as

$$Z_{mn} = l_m \left[j\omega \left(\mathbf{A}_{mn}^+ \cdot \frac{\boldsymbol{\rho}_m^{c+}}{2} + \mathbf{A}_{mn}^- \cdot \frac{\boldsymbol{\rho}_m^{c-}}{2} \right) + \Phi_{mn}^- - \Phi_{mn}^+ \right], \quad (4.10a)$$

$$V_m = l_m \left(\mathbf{E}_m^+ \bullet \frac{\boldsymbol{\rho}_m^{c+}}{2} + \mathbf{E}_m^- \bullet \frac{\boldsymbol{\rho}_m^{c-}}{2} \right), \quad (4.10b)$$

where

$$\mathbf{A}_{mn}^{\pm} = \frac{\mu}{4\pi} \int_S \mathbf{f}_n(\mathbf{r}') \frac{e^{-jkR_m^{\pm}}}{R_m^{\pm}} dS', \quad (4.10c)$$

$$\Phi_{mn}^{\pm} = \frac{\mu}{4\pi j \omega \epsilon} \int_S \nabla'_s \bullet \mathbf{f}_n(\mathbf{r}') \frac{e^{-jkR_m^{\pm}}}{R_m^{\pm}} dS', \quad (4.10d)$$

$$R_m^{\pm} = \left| \mathbf{r}_m^{c\pm} - \mathbf{r}' \right|, \quad (4.10e)$$

$$\mathbf{E}_{mn}^{\pm} = \mathbf{E}^i(\mathbf{r}_m^{c\pm}), \quad (4.10f)$$

$\mathbf{r}_m^{c\pm}$ is the centroid vector of triangle T_n^{\pm} with respect to the coordinate origin, and $\boldsymbol{\rho}_m^{c\pm}$ is the vector $\boldsymbol{\rho}_n^{\pm}(\mathbf{r})$ when \mathbf{r} is located at $\mathbf{r}_m^{c\pm}$. $\mathbf{E}^i(\mathbf{r}_m^{c\pm})$ is the incident electrical field at $\mathbf{r}_m^{c\pm}$.

4.1.2 Numerical Implementation

Evaluation of each Z_{mn} associated with edge m and n involves integrations over triangles T_n^{\pm} with observation points located at the centroids of triangles T_m^{\pm} . Assuming that edge i lies on the same triangle as edge m and edge j lies on the same triangle as edge n , as shown in Fig. 4.2, calculation of Z_{ij} will obviously repeat an integration used in the formation of Z_{mn} . Thus, instead of performing the integrations for each edge individually, the face-pair approach of Rao et al [47,48], where the integral giving the interactions between each face pair are first found, and then linearly combined to form

the Z_{mn} 's. This procedure saves a factor of approximately 8 in the workloads to form the elements.

The integrations over the triangular faces are formed using the approach of Rao [47,48]. The arbitrary triangular patches are first mapped into a regular triangular area, and the integration is performed using multi-point quadrature. The singularity in the self-interaction where the source and the observation faces are the same was treated as in Rao [47]. For numerical accuracy, a 7-point quadrature was used for non-self-interactions, while 16 points were used for self-interactions [5,47,48]. Use of higher order quadrature did not improve accuracy significantly.

Once the excitation vector $[V_m]$ and interaction matrix $[Z_{mn}]$ elements have been found, (4.8) may be solved using standard linear algebra techniques.

4.1.3 Imperfectly Conducting Surfaces [49]

As in the 2-D case, when a finite conductivity scatterer is considered, an equivalent problem including a magnetic surface current must be treated. Adding the field radiated by the magnetic current to (4.1) and applying the boundary condition, yields the EFIE

$$\mathbf{E}_{\text{tan}}^i = \left(j\omega\mathbf{A} + \nabla\Phi + \frac{1}{\varepsilon}\nabla\times\mathbf{F} \right)_{\text{tan}}, \quad (4.11)$$

where \mathbf{F} is the electric vector potential associated with \mathbf{M} .

The numerical treatment of $\mathbf{E}_{\text{tan}}^i$ and the first two parts of the right hand side of (4.11) have already been considered. The new term is found from

$$\frac{1}{\varepsilon}\nabla\times\mathbf{F} = \frac{1}{4\pi}\nabla\times\int_S\mathbf{M}\frac{e^{-jkR}}{R}dS'. \quad (4.12)$$

As $\mathbf{r} \rightarrow S^-$, (4.12) becomes

$$\lim_{r \rightarrow S^-} \left(\frac{1}{\varepsilon} \nabla \times \mathbf{F} \right) = \frac{1}{2} \hat{\mathbf{n}} \times \mathbf{M} - \frac{1}{4\pi} \int_S \mathbf{M} \times \nabla \left(\frac{e^{-jkR}}{R} \right) dS'. \quad (4.13)$$

Once again, the magnetic current may be related to the electric current through

$$\hat{\mathbf{n}} \times \mathbf{M} = -Z_s \hat{\mathbf{n}} \times \mathbf{J} \quad (4.14)$$

when the scatterer meets the conditions of (2.13).

Substituting (4.14) and (4.13) into (4.12), the EFIE for an impedance surface is

$$\begin{aligned} \mathbf{E}_{\tan}^i = & \left[\frac{\mu}{4\pi} \int_S \mathbf{J} \frac{e^{-jkR}}{R} dS' + \frac{1}{4\pi\varepsilon} \int_S \sigma \frac{e^{-jkR}}{R} dS' \right]_{\tan} \\ & + \left[\frac{1}{2} Z_s \mathbf{J} + \frac{1}{4\pi} \int_S Z_s \left(\hat{\mathbf{n}}' \times \mathbf{J} \right) \times \nabla \left(\frac{e^{-jkR}}{R} \right) dS' \right]_{\tan}. \end{aligned} \quad (4.15)$$

Equation (4.15) can also be discretized using the moment method with RWG basis functions. Substituting in the basis expansion (4.6) and applying Galerkin's method weighting gives additional terms in the interaction matrix (beyond those for perfect conductivity). The final moment method system of linear equations is

$$\left\langle \frac{1}{2} Z_s \mathbf{J}, \mathbf{f}_m \right\rangle = \frac{1}{2} \sum_{n=1}^N I_n \left\{ \int_{T_m^+} Z_s [\mathbf{f}_n \cdot \mathbf{f}_m] dS + \int_{T_m^-} Z_s [\mathbf{f}_n \cdot \mathbf{f}_m] dS \right\}, \quad (4.16a)$$

$$\begin{aligned} \left\langle \frac{1}{4\pi} \int_S Z_s \left(\hat{\mathbf{n}}' \times \mathbf{J} \right) \times \nabla \left(\frac{e^{-jkR}}{R} \right) dS', \mathbf{f}_m \right\rangle = & \frac{1}{4\pi} \int_{T_m^+} \int_S \sum_{n=1}^N \left[I_n Z_s \hat{\mathbf{n}}' \times \mathbf{f}_n \right] \times \nabla \left(\frac{e^{-jkR}}{R} \right) dS' \cdot \mathbf{f}_m dS \\ & + \frac{1}{4\pi} \int_{T_m^-} \int_S \sum_{n=1}^N \left[I_n Z_s \hat{\mathbf{n}}' \times \mathbf{f}_n \right] \times \nabla \left(\frac{e^{-jkR}}{R} \right) dS' \cdot \mathbf{f}_m dS \end{aligned} \quad (4.16b)$$

Note that (4.16a) is zero unless the basis function \mathbf{f}_n and testing function \mathbf{f}_m overlap on a common triangular face. The double integral in (4.16b) can be approximated in the same manner as in the PEC EFIE, giving

$$\begin{aligned}
\left\langle \frac{1}{4\pi} \int_S Z_s \left(\hat{\mathbf{n}}' \times \mathbf{J} \right) \times \nabla \left(\frac{e^{-jkR}}{R} \right) dS', \mathbf{f}_m \right\rangle &\approx \frac{l_m}{2} \frac{1}{4\pi} \sum_{n=1}^N \left\{ \int_S Z_s \hat{\mathbf{n}}' \times \mathbf{f}_n \times \nabla \left(\frac{e^{-jk|\mathbf{r}' - \mathbf{r}_m^{c+}|}}{|\mathbf{r}' - \mathbf{r}_m^{c+}|} \right) dS' \bullet \boldsymbol{\rho}_m^{c+} \right. \\
&\quad \left. + \int_S Z_s \hat{\mathbf{n}}' \times \mathbf{f}_n \times \nabla \left(\frac{e^{-jk|\mathbf{r}' - \mathbf{r}_m^{c-}|}}{|\mathbf{r}' - \mathbf{r}_m^{c-}|} \right) dS' \bullet \boldsymbol{\rho}_m^{c-} \right\}
\end{aligned} \tag{4.17}$$

The far-field scattered electric field due to \mathbf{A} and \mathbf{F} can be written as

$$\mathbf{E}^s = \left(-j\omega A_\theta - \frac{1}{\varepsilon} jkF_\phi \right) \hat{\boldsymbol{\theta}} + \left(-j\omega A_\phi - \frac{1}{\varepsilon} jkF_\theta \right) \hat{\boldsymbol{\phi}}, \tag{4.18}$$

where A_θ, A_ϕ and F_θ, F_ϕ are the components of \mathbf{A} and \mathbf{F} in the θ and ϕ direction respectively. This can be rewritten as

$$E_\theta^s = -jk\eta \frac{e^{-jkr}}{4\pi r} \int_S \mathbf{J} \bullet \left[\hat{\boldsymbol{\theta}} + \frac{Z_s}{\eta} \left(\hat{\mathbf{n}}' \times \hat{\boldsymbol{\phi}} \right) \right] e^{jk(\hat{\mathbf{r}}' \bullet \hat{\mathbf{r}})} dS', \tag{4.19a}$$

$$E_\phi^s = -jk\eta \frac{e^{-jkr}}{4\pi r} \int_S \mathbf{J} \bullet \left[\hat{\boldsymbol{\phi}} - \frac{Z_s}{\eta} \left(\hat{\mathbf{n}}' \times \hat{\boldsymbol{\theta}} \right) \right] e^{jk(\hat{\mathbf{r}}' \bullet \hat{\mathbf{r}})} dS'. \tag{4.19b}$$

Once the scattered field is known, the polarization-dependent scattering cross section is given by

$$\sigma_{\alpha\beta} = 4\pi r^2 \frac{|E_\alpha|^2}{|E_\beta^{inc}|^2}, \tag{4.20}$$

where α and β are θ or ϕ . The integrations in (4.19) are performed numerically using the final MM current solution.

4.1.4 Implementation Testing

The implementation of the RWG-based MM was tested with sample scatterer geometries. The first considered was a flat plate as shown in Fig. 4.3a. The plate is assumed to be perfectly conducting, and is a 1λ by 1λ square. It was divided into a grid, and each grid cell was bisected to yield the triangular patches. The stars denote the centers of interior edges.

Fig. 4.3b shows the calculated current with different grid sizes. The incident direction was perpendicular to the flat plate, and the incident field has only an x component ($\mathbf{E}_{\text{inc}} = \hat{a}_x 1.0$). The starred-dashed line in Fig. 4.3b corresponds to a 6 by 7 grid used in the moment method, the solid-circle line with a 6 by 9 grid, the solid-cross line with a 6 by 11 grid, the dashed-circle line with an 8 by 7 grid, and the dashed-crossed line with a 10 by 7 grid. The solid lines show the currents along the cut from point A to A' in Fig. 4.3a, and the dashed lines show the current along the cut from B to B'. The current clearly converges as the discretization of the surface is made finer. Moreover, the 6 by 7 grid results show excellent agreement with Fig. 6 of [48].

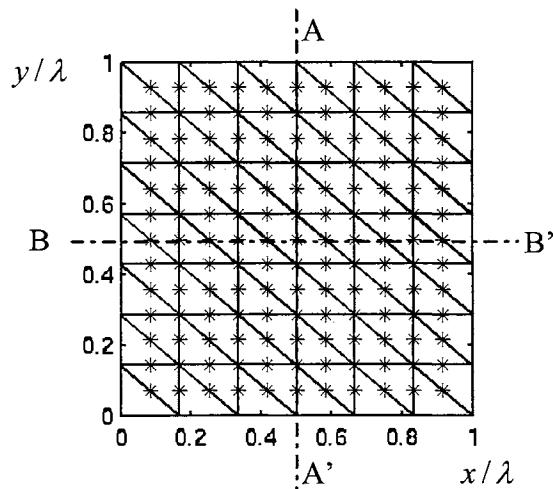


Fig. 4.3a: Segmentation of flat plate. ($N_x=6$, $N_y=7$)

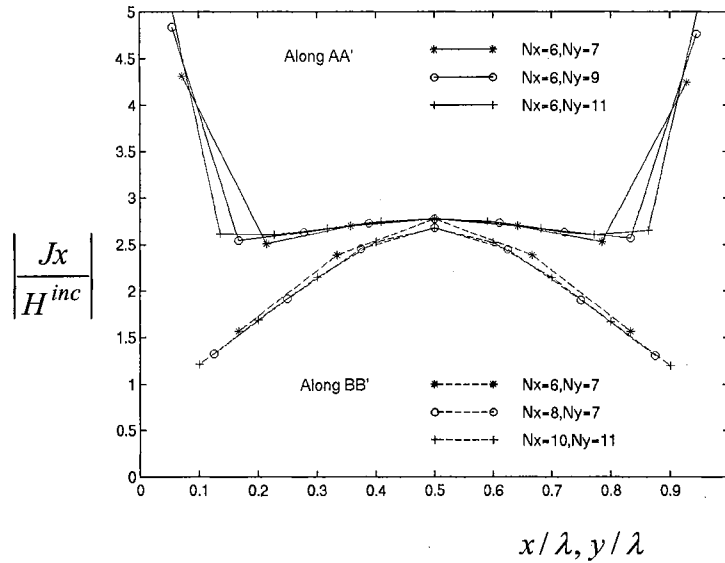


Fig. 4.3b: Results of a PEC square with different segmentation numbers.

The second test case considered was the disk shown in Fig. 4.4a. The 56 triangular patches used are shown, with the interior edges marked by stars. The incident direction was perpendicular to the disk, and the incident field again had only an x component

($\hat{\mathbf{E}}_{\text{inc}} = a_x \hat{1.0}$). Fig. 4.4b shows the numerically found current from point A to point A'.

The circled line represents a 1λ radius disk, the crossed line a 0.1λ radius, and the starred line a 0.05λ radius. Again, excellent agreement is achieved with Fig. 9 of [48].

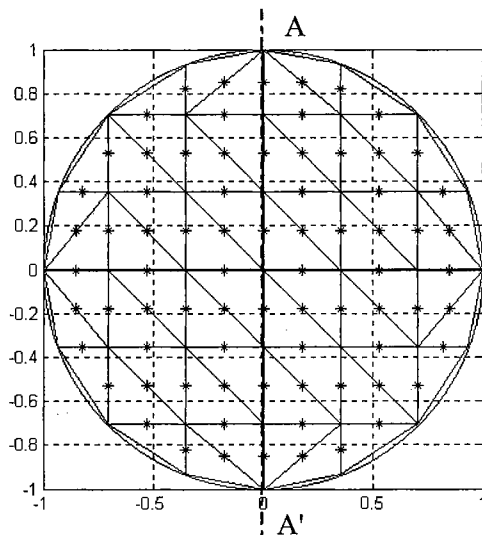


Fig. 4.4a: Segmentation of a disk.

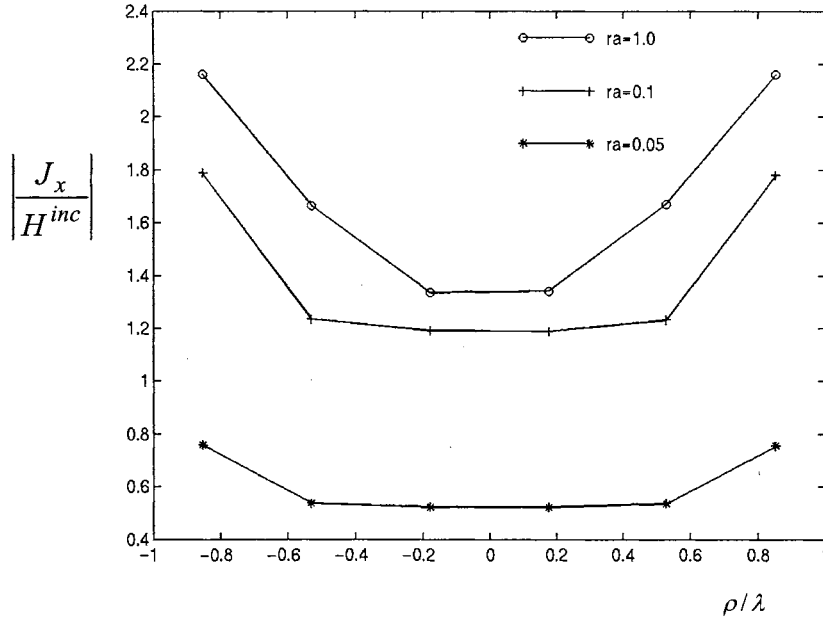


Fig. 4.4 b: Results of PEC disk with different radius.

The final test cases were based on a spherical scatterer, as shown in Fig. 4.5a. Shown is the triangular segmentation used, consisting of 120 patches. The sampling used in ϕ is independent of θ , so the polar regions are more finely sampled. Note that all edges are interior edges. Fig. 4.5b shows the results with a perfectly conducting sphere. Plotted is the normalized monostatic radar cross-section (RCS) (σ/λ^2) versus the free space wave number times the sphere radius (ka). The solid line shows the exact RCS that was calculated according to a Mie series solution [1], while the dashed line shows the RWG MM results. The results compare well with Fig. 5 of [49]. Note that at small radii the agreement between the exact and MM result is very good. However, as ka exceeds about 3, the positions of the relative maximum and minima are shifted. This results because the sampling of the surface is insufficient at the larger radii. At $ka = 3.5$, the average length of the patches is about 0.25λ . This is too large for fine accuracy [49]. In all following

cases the maximum dimensions of the patches will be limited to a maximum of 0.1λ to maintain accuracy.

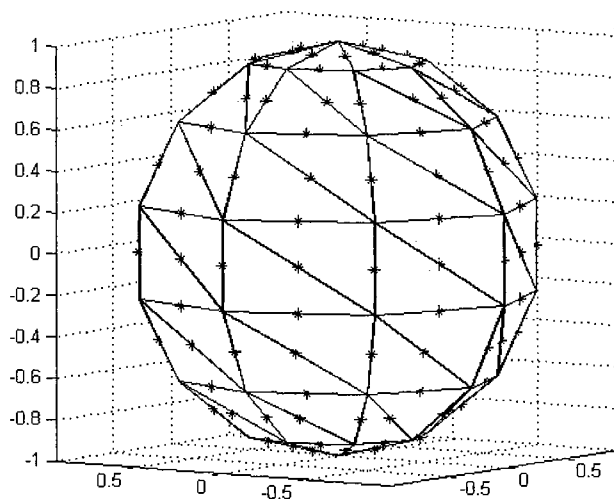


Fig. 4.5a: Segmentation of a sphere.

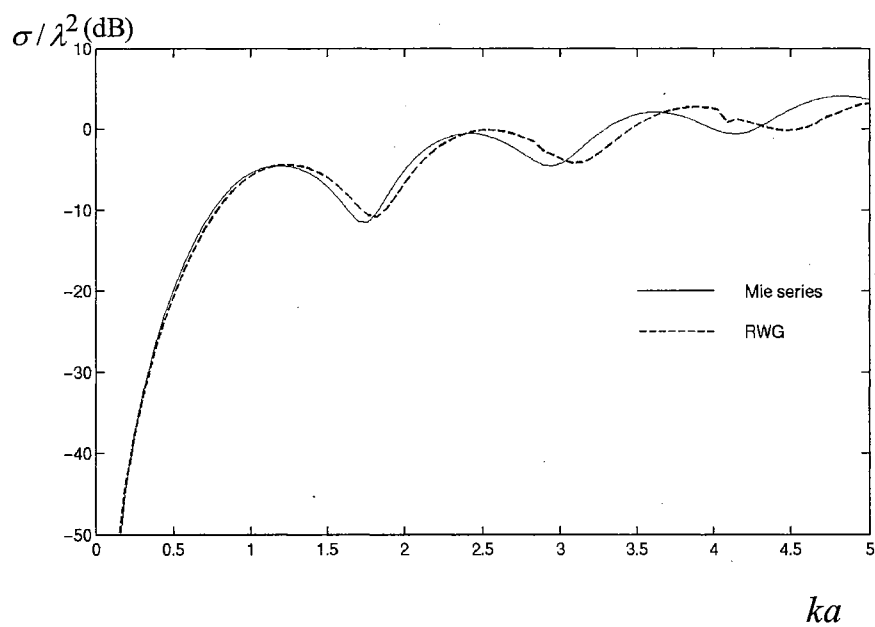


Fig. 4.5b: Monostatic scattering cross section for PEC spheres as a function of ka .

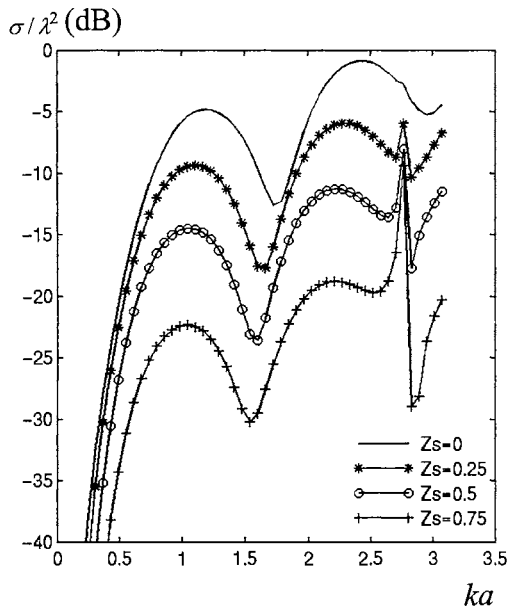


Fig. 4.5c: Monostatic scattering cross section for impedance spheres as a function of ka using 120 patches.

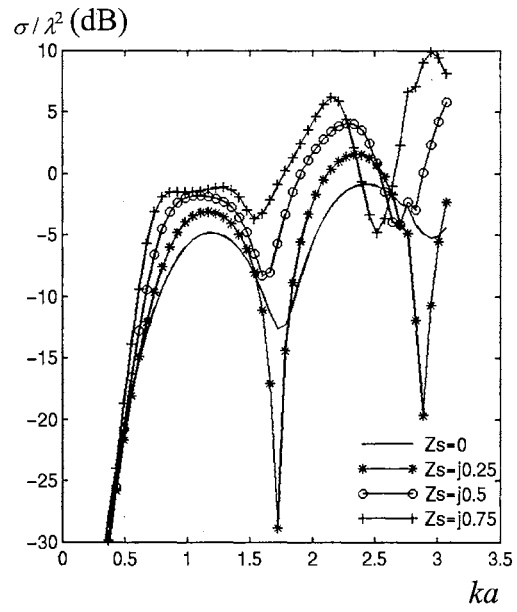


Fig. 4.5d: Monostatic scattering cross section for purely imaginary impedance spheres as a function of ka using 120 patches.

The impedance boundary implementation of the RWG moment method was tested by considering spheres with different surface impedances. The results are shown in Fig. 4.5c and 4.5d. In Fig. 4.5c, the $Z_s = 0$ case is denoted by the solid line, $Z_s = 0.25\eta_0$ with the starred line, $Z_s = 0.5\eta_0$ with the circled line, and $Z_s = 0.75\eta_0$ with the crossed line. Fig 4.5d is the results when purely imaginary surface impedances were used. Here, the solid line indicates $Z_s = 0$, the starred line is $Z_s = j0.25\eta_0$, the circled line is $Z_s = j0.5\eta_0$, and the crossed line is $Z_s = j0.75\eta_0$. Very good agreement with Fig. 4 and Fig. 6 of [49] shows that the impedance boundary RWG MM has been properly implemented.

4.2 Fast Multipole Method (FMM) [52-57]

Direct application of the moment method to 3-D surfaces quickly becomes cost prohibitive as the scattering surface increases in size. Doubling the dimensions of the scatterer gives a factor of 4 increase in the number of unknowns N that must be found using the same sampling size. The size of the interaction matrix is N^2 , so doubling the physical dimensions increases the size of the interaction matrix by a factor of 16. Finally, direct solution of the linear system using matrix factorization is order of $O(N^3)$, so doubling the dimensions gives a 64-fold computational increase. Iterative solution is $O(N^2)$, so still gives a 16-fold increase.

The fast multipole method (FMM) was introduced to decrease the computational expense of the moment method, both in terms of storage and computation. It accomplishes this by dividing the surface elements into groups. The interactions between elements in nearby groups are found directly using the standard moment method. However, the interactions between groups that are sufficiently separated are found simultaneously. Group-to-group interactions are found using a plane wave expansion of the radiation of all elements within the source group. The field at the center of the observation group is then shifted to the individual elements.

The foundation of FMM is two identities. The first is the expansion of the free space Green's function using Gegenbauer's addition theorem. As shown in Fig. 4.6,

$$|\mathbf{r} - \mathbf{r}'| = |\mathbf{x} + \mathbf{d}|. \quad (4.21)$$

Assuming $|\mathbf{x}|$ is much larger than $|\mathbf{d}|$, the Green's function

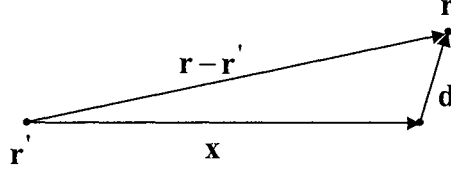


Fig. 4.6: Relationship between vector \mathbf{r}' , \mathbf{r} , \mathbf{x} and \mathbf{d} .

$$G(\mathbf{r}, \mathbf{r}') = \frac{e^{jk|\mathbf{r}-\mathbf{r}'|}}{|\mathbf{r}-\mathbf{r}'|} = \frac{e^{jk|\mathbf{x}+\mathbf{d}|}}{|\mathbf{x}+\mathbf{d}|} \quad (4.22)$$

can be expanded by Gegenbauer's addition theorem as

$$G(\mathbf{r}, \mathbf{r}') = \frac{e^{jk|\mathbf{x}+\mathbf{d}|}}{|\mathbf{x}+\mathbf{d}|} = ik \sum_{l=0}^{\infty} (-1)^l (2l+1) j_l(kd) h_l^{(1)}(k|\mathbf{x}|) P_l(\hat{\mathbf{d}} \cdot \hat{\mathbf{x}}), \quad (4.23)$$

where $j_l(\cdot)$ is the first kind spherical Bessel function, $h_l^{(1)}(\cdot)$ is the first kind spherical Hankel function, and $P_l(\cdot)$ is the Legendre polynomial.

The second identity used by FMM is the expansion of $j_l(kd) P_l(\hat{\mathbf{d}} \cdot \hat{\mathbf{x}})$ in an integration of propagating plane waves:

$$j_l(kd) P_l(\hat{\mathbf{d}} \cdot \hat{\mathbf{x}}) = \frac{1}{4\pi i^l} \int e^{i\mathbf{k} \cdot \mathbf{d}} P_l(\hat{\mathbf{k}} \cdot \hat{\mathbf{x}}) d^2k. \quad (4.24)$$

(4.24) is in fact a 2-D Fourier transform. Substitution of (4.24) into (4.23) yields

$$G(\mathbf{r}, \mathbf{r}') = \frac{ik}{4\pi} \int d^2k e^{i\mathbf{k} \cdot \mathbf{d}} \sum_{l=0}^{\infty} (i)^l (2l+1) h_l^{(1)}(k|\mathbf{x}|) P_l(\hat{\mathbf{k}} \cdot \hat{\mathbf{x}}). \quad (4.25)$$

The summation on the right hand side of (4.25) is a function of $k|\mathbf{x}|$ and $\hat{\mathbf{k}} \cdot \hat{\mathbf{x}}$. It is denoted by the translation operator

$$T(k|\mathbf{x}|, \hat{\mathbf{k}} \cdot \hat{\mathbf{x}}) = \sum_{l=0}^{\infty} (i)^l (2l+1) h_l^{(1)}(k|\mathbf{x}|) P_l(\hat{\mathbf{k}} \cdot \hat{\mathbf{x}}). \quad (4.26a)$$

Obviously, it will not be realistic to perform infinite summations in a numerical implementation, so the series in (4.26a) must be truncated. Fortunately, the convergence of the series is well behaved and guidelines for the accuracy required versus the upper limit L used exist (and will be summarized later). The notation $T_L()$, indicating that the series has been truncated at $l = L$, will be used hereafter:

$$T_L(k|\mathbf{x}|, \hat{\mathbf{k}} \bullet \hat{\mathbf{x}}) = \sum_{l=0}^L (i)^l (2l+1) h_l^{(1)}(k|\mathbf{x}|) P_l(\hat{\mathbf{k}} \bullet \hat{\mathbf{x}}). \quad (4.26b)$$

The benefit of FMM is that the translation operators $T_L()$ between groups can be pre-computed before the iterative solution.

Assuming for now that the interactions between elements can be fully described by the scalar Green's function, the interaction elements become

$$Z_{mn} = A \int d\mathbf{r} f_m(\mathbf{r}) \int d\mathbf{r}' f_n(\mathbf{r}') G(\mathbf{r}, \mathbf{r}'), \quad (4.27)$$

where A is a constant and $f_m(\mathbf{r})$ and $f_n(\mathbf{r}')$ are the weighting function and testing functions respectively (assumed to be the same for RWG basis functions). Using (4.25) and (4.26b), (4.27) can be approximated as

$$Z_{mn} \approx B \int d\mathbf{r} f_m(\mathbf{r}) \int d\mathbf{r}' f_n(\mathbf{r}') \int d^2k e^{i\mathbf{k} \bullet \mathbf{d}} T_L(k|\mathbf{x}|, \hat{\mathbf{k}} \bullet \hat{\mathbf{x}}), \quad (4.28)$$

where B is a constant.

The approximate equality in (4.28) is due to the finite number of terms L in $T_L()$. The required L for adequate accuracy depends on the size of $|\mathbf{d}|$ with respect to $|\mathbf{x}|$. $|\mathbf{x}|$ is assumed to be the distance between the centers of groups in which the source and observation points are located. $|\mathbf{d}|$ is the distance from the group center to the individual

elements. The value of L therefore determines whether the groups must be considered near or far.

Using (4.28), (4.8) may now be rewritten in a form suitable for iterative solution:

$$V_m = \sum_{\substack{\text{near} \\ \text{elements}}} Z_{mn} I_n + \sum_{\substack{\text{far} \\ \text{elements}}} I_n B \int d\mathbf{r} f_m(\mathbf{r}) \int d\mathbf{r}' f_n(\mathbf{r}') \int d^2 k e^{i\mathbf{k} \cdot \mathbf{d}} T_L(k|\mathbf{x}|, \hat{\mathbf{k}} \cdot \hat{\mathbf{x}}). \quad (4.29)$$

Setting

$$\mathbf{d} = \mathbf{r} - \mathbf{r}' - \mathbf{x} = \mathbf{r} - \mathbf{r}' - (\mathbf{r}_{cA} - \mathbf{r}_{cB}) = (\mathbf{r} - \mathbf{r}_{cA}) - (\mathbf{r}' - \mathbf{r}_{cB}), \quad (4.30)$$

where \mathbf{r} falls within the group whose center is \mathbf{r}_{cA} , \mathbf{r}' is within the group whose center is \mathbf{r}_{cB} , and $\mathbf{x} = \mathbf{r}_{cA} - \mathbf{r}_{cB} = \mathbf{r}_{AB}$, (4.29) can be rewritten as

$$V_m = \sum_{\substack{n \text{ is} \\ \text{neaby}}} Z_{mn} I_n + \sum_{\substack{n \text{ is not} \\ \text{nearby}}} I_n B \int d^2 k \left[\int d\mathbf{r} (f_m(\mathbf{r}) e^{i\mathbf{k} \cdot (\mathbf{r} - \mathbf{r}_{cA})}) \right] \left[\int d\mathbf{r}' (f_n(\mathbf{r}') e^{-i\mathbf{k} \cdot (\mathbf{r}' - \mathbf{r}_{cB})}) \right] T_L(k|\mathbf{r}_{AB}|, \hat{\mathbf{k}} \cdot \hat{\mathbf{r}}_{AB}) \quad (4.31)$$

The first part of the right hand side of (4.31) gives the interactions between elements in nearby groups. These interactions are stored in a sparse matrix. The second term of the right hand side includes three steps, i.e. shifting the references of the source elements radiation to the group center, translating the complete group radiation to other groups using the operator T_L , and shifting the group interactions from the observation group center to the individual observation elements. More details will be given in the description of the implementation.

(4.31) is still in a form that can be iteratively solved. At first glance, it appears that (4.31) is much more complicated than (4.8). But in fact, it allows a dramatic computational savings. If elements m and m' fall within the same group and n and n'

fall in another (far) group, Z_{mn} , $Z_{mn'}$, $Z_{m'n}$ and $Z_{m'n'}$ all use the same translation operator $T_L()$, which need only be applied once.

4.3 Implementation of Fast Multipole Method (FMM) [56]

4.3.1 Implementation Steps of FMM

The FMM is implemented in five steps:

1) Grouping

An element-grouping scheme is shown in Fig. 4. 7a. For convenience, a flat plate is shown here although the surface can be arbitrary as in Fig. 4.7b. First, the surface is approximated by triangular patches using a segmentation length of about 0.1λ . The edges are then collected into M separate groups. The “radii” of the groups are then found from the maximum distance a triangle within the group is from the centroid of the group. Now, the number of terms L that are maintained in the translation operator of (4.26b) is determined from [64]

$$L = 2k\rho_{\max} + \frac{D}{1.6} \ln(2k\rho_{\max} + \pi), \quad (4.32)$$

where ρ_{\max} is the maximum “radius” among all the groups and D is the number of significant digits to which accuracy is desired. (4.32) was determined empirically by Rokhlin [55]. The effect of D will be considered in the following test cases. The criteria for setting near or far groups is expressed as

$$k|\mathbf{r}_{\mathbf{cA}} - \mathbf{r}_{\mathbf{cB}}| \begin{cases} \geq L, & \Rightarrow \text{group A and group B are far groups} \\ < L, & \Rightarrow \text{group A and group B are near groups} \end{cases} \quad (4.33)$$

where $\mathbf{r}_{\mathbf{cA}}$ and $\mathbf{r}_{\mathbf{cB}}$ are the centers of groups A and B respectively.

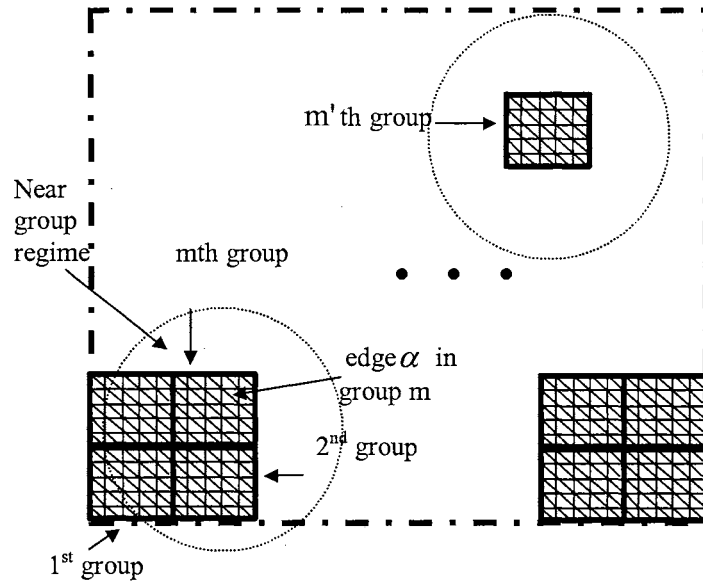


Fig. 4.7a: Relationship between groups and edges.

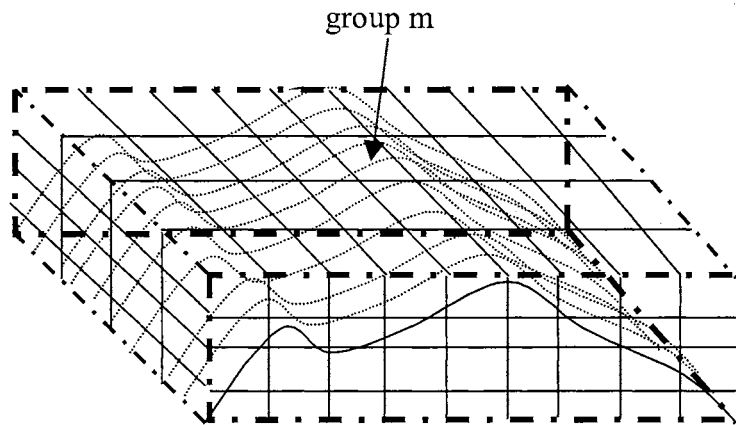


Fig. 4.7b: Groups for 3-D arbitrary surface.

The size of each group will affect the computation load. The larger the group size, the fewer the total number of groups, reduce the computation load in calculating $T_L()$. However, more edges will be included in nearby groups, increasing the number of entries in the first term of the right hand side of (4.31) (the sparse matrix). On the other hand, too small a group size will result in a large number of groups for which $T_L()$ must be found. [56] showed that the optimal scaling is achieved when $M \approx \sqrt{N}$, where M is the

number of groups and N is the total number of unknowns. The system scales as $O(N^{1.5})$ in this case. Fig. 4.7b shows a sample 3-D grouping.

2) Sparse Matrix Filling

The interactions matrix entries between elements that are within nearby groups are calculated and stored. This is accomplished by directly evaluating (4.10) or (4.15). The entries are stored in a sparse matrix format to save memory. This implementation uses the compressed row storage (CRS) format [70].

3) Translation Operators $T_L()$

The translation operators between the far groups are then found. From (4.26), \mathbf{x} is first replaced by $\mathbf{r}_{mm'} = \mathbf{r}_{cm} - \mathbf{r}_{cm'}$, where \mathbf{r}_{cm} is the center of observation group m and $\mathbf{r}_{cm'}$ is the center of source group m' . $T_L()$ is a function of wave number \hat{k} , over which a continuous integral must be computed in (4.31). $T_L()$ is therefore computed at a discrete number of \hat{k} values. The \hat{k} values are uniformly spaced in the ϕ coordinate. In the θ coordinate, the \hat{k} vectors are non-uniformly spaced, corresponding to the nodes of a Gauss-Legendre quadrature [55]. This allows the integral in (4.31) to be accurately evaluated from the discrete \hat{k} values. Sampling theory shows that $K = 2L^2$ samples should be used in both θ and ϕ directions [64]. The final translation operations are therefore

$$T_{mm'}(m, m', \hat{k}) = \frac{k}{(4\pi)^2} \sum_{l=0}^L (i)^l (2l+1) h_l^{(1)}(k|\mathbf{r}_{mm'}|) P_l(\hat{\mathbf{k}} \cdot \hat{\mathbf{r}}_{mm'}). \quad (4.34)$$

This translation operator $T_L()$ occupies considerable memory. In theory, there are $2M(M-1)$ $\mathbf{r}_{mm'}$ vectors, but using uniform grouping the translation operators may be reused. If $\mathbf{r}_{mm'} = \mathbf{r}_{ij}$, the same $T_L()$ is used even though, $m \neq i$, $m' \neq j$. This technique substantially reduces the memory needed to store $T_L()$.

4) Shifting Operators

The second term of the right hand side of (4.31) includes two shifting operators written as

$$\mathbf{V}_{\mathbf{fm}\alpha}(\hat{k}) = \int d\mathbf{r} \left(\mathbf{f}_{\mathbf{n}}(\mathbf{r}) e^{i\mathbf{k} \cdot (\mathbf{r} - \mathbf{r}_{cm})} \right), \quad (4.35a)$$

and

$$\mathbf{V}_{\mathbf{sm}\alpha}(\hat{k}) = (\mathbf{V}_{\mathbf{fm}\alpha})^*. \quad (4.35b)$$

These were derived using a scalar Green's function. Since the electric field and surface current are vectors, $\mathbf{V}_{\mathbf{fm}\alpha}$ and $\mathbf{V}_{\mathbf{sm}\alpha}$ are vector operators. With RWG basis functions with a PEC surface, the scalar Green's function $G(\mathbf{r}, \mathbf{r}')$ is replaced by

$\left(G - \frac{1}{k^2} \nabla \cdot \nabla G \right)$. Using this, (4.35a) is replaced by

$$\mathbf{V}_{\mathbf{fm}\alpha}(\hat{k}) = \int d\mathbf{r} \left(\mathbf{f}_{\mathbf{n}}(\mathbf{r}) - \hat{k}(\hat{k} \cdot \mathbf{f}_{\mathbf{n}}(\mathbf{r})) \right) e^{i\mathbf{k} \cdot (\mathbf{r} - \mathbf{r}_{cm})}. \quad (4.36)$$

(4.35b) is still valid.

Shift operators are similarly derived for finite conductivity surfaces from (4.15), giving

$$\mathbf{V}_{\text{sm}\alpha}(\hat{k}) = \int d\mathbf{r} \left(\mathbf{f}_{\mathbf{n}}(\mathbf{r}) - \hat{k}(\hat{k} \cdot \mathbf{f}_{\mathbf{n}}(\mathbf{r})) \right) e^{-i\mathbf{k} \cdot (\mathbf{r} - \mathbf{r}_{cm})}, \quad (4.37a)$$

$$\mathbf{V}_{\text{fm}\alpha}(\hat{k}) = \int d\mathbf{r} \left(\mathbf{f}_{\mathbf{n}}(\mathbf{r}) - \hat{k}(\hat{k} \cdot \mathbf{f}_{\mathbf{n}}(\mathbf{r})) \right) e^{i\mathbf{k} \cdot (\mathbf{r} - \mathbf{r}_{cm})} - \frac{Z_s}{\eta_0} \hat{k} \times \int d\mathbf{r} \left(\mathbf{f}_{\mathbf{n}}(\mathbf{r}) \times \hat{n} \right) e^{i\mathbf{k} \cdot (\mathbf{r} - \mathbf{r}_{cm})}, \quad (4.37b)$$

where \hat{n} is the external normal to the surface of the triangle over which the integration is being performed.

The translation operator $T_L()$ is unchanged for PEC and impedance surfaces.

5) Solution

(4.8) can now be written as

$$V_{m\alpha} = \sum_{m' \in B_m} Z_{mcm'\alpha'} I_{m'\alpha'} + \omega\mu \int d^2 \hat{k} \left\{ \mathbf{V}_{\text{fm}\alpha}(\hat{k}) \cdot \left[\sum_{m' \notin B_m} T(m, m', \hat{k}) \left(\sum_{\alpha' \in G_{m'}} \mathbf{V}_{\text{sm}'\alpha'}(\hat{k}) I_{m'\alpha'} \right) \right] \right\}, \quad (4.38)$$

in which B_m denotes all groups near group m . $G_{m'}$ stands for group m' . (4.38) is a form that can be iteratively solved.

Computational cost of FMM analysis

When the total number of unknowns is N , it can be shown that FMM is most efficient with number of groups $M \approx \sqrt{N}$. There are therefore approximately \sqrt{N} unknowns in each group. This leads to $L = \sqrt{N}/M$ and $K = N/M$. Step (2) therefore requires $O(N)$ operations, step (3) requires $O(N^2/M \approx N^{3/2})$ operations, and step (4) requires order $O(N^{3/2})$ operations. FMM is therefore $O(N^{3/2})$ overall, versus $O(N^2)$ for direct iterative solution of (4.8).

4.3.2 Iterative Algorithm

Sultan and Mittra [89] first applied conjugate gradient iterative solution to MM based scattering. West and Sturm [73] then applied several more modern conjugate gradient based schemes for non-Hermitian, complex matrix systems to rough surface scattering. Two of the more promising schemes from that study were considered for use with FMM: the generalized minimal residual (GMRES) and bi-conjugate gradient-stable (BICGSTAB) algorithms. These are especially appropriate for FMM since they do not require the transpose of the interaction matrix, which is not available with FMM. The convergence history of each when applied to scattering from a flat-plate (4 by 4 groups, 20 by 20 grids with 0.1λ segmentation) is shown in Fig. 4.8. The solid line was found using BICGSTAB and the dashed line was found with GMRES. Both algorithms show good convergence properties, although GMRES converges more uniformly and more quickly. The primary disadvantage of GMRES is that it requires more work per iteration and larger storage. However, these are small compared to the workload and storage of FMM itself. GMRES is therefore used for the remainder of this work.

4.3.3 Test Cases for FMM

The FMM implementation with RWG basis functions was first tested through an application to a PEC flat-plate. The segmentation is similar to Fig. 4.3a, except that the size is enlarged to 2λ by 2λ , the grid length is still 0.1λ in both directions. The incoming field was the same as in Fig. 4.3a.

The results are shown in Fig. 4.9. The solid line shows the current along the segment AA' in Fig. 4.3a when the moment method system was solved directly using matrix

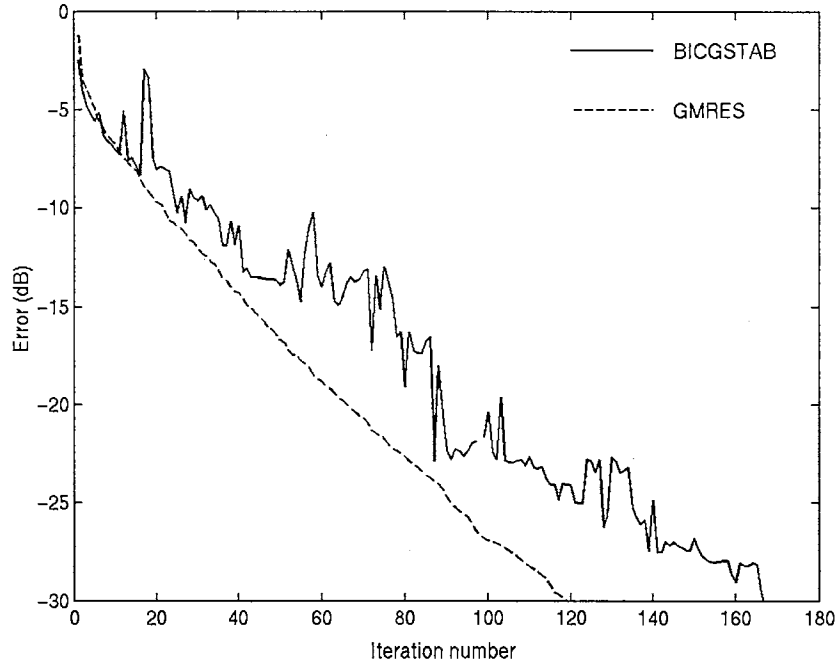


Fig. 4.8. Comparison between BICGSTAB and GMRES.

factorizations. This can be treated as the exact solution. The circle-dashed line shows the FMM current when $D = 3$ in (4.32), and $D = 2$ is shown as the starred line. The agreement is very good in all cases. The slight error in $D = 2$ at element 5 will not lead to significant errors in the far field scattering since the scattered field is an integration of the current. $D = 2$ is therefore adequate for the remainder of the calculations.

The second test case was a PEC sphere of radius 0.5λ . A segmentation of 30 in both the θ and ϕ coordinates was used, giving 1740 triangular patches. The calculated current is shown in Fig. 4.9b. For convenience, the results only show the currents for first 120 edges. The solid line shows the reference MM current using matrix factorization, while the circled and starred lines correspond to FMM with $D = 3$ and $D = 2$ respectively. Excellent agreement is achieved at all but the lowest current levels. Again, this will have negligible effects on the far field scattering.

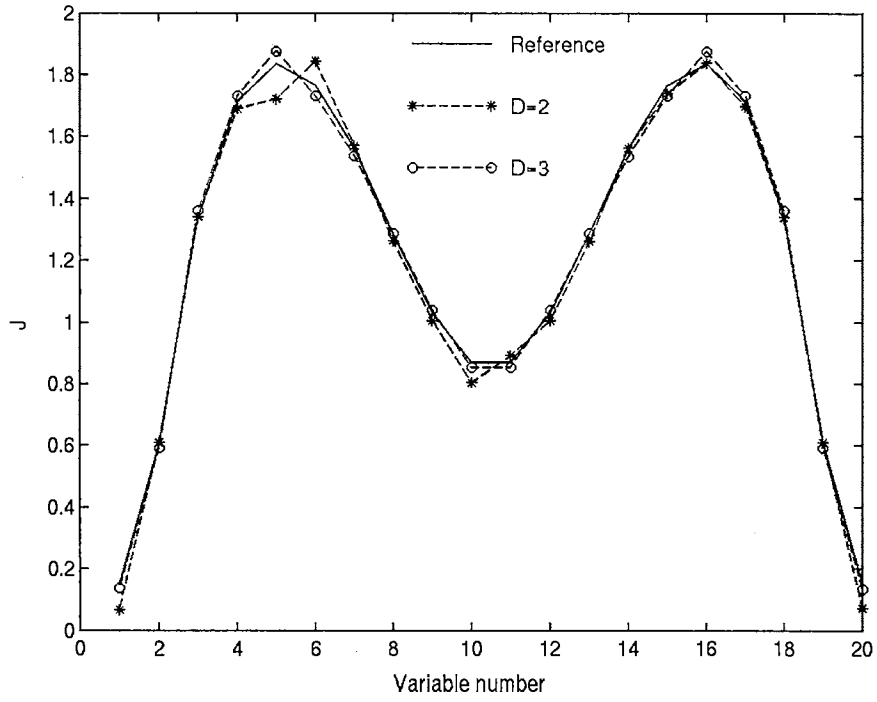


Fig. 4.9a: Results with different D for a flat plate.

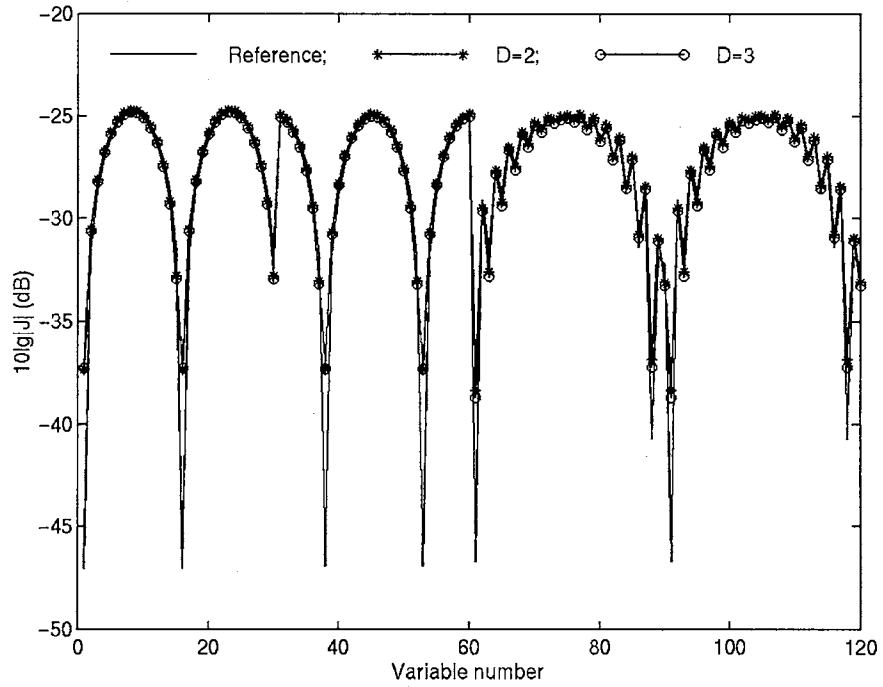


Fig. 4.9b: Results of PEC sphere by using FMM.

4.4 Multilevel Fast Multipole Algorithm (MLFMA) [58-67]

The multi-level fast multipole algorithm (MLFMA) further expands upon the FMM concept to give even greater computational efficiency. It accomplishes this by subdividing the FMM groups into smaller groups, and independently applying FMM at the finer level. The basic scheme is shown in Fig. 4.10. Fig. 4.10 illustrates 3 levels, but it is straight forward to extend to an arbitrary number of levels. The top level (level L_g) is the coarsest level, while the lowest level (level 1) is the finest level. Each group in level l includes a number of children groups from level $l-1$. The number of groups that are included in the parent group is determined by the grouping size at each level. The figure shows four children groups per parent group, but the number is arbitrary. The upward tree is defined from the finest level to the coarsest (1 to L_g), while L_g to level 1 is the downward tree. Because the number of moment method triangles in the groups is different at each level, the L and K associated with each level is also different. The values for level l are specified by L_l and K_l .

The grouping is largest at the top level, so the maximum number of elements translate at once through a $T_L()$. However, large numbers of elements would be left in nearby groups if only the highest level were used. Instead, the children groups that are in nearby groups at parent level l are treated in their own child level $l-1$ FMM expansion. This continues down to level 1.

A different number of plane waves K_l are used in the FMM expansion at each level. The lower level groups must therefore be combined into larger groups and the plane wave expansion interpolated into large expansions in an aggregation step. After the translations

are performed, the groups must then be divided into the lower levels, and the plane waves filtered to fewer samples. This is the dis-aggregation step. These are briefly described below.

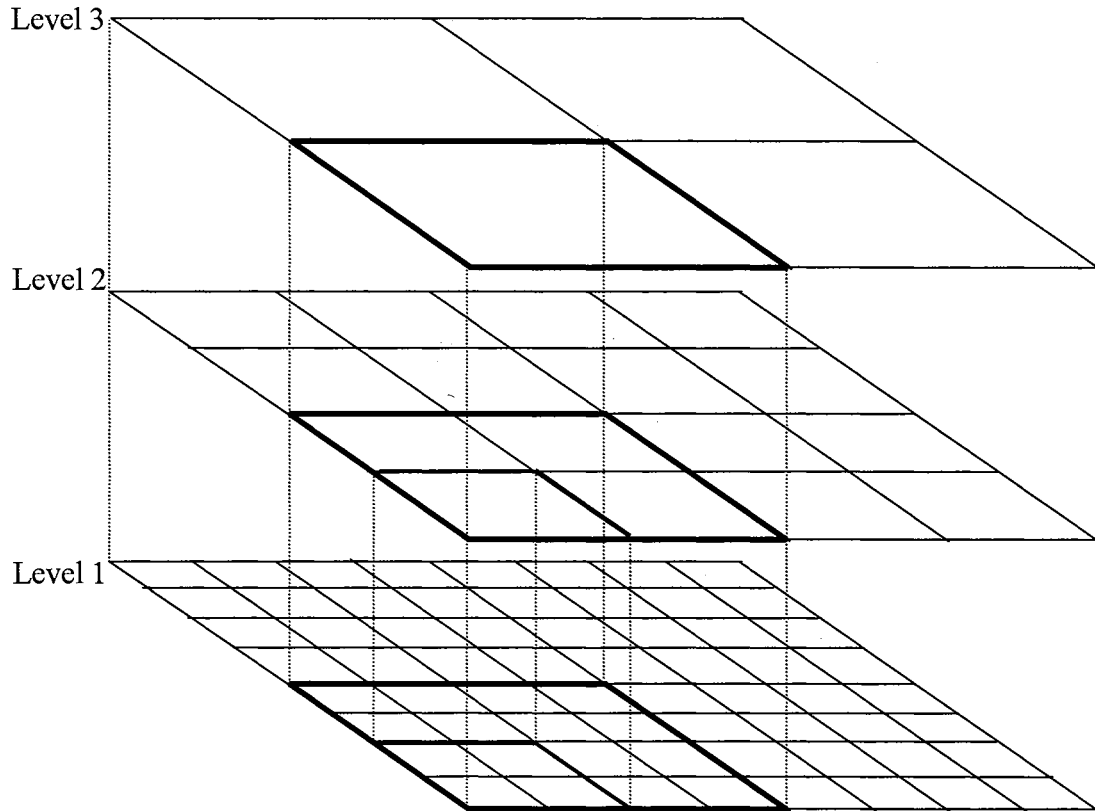


Fig. 4.10: Tree structure of multi-level grouping.

4.4.1 Implementation of MLFMA

Compared with FMM, MLFMA has two main additional steps: the aggregation step and the dis-aggregation step.

1) Aggregation Step

The aggregation step combines the K_{l-1} plane waves in the children groups into K_l plane waves in the corresponding parent group. To demonstrate this, the term $\hat{s}_{m_l}(\hat{k})$ is introduced:

$$\mathbf{s}_{m'_l}(\hat{k}_l) = \sum_{\alpha'_l \in G_{m'_l}} \mathbf{V}_{\mathbf{s}m'_l\alpha'_l}(\hat{k}_l) I_{m'_l\alpha'_l}, \quad \text{for } m'_l = 1, 2, \dots, M_l. \quad (4.39)$$

where M_l is the number of groups in level l . $\mathbf{s}_{m'_l}(\hat{k}_l)$ is therefore the plane wave in the direction \hat{k}_l due to all elements within the group $G_{m'_l}$. The $\mathbf{s}_{m'_l}(\hat{k}_l)$'s are translated to an observation group in level l via $T_{L_l}()$.

Direct calculation of $\mathbf{s}_{m'_l}(\hat{k}_l)$ from the individual elements in the group would be inefficient. Instead, $\mathbf{s}_{m'_l}(\hat{k}_l)$ is formed as a sum of plane waves from the children groups, shifted to the appropriate phase reference at the center of the parent group. Examining a single child group, the contribution to the parent group is

$$\delta \mathbf{s}_{m'_l}(\hat{k}_l) = e^{-j\mathbf{k} \cdot (\mathbf{r}_{cm'_l} - \mathbf{r}_{cm'_{l-1}})} \left(\mathbf{s}_{m'_{l-1}}(\hat{k}_l) \right). \quad (4.40)$$

The contributions from all children groups are added to give the complete plane wave expansion. It is noted that equation (4.40) requires that a plane wave in the \hat{k}_l direction be known in $l-1$ level. As mentioned above, fewer plane waves are stored at level $l-1$ than at level l . The level $l-1$ plane wave expansion must therefore be interpolated from the \hat{k}_{l-1} directions to the \hat{k}_l directions. Mathematically, this can be written as

$$\mathbf{s}_{m'_l}(\hat{k}_l) = \sum_{\substack{\text{child} \\ \text{groups}}} e^{-j\mathbf{k} \cdot (\mathbf{r}_{cm'_l} - \mathbf{r}_{cm'_{l-1}})} \sum_{1 \text{ to } K_{l-1}} \mathbf{W}_{l-1,l} \left(\mathbf{s}_{m'_{l-1}}(\hat{k}_{l-1}) \right), \quad (4.41)$$

for $l = 2, 3, \dots, L_g$

where \mathbf{r}_{cm^l} is the centroid vector of the group m^l at level l . $\mathbf{W}_{l-1,l}$ are interpolation coefficients from level $l-1$ to level l . This interpolation and shifting [64] can be illustrated by using Fig. 4.11.

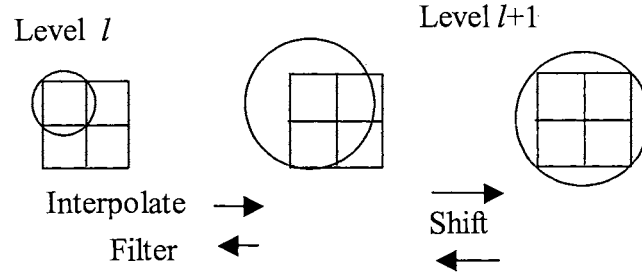


Fig. 4.11: The interpolation and shifting step for moving up tree, and the inverse shifting and filtering step for moving down tree.

In practice, (4.41) is not explicitly evaluated. Instead, interpolation in the ϕ coordinate is achieved using fast Fourier transforms (FFTs). The θ interpolation requires a discrete Legendre transform. A fast algorithm does not exist for the Legendre transform, so interpolation coefficients are found initially and stored. The procedure is explained in detail in [64]. Note that (4.39) is explicitly evaluated at the lowest (finest) level.

2) Dis-aggregation Step

At the highest level, the plane wave expansion of a group is translated to an observation group using

$$\mathbf{g}_{m_{L_g}}(\hat{k}_{L_g}) = \sum_{m^l \in D_{m_{L_g}}} T(m, m^l, \hat{k}_{L_g}) \mathbf{s}_{m^l}(\hat{k}_{L_g}) \quad (4.42)$$

The $\mathbf{g}_{m_{L_g}}(\hat{k}_{L_g})$ then must be dis-aggregated to the children groups. The process is similar to the aggregation step, although as fewer plane waves result that it is typically

referred to as a filtering rather than an interpolation. Mathematically, the dis-aggregation from level l to level $l-1$ is

$$\mathbf{g}_{m_{l-1}}(\hat{k}_{l-1}) = \sum_{m'_l \in D_{m_l}} e^{-j\mathbf{k} \cdot (\mathbf{r}_{cm'_{l-1}} - \mathbf{r}_{cm'_l})} \sum_{1 \text{ to } K_l} \mathbf{W}_{l,l-1} \left(\mathbf{g}_{m'_l}(\hat{k}_l) \right). \quad (4.43)$$

for $l = L_g, \dots, 3, 2$

$\mathbf{W}_{l,l-1}$ are filtering coefficients from level l to level $l-1$. D_{m_l} denotes all groups far from group m at level $l-1$ but not far at the parent level (level l). This again includes a shifting as well as a filtering. It can be illustrated in Fig. 4.11, (from right side to the left). The filtering is also implemented using an FFT in the ϕ direction and a Legendre transform in the θ dimension.

At the finest level (level 1), the final expression for MLFMA can be rewritten as

$$V_{m\alpha} = \sum_{m' \in B_m} Z_{m\alpha m'\alpha'} I_{m'\alpha'} + \frac{\omega\mu k}{(4\pi)^2} \int d^2 \hat{k} \left\{ \mathbf{V}_{\text{fm}\alpha}(\hat{k}_{L_1}) \cdot \mathbf{g}_{L_1}(\hat{k}_{L_1}) \right\}. \quad (4.44)$$

MLFMA is a $O(N \log N)$ method, as outlined in [69]. As mentioned, FMM is $O(N^{3/2})$. For small N , the overhead of MLFMA (interpolation, filtering) can lead to a less efficient algorithm than FMM, but with large N , MLFMA has a significant advantage.

4.4.2 Test Cases for MLFMA

Fig. 4.12 shows the results of applying MLFMA to a perfectly conducting sphere of radius 0.5λ . The segmentation in both θ and ϕ directions was 40, so there are 3120 triangular patches. Only the first 160 current values are displayed here. $D = 2$ was used

at all levels. The solid line shows the results when only one level was used (FMM), while the starred line shows two levels. Excellent agreement is achieved.

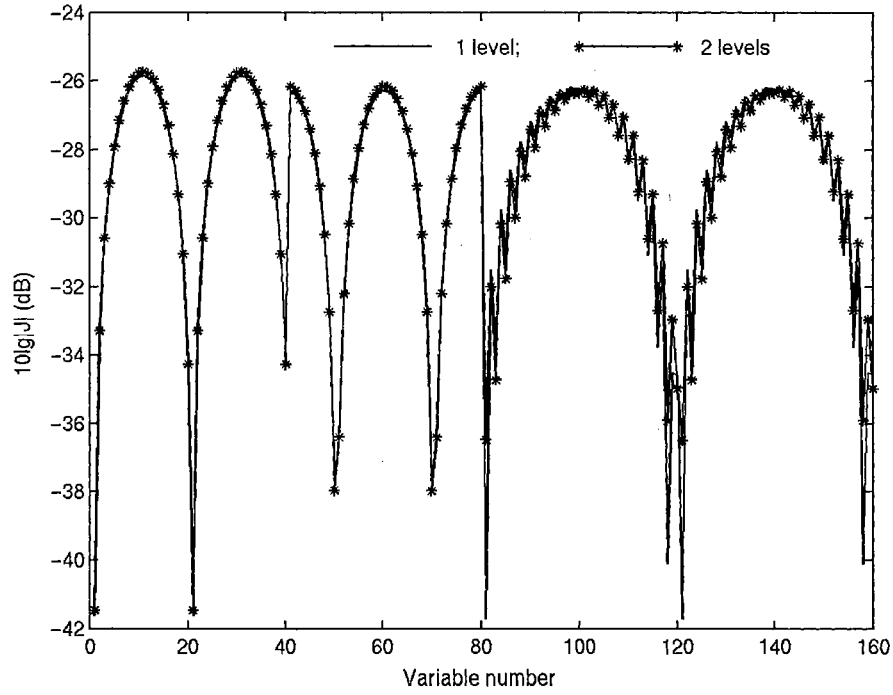


Fig. 4.12: Testing results of PEC sphere by using MLFMA.

As mentioned in Chapter 3, SPM is very accurate at moderate incidence angles with small surface roughness. SPM was therefore used to check the implemented MLFMA. A periodic “cosine” surface was first used. The surface was defined by

$$z(x, y) = A \cos(K_B x), \quad (4.45)$$

where A is an amplitude factor and K_B is a surface wavenumber. A was set to 0.005λ . For this small surface roughness, the contribution of KA is very small when the incidence angle is larger than 30° . The total backscattering can therefore be regarded as only due to SPM. K_B was set to $\sqrt{2}$. Hence, there should be a Bragg-resonant peak at a 45° incidence angle. To avoid edge effects, a Gaussian illumination window was applied in azimuthal direction and a Thorsos window (to be described in detail in Chapter 5) was

used in the range direction [35]. The Thorsos window requires a large modeled range length. The surface used was 32λ in range and 4λ in azimuth, giving 38,040 unknowns to be found. A three level MLFMA was used. The results are shown in Fig. 4.13. A surface impedance of $Z_s \approx 44 + j13\Omega$ for seawater at 10 GHz was used. The starred line and circled line represent VV and HH found using MLFMA, respectively. The solid line and dashed line are for VV and HH found using SPM. The MLFMA results and SPM results agree well around 45° . Away from the peak the MLFMA cross-sections are about -60 dB, showing the numerical noise floor of the technique.

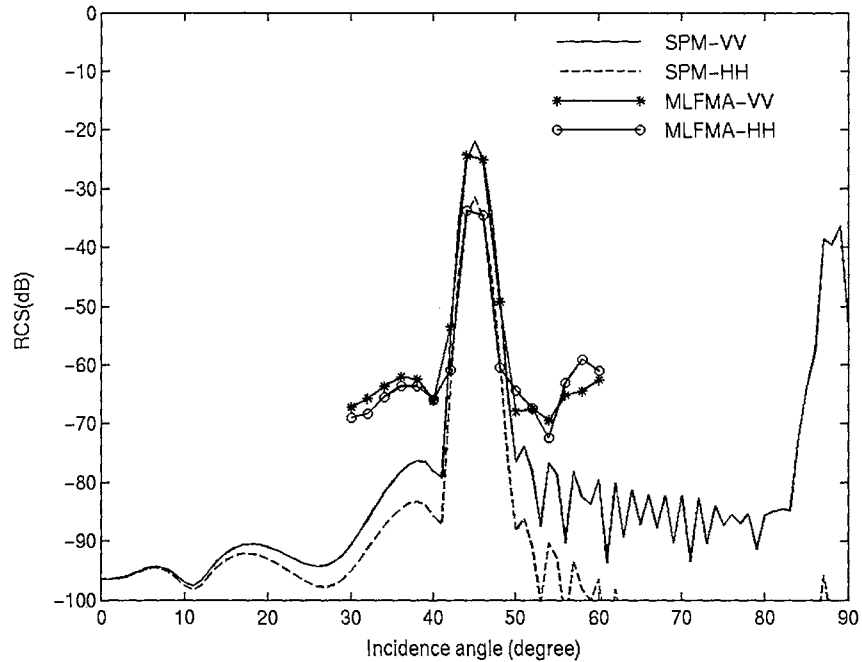


Fig. 4.13: Comparison of SPM and MLFMA for “cosine” surface.

Another test was performed using 3-D rough Pierson-Moskowitz surfaces. The RMS height of the surface was 0.05λ . The surface was 48λ in range and 8λ in azimuth, giving 114,640 unknowns. The same illumination window treatment was used as for the “cosine” surface, and again three MLFMA levels were used. The results using one

surface are shown in Fig. 4.14. The circled line and starred line are for VV and HH found using MLFMA, respectively. The solid line and dashed line are for VV and HH found using SPM. The agreement is within 1.5 dB. Fig. 4.15 was obtained by averaging the scattering from 12 realizations (a 12 sample Monte-Carlo test). The agreement at both polarizations is better than 1dB.

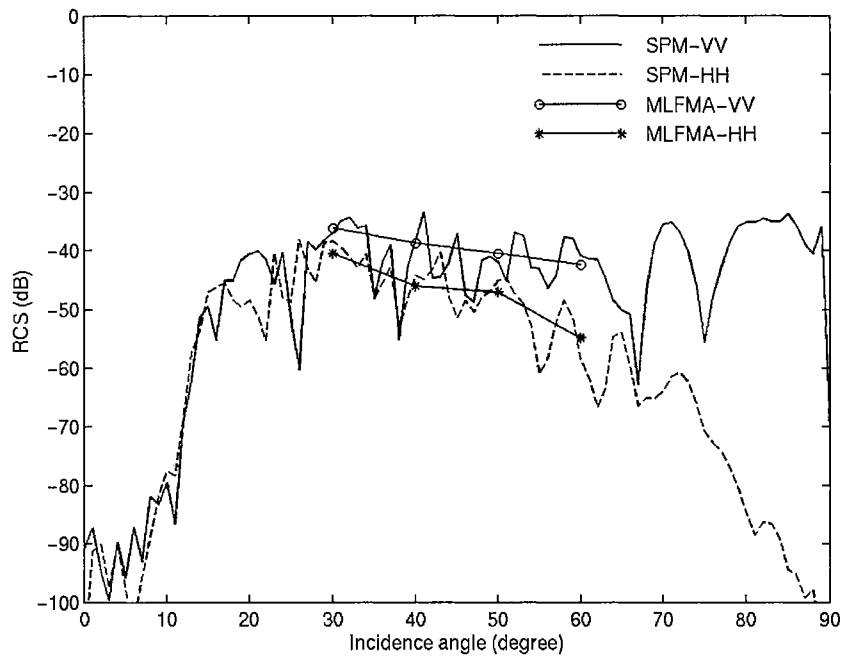


Fig. 4.14: Comparison of SPM and MLFMA for one deterministic 3-D PM surface.

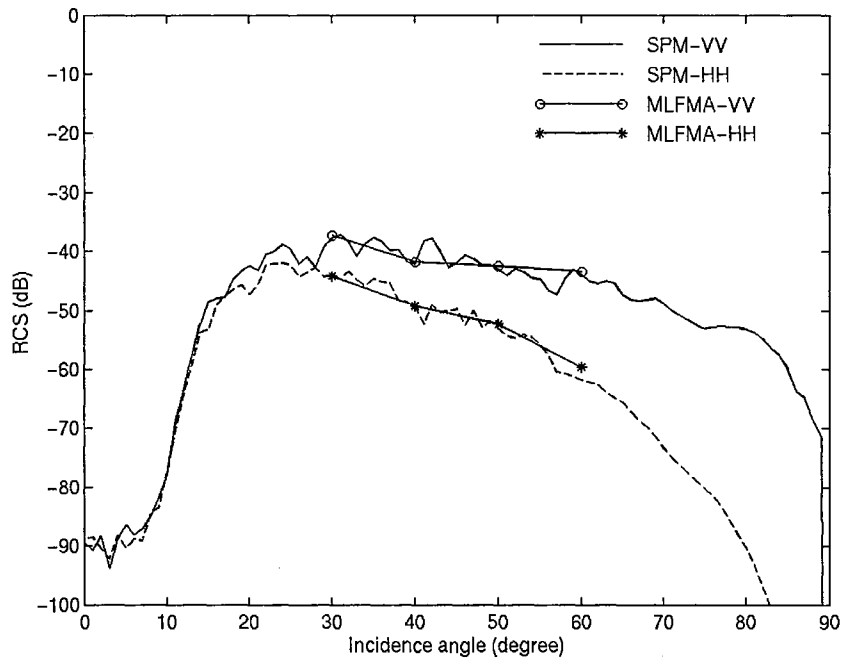


Fig. 4.15: Comparison of Monte-Carlo results of SPM and MLFMA for 3-D PM surfaces.

CHAPTER 5

TWO-DIMENSIONAL EDGE TREATMENT

Fig. 4.3b showed that the current induced on a flat plate tangential to an edge is quite large. This large current is responsible for edge diffraction. With the flat plate this is physically accurate. However, when an arbitrary scattering surface is truncated to fit in finite computer memory, similar edge currents will be induced. This leads to non-physical diffraction that will both directly mask the backscatter from the true surface features, as well as affect the feature scattering through multiple interactions. In this chapter a method to suppress the edge effects is examined.

5.1 Approaches

Several approaches have been used to treat edges in moment method analyses. As discussed in Chapter 2, MM/GTD is a very powerful method to suppress the edge diffraction from 2-D surfaces that does not require substantial extra calculation. Unfortunately, it requires that the diffraction into the GTD region be from a distinct point. It therefore cannot be extended to the 3-D case. Other approaches that can be used in the 3-D case can be classified to two types. One is illumination-weighting windows. In this, the illumination is smoothly reduced to near zero at the edges. Two illumination windows that have been considered include the Gaussian window and the Thorsos

window. These are reviewed below. Another approach is to resistively load the edge, which also forces the current to zero. West [76,77] examined resistive edge loading in the 2-D case, and compared the performances of this two different resistive tapers. Here the use of resistive loading for control of edge effects is extended to the 3-D case.

5.1.1 Illumination Windows

1) Gaussian window

The simplest illumination window is the Gaussian window. When applied in the azimuthal (y) dimension, it is written as

$$p(y) = \exp\left(\frac{-(y-y_0)^2}{g_0^2}\right), \quad (5.1)$$

where y_0 is the center of the beam in the azimuthal direction and g_0 is a constant that controls the width of the illumination beam. This window has proven adequate for weighting in the azimuthal direction.

2) Thorsos window

The Thorsos window was introduced for weighting in the range direction [35]. It has the advantage of providing a more exact solution to the wave equation than the simpler Gaussian window at non-zero incidence angles. This window can be written as

$$p(\mathbf{r}) = \exp\left\{j\mathbf{k} \cdot \mathbf{r} [1 + w(\mathbf{r})] - (x - z \tan \theta)^2 / g_0^2\right\}, \quad (5.2)$$

where $w(\mathbf{r}) = [2(x - z \tan \theta)^2 / g_0^2 - 1] / (kg \cos \theta)^2$ and θ is the incidence angle. Note that

the Thorsos window includes the phase of the incident wave, so the phase of E^i in (4.4)

should be compensated. Also, $\mathbf{k} = \hat{a}_x k_x + \hat{a}_z k_z$, so there is no phase variation in y

direction.

Because the weighting affects only the incoming illumination, only equation (4.10b) need be modified for implementation. The Gaussian window affects only the amplitude of V_m . V_m using a Gaussian window is written as

$$V_m = l_m \left(p(\mathbf{r}_m^{c+}) \mathbf{E}_{mn}^+ \bullet \frac{\boldsymbol{\rho}_m^{c+}}{2} + p(\mathbf{r}_m^{c-}) \mathbf{E}_{mn}^- \bullet \frac{\boldsymbol{\rho}_m^{c-}}{2} \right). \quad (5.3)$$

The phase of V_m is also affected when the Thorsos window is used.

The Thorsos window has proven quite popular. However, as the illumination grazing angle decreases, the length of the modeled surface must be increased to give a realistic representation of the illumination of surface features. Therefore, this approach becomes quite expensive at low grazing angle (LGA), particularly for 3-D surfaces.

5.1.2 Resistive Loading of Edges

Oh and Sarabandi [75] considered the use of resistive loading of edges to suppress unwanted diffraction from surface truncation points in rough surface scattering. It has the advantage of very low computational overhead, so it appears to be a promising approach for treating scattering from arbitrary 3-D surfaces. West [76,77] compared the performance of a resistive loading based on Taylor weighting first introduced by Haupt and Liepa [74] with that of the power-law weighting used by Oh and Sarabandi [75]. The Taylor weighting proved superior, so it is used hereafter for the 3-D surfaces.

Taylor taper window [74]

The resistive loading $R(\mathbf{r})$ for the Taylor taper takes the form

$$R(\mathbf{r}) = \begin{cases} \frac{1}{J(\mathbf{r})} - \frac{1}{2} & \text{loading area} \\ 0 & \text{otherwise} \end{cases}, \quad (5.4)$$

where

$$J(\mathbf{r}) = \frac{1}{2a} \left[1 + 2 \sum_{n=1}^{\bar{n}-1} f(n) \cos\left(\frac{\pi n |\mathbf{r} - \mathbf{r}_0|}{a}\right) \right], \quad (5.5a)$$

$$f(n) = \frac{[(\bar{n}-1)!]^2}{(\bar{n}-1+n)!(\bar{n}-1-n)!} \prod \left(1 - \frac{n^2}{w_m^2} \right), \quad (5.5b)$$

$$w_m = \begin{cases} -n \sqrt{\frac{A^2 + (m-0.5)^2}{A^2 + (\bar{n}-0.5)^2}}, & |n| < \bar{n} \\ n, & |n| \geq \bar{n} \end{cases}, \quad (5.5c)$$

\bar{n} is the number of sidelobes desired in the scattering pattern at a level of q dB below the main reflection,

$$A = \frac{1}{\pi} \cosh^{-1}(10^{q/20}), \quad (5.5d)$$

a is the distance over which the loading is applied, and \mathbf{r}_0 is the position where the loading begins.

The EFIE with resistive loading added is written as [75]

$$\begin{aligned} \mathbf{E}_{\tan}^i = & \left[\frac{\mu}{4\pi} \int_S \mathbf{J} \frac{e^{-jkR}}{R} dS' + \frac{1}{4\pi\epsilon} \int_S \sigma \frac{e^{-jkR}}{R} dS' \right]_{\tan} \\ & + \left[\frac{1}{2} (Z_s + 2R(\mathbf{r})) \mathbf{J} + \frac{1}{4\pi} \int_S Z_s \left(\hat{\mathbf{n}} \times \mathbf{J} \right) \times \nabla \left(\frac{e^{-jkR}}{R} \right) dS' \right]_{\tan}. \end{aligned} \quad (5.6)$$

The resistive loading can therefore be added to the RWG moment method by replacing (4.16a) with

$$\left\langle \frac{1}{2} (Z_s + 2\eta) \mathbf{J}, \mathbf{f}_m \right\rangle = \frac{1}{2} \sum_{n=1}^N I_n \left\{ \int_{r_m^+} (Z_s + 2R(\mathbf{r}_m^{c+})) [\mathbf{f}_n \cdot \mathbf{f}_m] dS + \int_{r_m^-} (Z_s + 2R(\mathbf{r}_m^{c-})) [\mathbf{f}_n \cdot \mathbf{f}_m] dS \right\}. \quad (5.7)$$

The resistive loading affects only the diagonal element of the interaction matrix. The overhead calculation of $R(\mathbf{r})$ is trivial, so the cost of adding the resistive taper is negligible. West [77] showed that although resistive tapering was introduced assuming perfectly conducting surfaces, it is also effective in controlling the edges with 2-D finite conductivity seawater surfaces.

5.2 Preconditioning [70]

Adding the resistive loading changes the relative levels of the diagonals, reducing the conditioning of the interaction matrix and giving much slower iteration convergence. Point Jacobi preconditioning, where the rows are normalized to give unity diagonals, has therefore been used. More sophisticated preconditioning based on an incomplete LU factorization of the FMM sparse matrix will be considered in later work.

5.3 Test Cases

5.3.1 Surface Setup

The resistive-loading edge treatment was tested by considering the scattering from a 3-D surface derived from a profile taken from the LONGTANK series representing the time evolution of a plunging-breaker water wave [80]. The complete time history of the crest of the generated wave is shown in Fig. 5.1a. Fig. 5.1b shows profile 9 and 13 after the crest areas were isolated and the profiles extended with smoothly curved sections of surface (radius= 10λ) that join to planar sections of surfaces that are angled at 30° down from horizontal. The extensions, shown as the dashed line in the figure, are needed to allow a comparison of the calculated scattering with reference 2-D MM/GTD results as

described in Chapter 2. Profile 13 has a more developed jet than profile 9. These are the same as the “isolated-crest” surfaces used in West and Zhao [83]. The 3-D profile used for the initial tests was formed by extending the 2-D profile uniformly 4λ in the azimuthal direction. Fig. 5.1.c shows the 3-D surface formed from profile 9.

Two different edge-treatment approaches were used in the tests. In the first, the resistive loading was applied to the forward and trailing edges of the surface, while Gaussian illumination weighting was applied in the azimuthal (y) direction. In the second, resistive loading was applied to all edges.

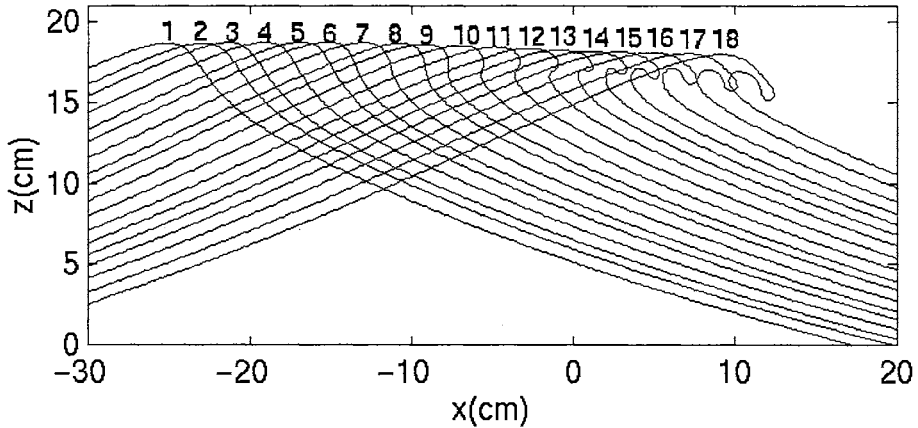


Fig. 5.1a: LONGTANK profiles.

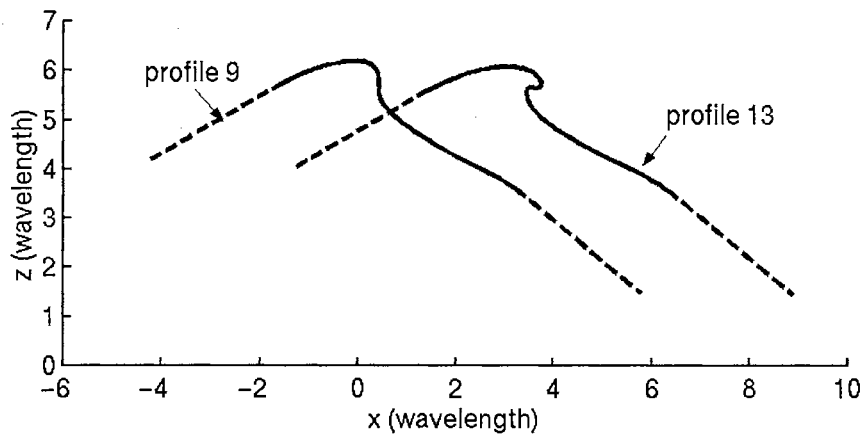


Fig. 5.1b: Profile 9 and 13 with extension in range.

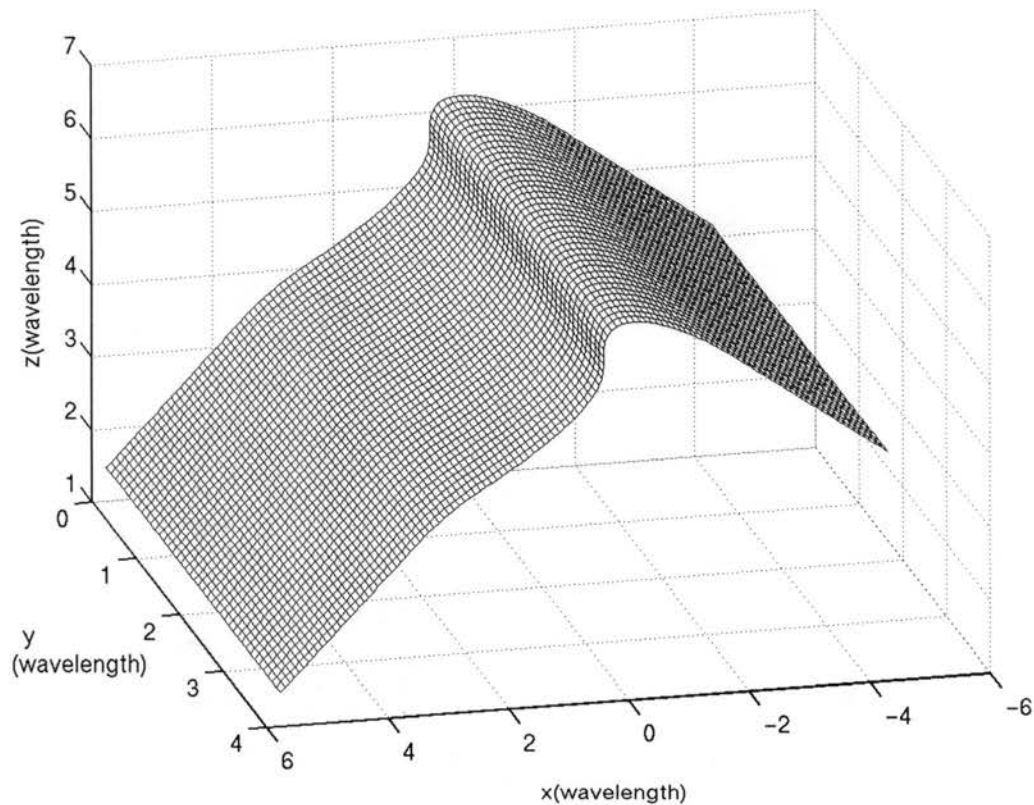


Fig. 5.1.c: 3-D profile with 4λ extension in azimuth from profile 9.

5.3.2 Gaussian Illumination Plus Resistive Loading

In the first test case, a Gaussian illumination window was used in the azimuthal direction to remove the edge diffraction, while resistive loading was used in range extension area, as shown in Fig. 5.2. The resistive loading was applied over 3λ on each end of the surface. In order to demonstrate the effectiveness of this technique, the results were compared with that of MM/GTD in the 2-D profile. The reference 2-D scattering of MM/GTD calculations were found using pulse basis functions of 0.025λ in length, minimizing any possible error in the reference scattering.

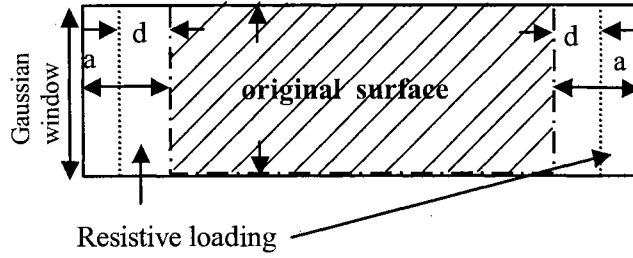


Fig. 5.2: Resistive loading in azimuth for 3-D surface.

Because the wave profile was extended in azimuth to give a 3-D scattering surface, the 2-D cross-sections (σ_{2-D}) yielded by the MM/GTD approach must be converted to 3-D cross-sections (σ_{3-D}) using [1, p578]

$$\sigma_{3-D} \approx \sigma_{2-D} \frac{2l_{equ}^2}{\lambda}, \quad (5.8)$$

where l_{equ} is the equivalent length in azimuth direction. It can be calculated by using

$$l_{equ} = \int_0^{L_y} \left[\exp\left(\frac{-(y - L_y/2)^2}{g_0^2}\right) \right]^2 dy, \quad (5.9)$$

where L_y is the width of the surface in the azimuthal direction. $g_0 = \frac{\sqrt{2}}{2} L_y$ was used in this test, where $L_y = 4\lambda$ is the azimuthal width of the surface, giving an equivalent width 1.2532λ .

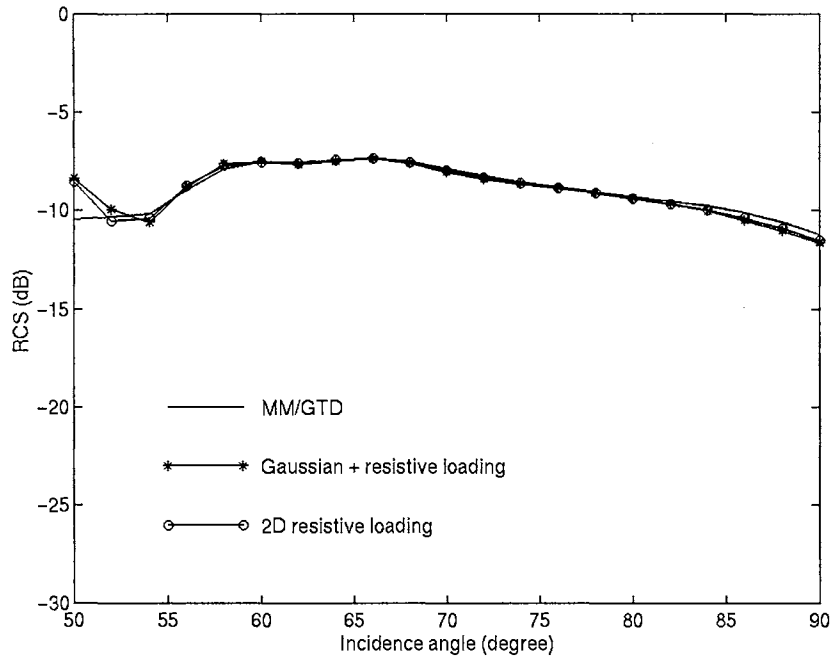
Fig. 5.3 and 5.4 are the backscattering from profile 9 when the surface is assumed both to be perfectly conducting and to have a surface impedance of $Z_s = 44 + j13\Omega$ (corresponding to seawater at 10 GHz [2]). Fig. 5.5 and 5.6 are the corresponding results using profile 13. The solid lines show the reference 2-D MM/GTD results, and the starred lines show the 3-D results with resistive loading applied to the range edges. Very good agreement is achieved at both polarizations above 55° incidence. For profile 9, the

maximum error is only 0.3 dB for both the PEC and seawater surfaces. With profile 13, the performance is a bit poorer, primarily due to the deep null in the VV case at 82° incidence. With the perfectly conducting surface, the maximum error for HH is less than 0.5 dB, and is smaller for seawater. This is because that the edge diffraction is naturally smaller with finite conductivity. At vertical polarization the agreement is within 1dB at most points, although it approaches 3 dB in the profile 13 null due to numerical noise. This point will contribute little to the total backscattered power, so is not of great concern.

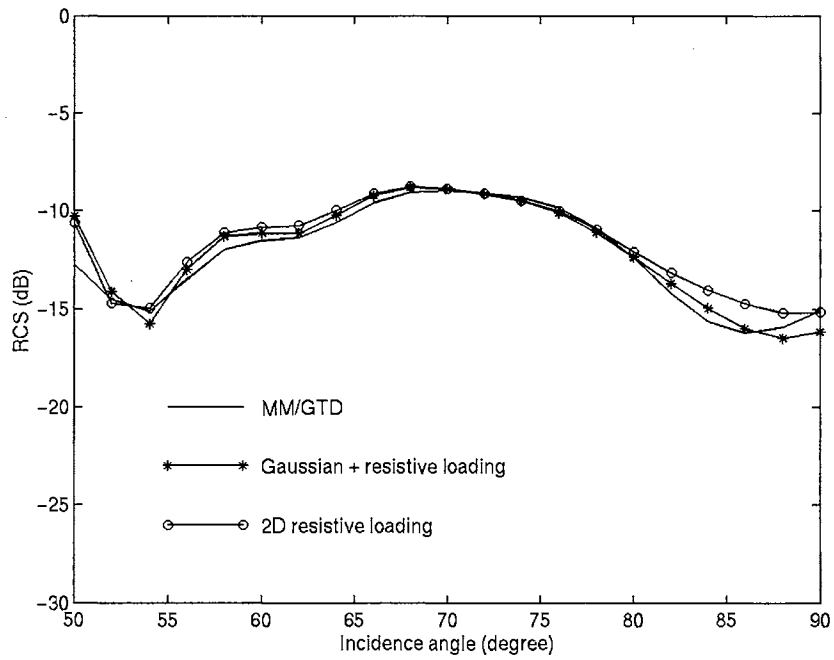
Below 55° incidence, the local angle of incidence on the planar extension of the front face of the surface is less than 25° . Sidelobes from the resistive loading therefore affect the accuracy. The same inaccuracy is observed when the edges of the 2-D surface are resistively loaded [76]. This is further discussed in Section 6.3.1. As we are interested in LGA (high incidence) backscattering, the inaccuracy at moderate and low incidence is of little concern.

5.3.3 2D Resistive Taper Window

The second test case considered is both the range and azimuthal edges treated with resistive loading as shown in Fig. 5.7. This approach has the advantage of allowing uniform plane-wave illumination of the surface in both dimensions, which is realistic of the open sea case. The dimension a shows the distance over which the taper was applied (3λ in this case). The tapering was added to the corners such that the dotted line shown has same resistance everywhere. The extension in the azimuthal direction is the same as in Fig. 5.1c, but the azimuthal width was increased to 9λ to allow the extra width need for the loading.

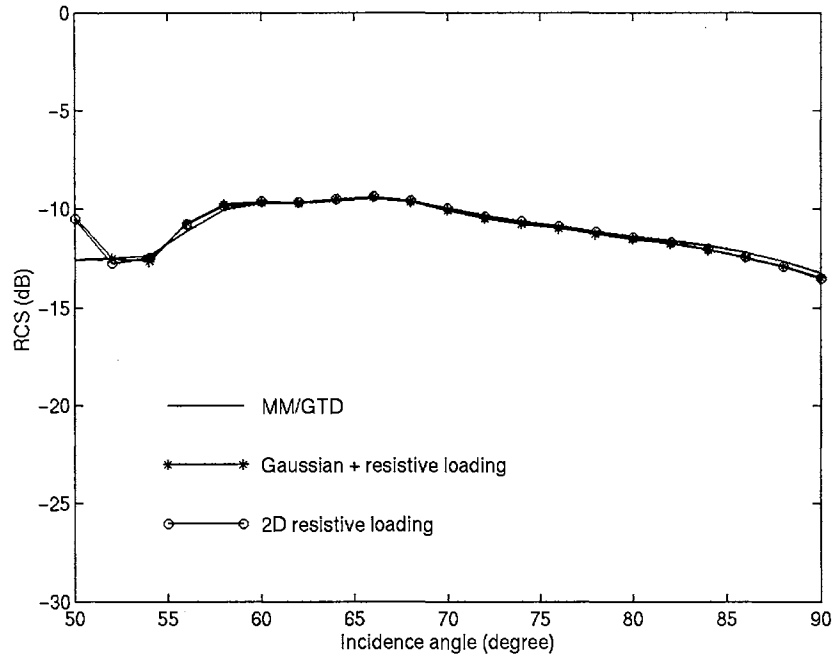


a) HH

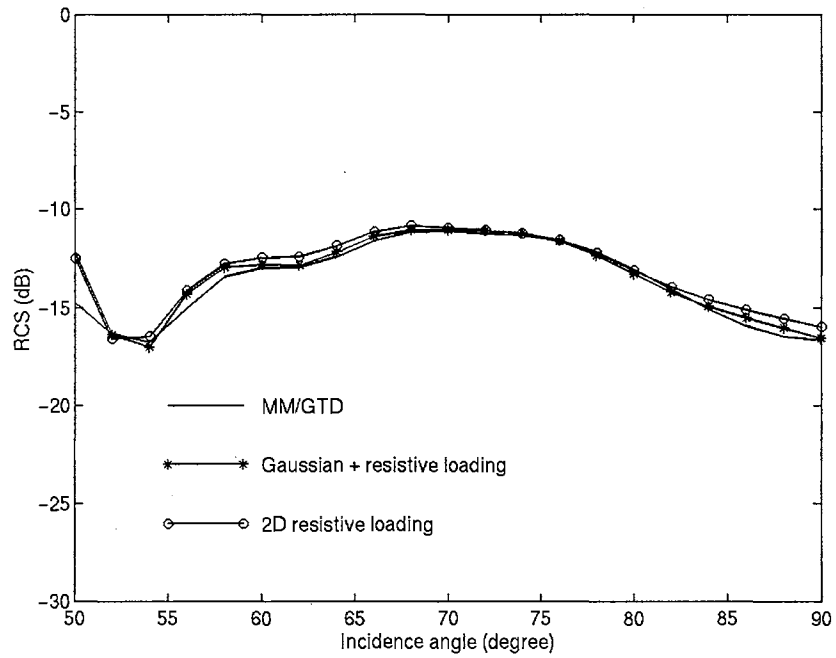


b) VV

Fig. 5.3: Backscattering of profile 9 (PEC, 10 GHz).

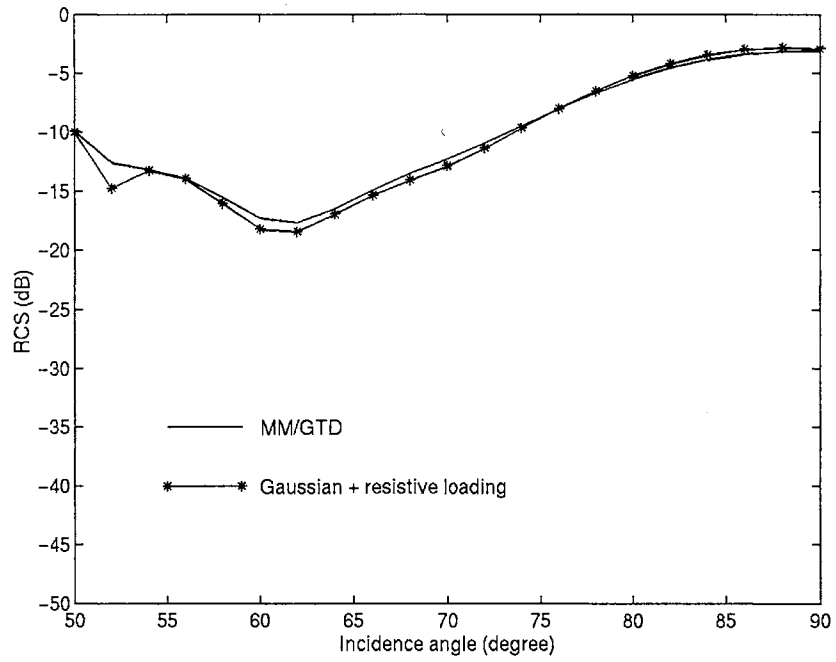


a) HH

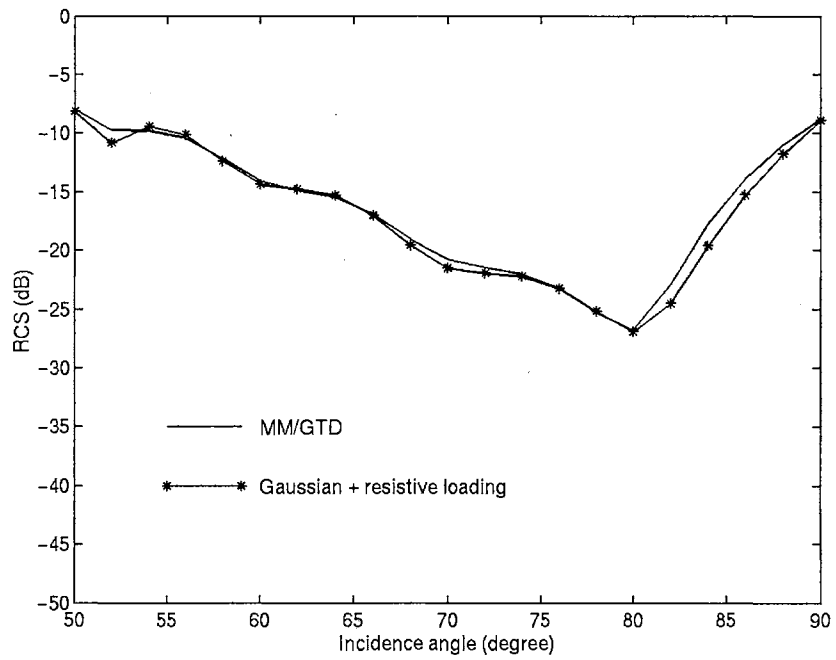


b) VV

Fig. 5.4: Backscattering of profile 9 with impedance (SEA, 10 GHz).

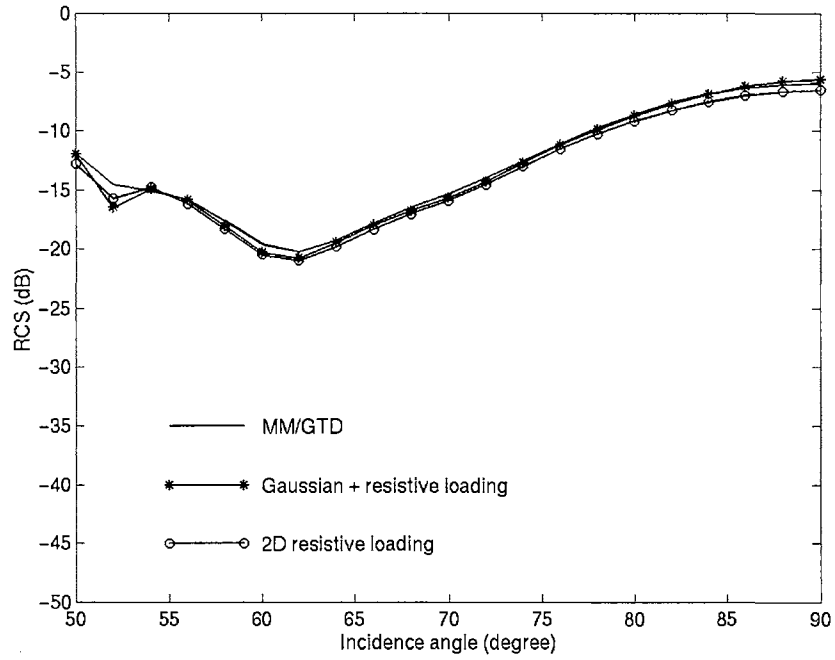


a) HH

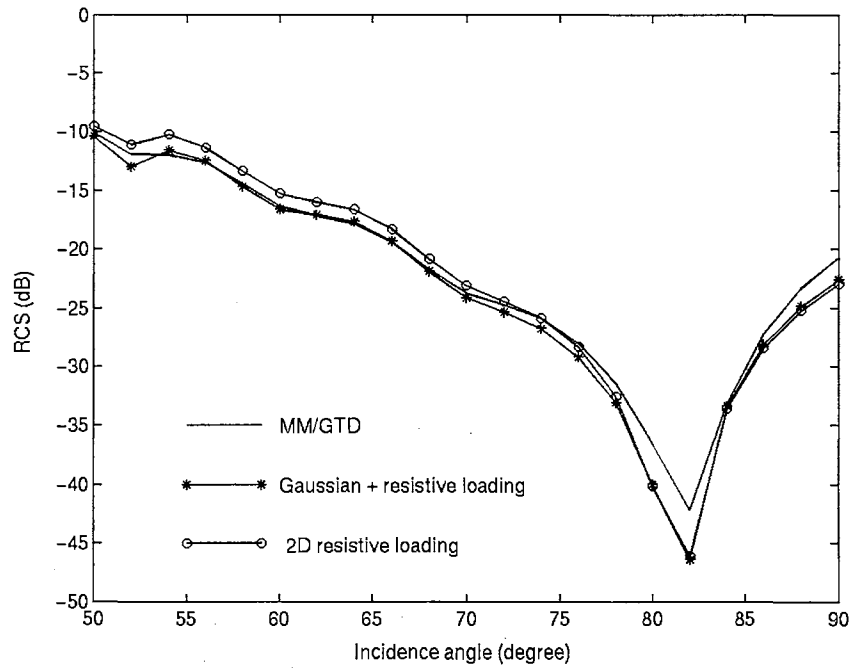


b) VV

Fig. 5.5: Backscattering of profile 13 (PEC, 10 GHz).



a) HH



b) VV

Fig. 5.6: Backscattering of profile 13 with impedance (SEA, 10 GHz).

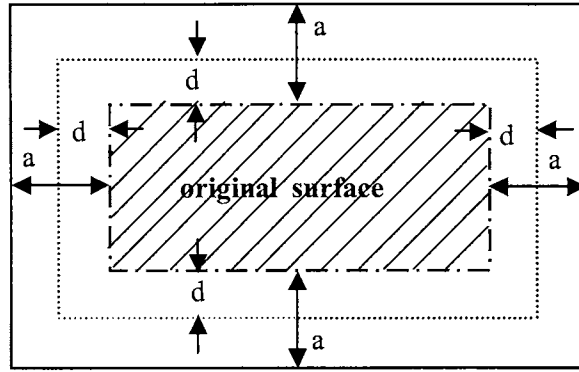


Fig. 5.7: Two-dimensional resistive loading.

An equivalent scattering azimuthal width must be found to allow comparison with the 2-D reference. According to [74], the reflection coefficient ρ from specular reflection points can be written as

$$\rho(r) = \frac{-1}{1 + 2R(r)}. \quad (5.10)$$

where $R(r)$ was given in (5.4). The dominant scattering mechanism from the test surfaces is specular-like reflection from the jet, which will add coherently. The effective width is therefore

$$L_{equ} = \int_{L_y} |\rho| dy. \quad (5.11)$$

For $L_y = 9\lambda$, with 3λ loading at both sides, the equivalent width that will be used in the conversion from 2-D to 3-D is about 5.4λ .

The results using both range and azimuthal loading are also shown in Figs. 5.3, 5.4 and 5.6 as the circle lines. Above 55° the agreement with the reference 2-D results is slightly poorer than when azimuthal illumination weighting was used. However, the agreement is still within 1 dB for seawater conductivity at both polarizations everywhere but in the profile 13 VV null. The performance of the resistive loading is therefore acceptable for this approach.

CHAPTER 6

SPILLING BREAKER SCATTERING

In this chapter the MLFMA numerical routine is used to examine the backscattering from a spilling-breaker. Because 3-D measured surfaces are not available, model 3-D breaker crests were synthesized from the measured 2-D time series shown in Figs. 1.1 and 1.3. The resulting 3-D surfaces are not likely to be entirely realistic, but give test cases for the models. The results are then related to the 2-D scattering results previously published by Ja et al [43,44] and West and Ja [17], and compared to the predictions of analytical scattering models. The spilling breaker is examined here, while the plunging breaker is considered in Chapter 7.

6.1 Scattering Surface

The 3-D spilling breaker profile was constructed from the measured 2-D profiles shown in Fig. 1.1. The 3-D profile was formed by aligning the individual profiles in the azimuth dimension at a spacing of 3 mm (corresponding to 0.1λ for 10 GHz). The resulting surface is shown in Fig 6.1. The final geometry of the wave was influenced by several characteristics of the MLFMA approach and the individual 2-D wave profiles themselves, as now discussed.

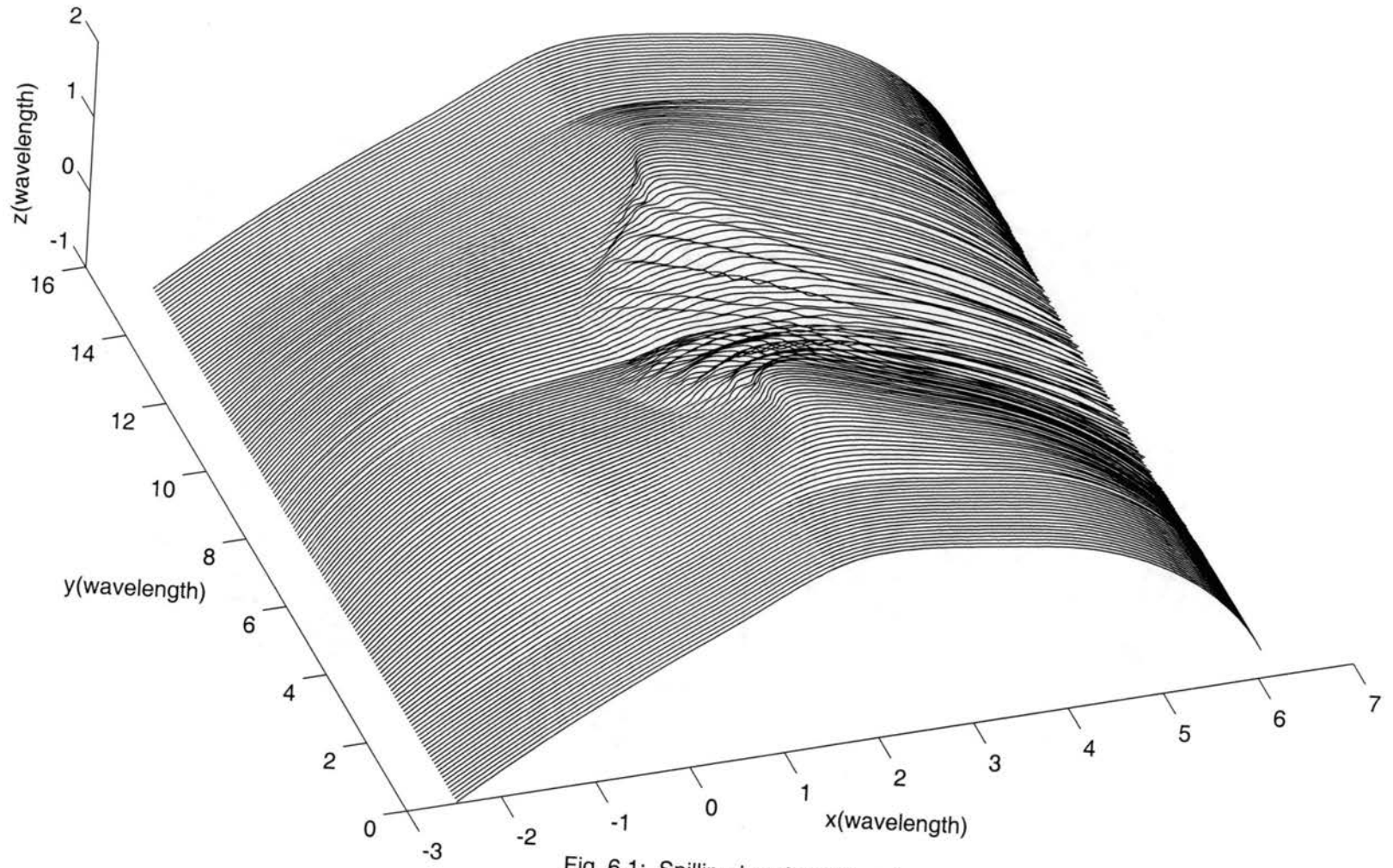


Fig. 6.1: Spilling-breaker full surface.

The MLFMA approach used relies upon resistive loading of the edges to suppress unwanted edge effects. Ideally, the backscattering from the resistively loaded areas would be zero. This eliminates the need for the inclusion of an effective width to adjust the calculated scattering cross section, which may not be easily determined with arbitrary, distributed surface roughness. (An effective width could be found for the test cases in Chapter 5, but these gave specular reflection that could be easily treated using the reflection coefficient). The scattering from the individual 2-D profiles was shown in Fig. 2.5. The scattering from the first profile, when the crest is still round, was quite small compared to the scattering at later times. This profile was therefore extended over 2λ on the edge. The resistive loading was applied over this width, and the total backscatter from this region is therefore assumed to be zero.

The last profile in the 2-D sequence, number 329, has significant roughness, which leads to significant backscattering relative to the other profiles. It is obviously not appropriate to extend this profile azimuthally and apply the loading, as it would dramatically affect the total scattering. Instead, the 3-D surface has been reflected on profile 329, giving a symmetric surface. Resistive loading is therefore also applied on the mirror image of the 2λ extension of profile 0, suppressing the edge effects without affecting the scattering.

The final required modification to the profiles was the extension of the leading and trailing edges for the application of the range-dimension resistive loading. The extensions were formed in the same manner as they were for application of the MM/GTD technique. This shadows the resistive loading from the actual surface roughness, avoiding any unrealistic multipath. Because the start points of the profiles vary, the radius of the

curved sections have been adjusted for each profile to give the same x and z coordinates at the start points. The curved sections joining the actual surface to the planar extensions have a large radius of curvature. The resistive taper is applied over the ends of these extension areas.

6.2 Calculated Scattering

The scattering at 10 GHz was once again considered. The surface impedance used in the impedance boundary condition was therefore $Z_s = 44 + j13\Omega$, that of seawater. All MLFMA calculations were performed with a 0.05λ surface sampling in the range direction and 0.07λ sampling in the azimuthal direction.

Fig. 6.2 shows the backscattering from the complete spilling breaker surface. VV backscattering is shown by the solid line and HH is shown by the dashed line. Cross-polarized backscattering is shown by the circled line for HV (where the transmitted energy is horizontally polarized and the received energy is vertically polarized) and by the starred line for VH (where the transmitted energy is vertically polarized and the received energy is horizontally polarized). Overall the co-polarized backscattering is consistent with that expected from the wave geometry and the associated 2-D results. At 60° there is quasi-specular reflection from the steepest sections of the breaking crest, giving an HH-to-VV backscattering ratio of approximately 0 dB. At higher incidence there are no specular points. The VV backscatter therefore becomes considerably stronger than the HH breaker at higher incidence angle. Near grazing incidence (90°), VV is about 10 dB larger than HH.

The cross-polarized backscatter is well below the co-polarized signal at all angles. From 60° to 70° incidence, the cross-polarization is 40 to 50 dB less than the co-polarization. As the incidence angle increases, the difference between the cross-polarization and co-polarization decreases, giving about a 25 dB to 35 dB difference when the incidence tends to grazing. Note that VH and HV monostatic backscattering should be identical, while there are some differences in the actual results. They agree to within 3-4 dB from 70° to 90° incidence, but lose agreement from 60° to 70° . This results because the scattering cross sections are quite low (40 to 50 below the co-polarizations), and therefore are affected by numerical error due to the finite sampling of the surface. Better agreement can be obtained by using a smaller segmentation, although at the expense of computational efficiency.

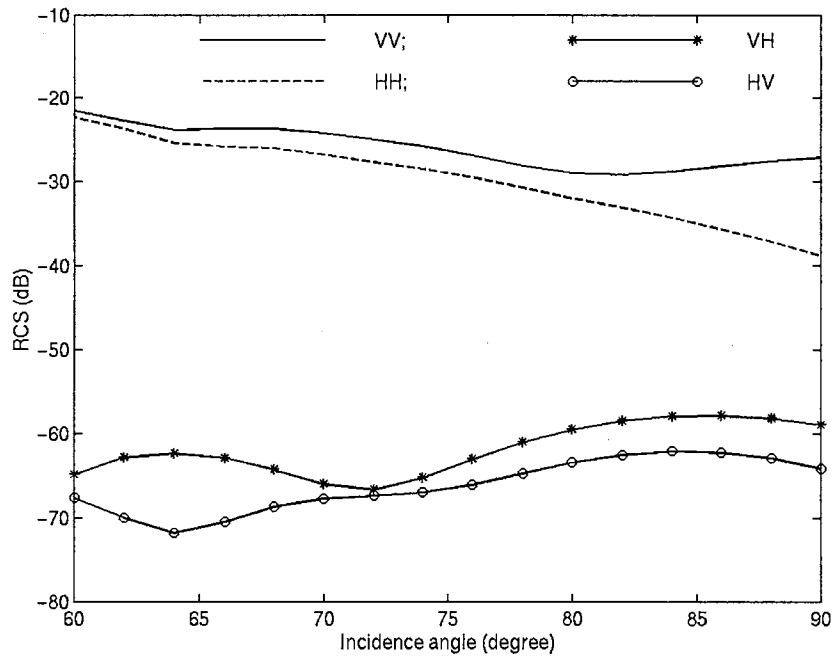


Fig. 6.2: Backscattering from complete spilling breaker using MLFMA.

6.3 Analysis of Scattering

6.3.1 2-D Synthesis of 3-D Results

As mentioned in Chapter 2, the MM/GTD technique has previously been used to model the scattering from the individual 2-D profiles of the spilling breaker by Ja et al [43,44] and West et al [45]. In this, the surface was assumed to be uniform in the azimuthal direction. Scattering cross sections that can be directly compared to the scattering from the 3-D profiles are now synthesized from the 2-D scattering. This was accomplished by coherently adding the scattered 2-D fields using

$$E_{2D\text{-total}} = \sum E_i, \quad (6.1)$$

where E_i is the 2-D scattering of i th 2-D profile. The total 2-D field was then converted to a 3-D field by using equation (11-22d) of Balanis [1, p578]:

$$E_{3D} \approx \left(E_{2D\text{-total}} \frac{l e^{j\pi/4}}{\sqrt{\lambda \rho}} \right)_{\rho=r}, \quad (6.2)$$

where l is the azimuthal width of each 2-D profile used in forming the 3-D crest. ($l \approx 0.017\lambda$ at 10GHz here). The 3-D radar cross-section is then formed using the coherently summed field of (6.2).

Fig. 6.3 shows the comparison of the 3-D cross-sections synthesized from the 2-D results with the reference MLFMA results. The solid and crossed lines are the reference VV and HH MLFMA scattering respectively. The starred and circled lines are the corresponding synthesized VV and HH cross-sections. Very good agreement is achieved at all incidence angles, with a maximum error of 2 dB at 65° . Agreement is within 1.5 dB from 70° to 90° , where there is no effect from the front face loading.

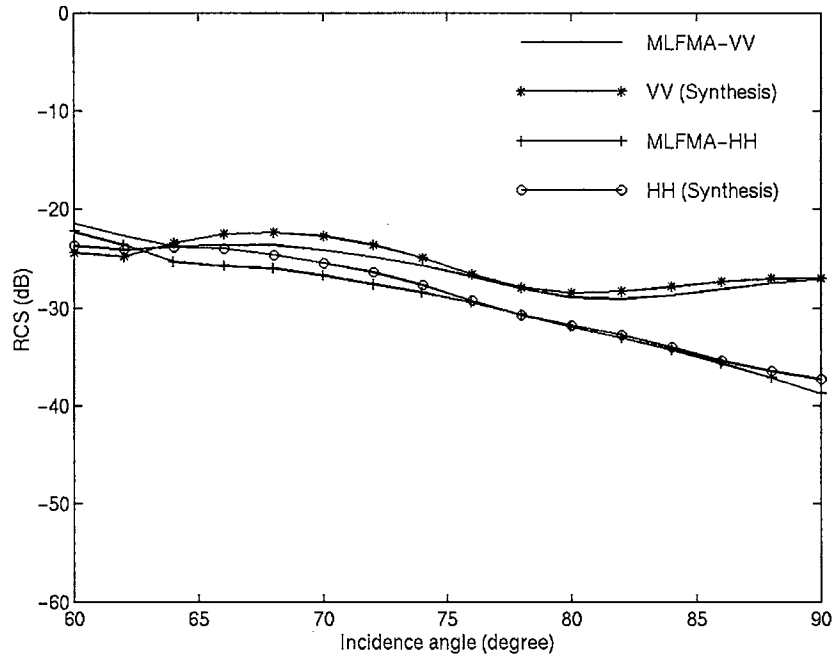


Fig. 6.3: Comparison of 2-D synthesis and 3-D MLFMA results of the full spilling breaker wave.

A) Pre-breaking and post-breaking scattering

The scattering was further analyzed by separating the full surface into pre-breaking and post-breaking sections. The pre-breaking surface, shown in Fig. 6.4, was formed from profiles 0 through 175 using the same method as described in Section 6.1. It is seen from Fig. 2.5 that profile 175 is the initial breaking point of the spilling breaker. Fig. 6.5 shows the backscattering from the pre-breaking surface. The strengths of VV and HH are within 2 dB and 1 dB respectively of those from the full surface at all incidence angles. The returns from the steep section of the full surface before breaking therefore dominate the co-polarized returns. On the other hand, the cross-polarized signals drop by about 10 to 15 dB compared to the full surface at the largest incidence angles. (It is also more strongly affected by numerical error due to the lower cross-sections). The steep section is therefore not the dominant source of cross-polarized scatter.

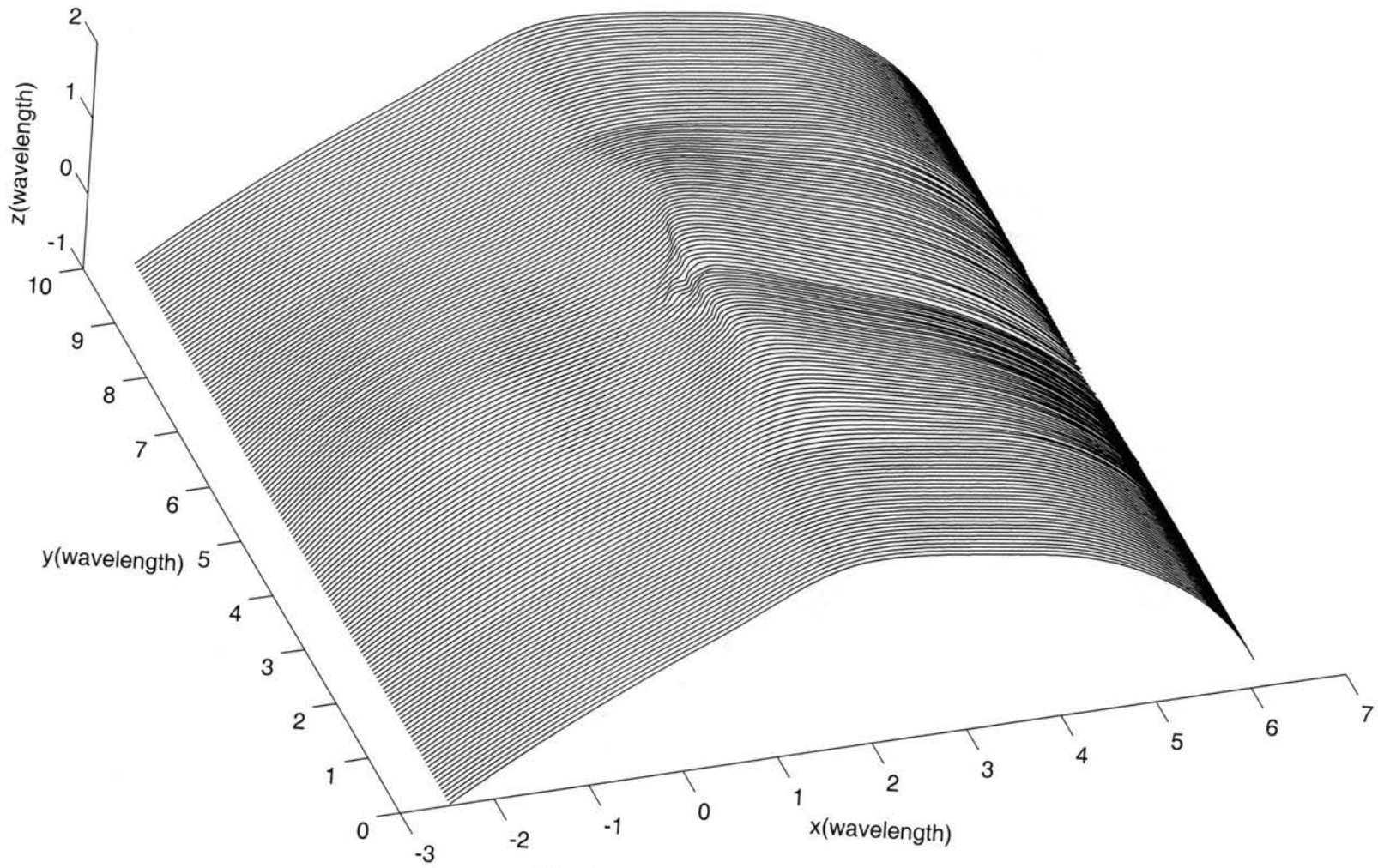


Fig. 6.4: Pre-breaking spiller surface.

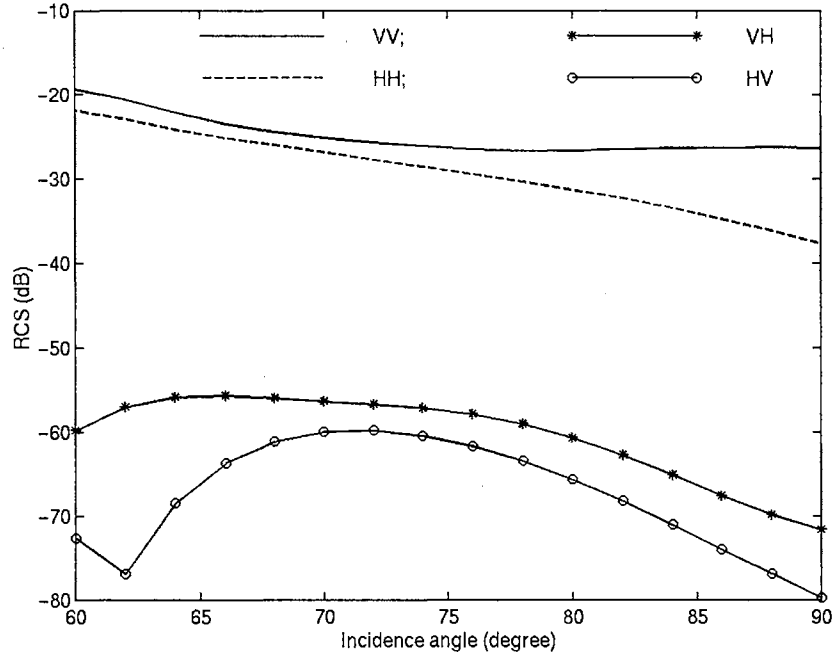


Fig. 6.5: Backscattering from pre-breaking spilling breaker by using MLFMA.

A post-breaking surface, shown in Fig. 6.6, was formed from profiles 175 through 329. Because profile 175 is not entirely smooth, it gives some backscattering through Bragg resonance. (Although the scattering from profile 175 is small in Fig. 2.5, it increases at other incidence angles). It is therefore not appropriate to extend this profile directly for application of the resistive loading. Instead, profile 175 was gradually smoothed over 0.7λ to give a rounded crest with minimal scattering. The smoothed crest was then extended over an additional 2λ , providing the area for the resistive loading.

Fig. 6.7a shows the calculated backscattering from the post-breaking spilling surface. The VV scattering is about 10 dB below that with the complete surface, while the HH scattering is reduced by as much as 15 dB. The HH to VV ratio is consistent with the 2-D results of Fig. 2.5, where it was shown that HH reduces more rapidly than VV after breaking. However, the average VV cross-section was about the same post-breaking as it

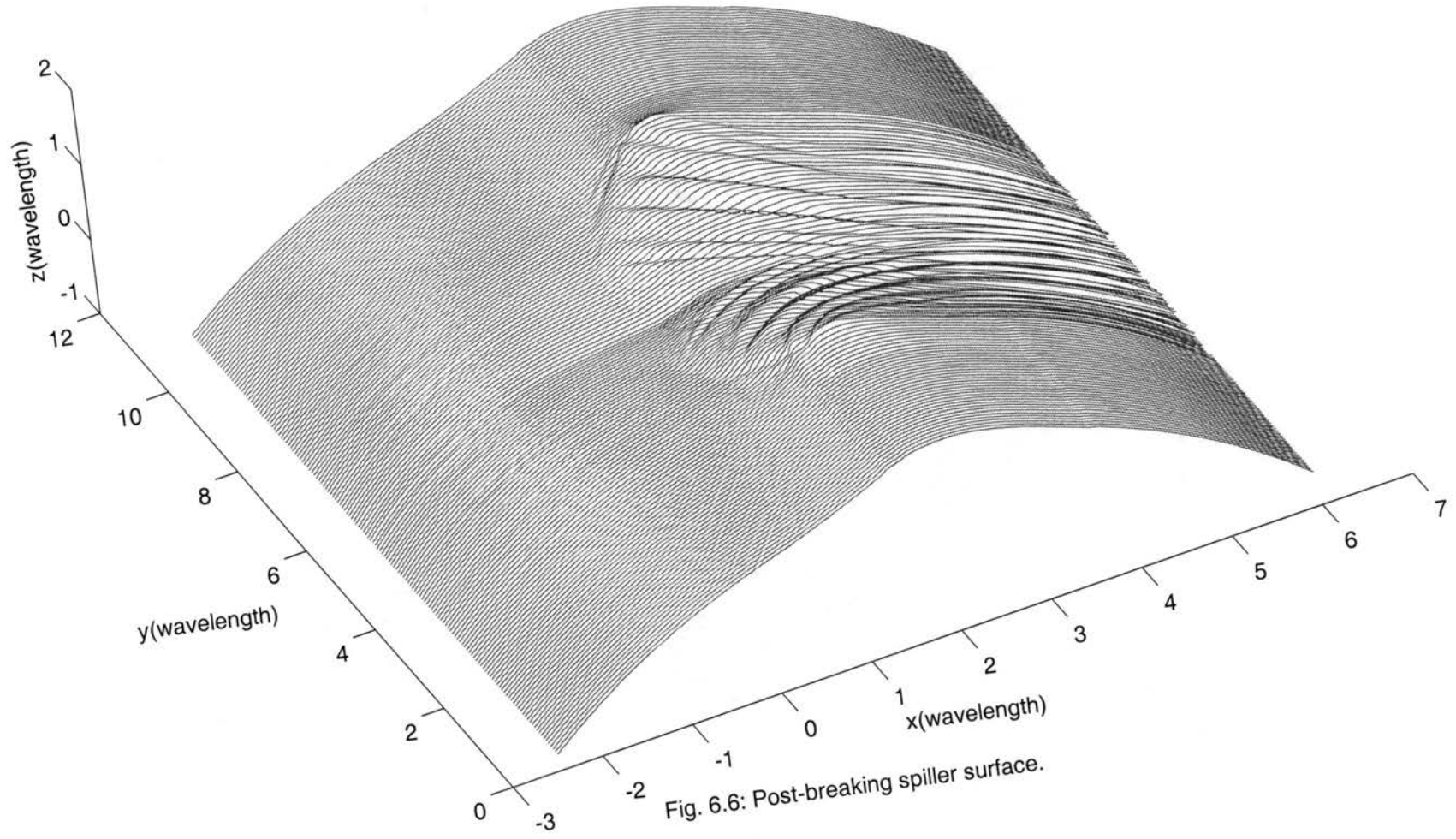


Fig. 6.6: Post-breaking spiller surface.

was in pre-breaking in the 2-D scattering. Here the post-breaking VV cross-section was 10 dB lower than pre-breaking. This is because the post-breaking surface is due to Bragg-like scattering. The 2-D surfaces however are assumed to extend uniformly in the azimuthal direction. This gives an azimuthally coherent scattering surface that leads to strong Bragg scattering with cross-sections comparable to the overturning section. The 3-D surface on the other hand varies randomly in the azimuthal direction. The scattering therefore adds incoherently in the azimuthal direction, giving a weaker cross-section. The pre-breaking surface, however, changes very slowly in azimuth. It therefore gives a coherent reflection that remains strong.

The cross-polarized backscatter of the post-breaking part is approximately the same level as that observed from the complete surface. This is because the surface becomes more random after breaking, introducing multiple scattering that gives cross-polarized components [78].

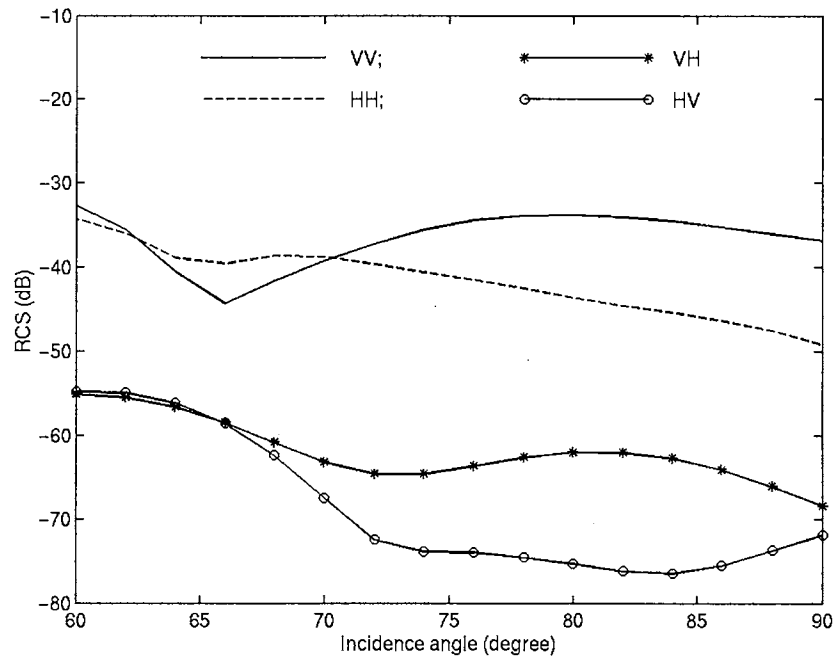


Fig. 6.7a: Backscattering from post-breaking spilling breaker by using MLFMA. (The cross-sections are valid only above 70° incidence)

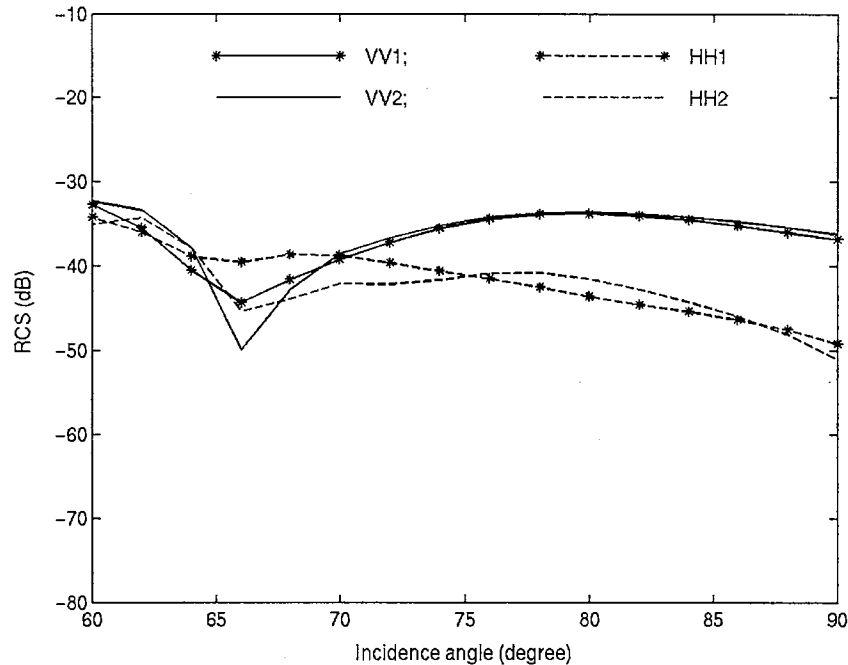


Fig. 6.7b: Comparison of backscattering from post-breaking spilling with different extension angles.

The choice of the surface extension may have some impact on the calculated scattering. As mentioned in Section 5.3.2, there is a mainlobe reflection response from the resistively loaded surface due to the Taylor weighting used. This response can be significant when the local incidence angle on the loading is less than 20° [77]. To give a smooth 3-D surface over the area in which the resistive loading is applied, the individual 2-D profiles were extended to the same point at the front. Because the original start points of the measured profiles are different, the extension angles of individual profiles are necessarily different. Overall the extension angles in the post-breaking region are larger than that in the pre-breaking region. This phenomenon was found in the backscattering in Figs. 5.3 through 5.6. From 50° to 55° incidence, the local angles of incidence on the planar extension of the front face in Figs. 5.3 through 5.6 range from 20° to 25°

(relative to horizontal). The extension angles in Fig. 6.4 and Fig. 6.6 are even larger than that in Figs 5.3 through 5.6. To investigate the effect of the scattering in Fig. 6.2 and Fig. 6.5, the calculations were repeated with the individual profiles extended to different points. In this case, the leading edge point was changed from $(x = -2.5\lambda, z = -1.0\lambda)$ to $(x = -2.2\lambda, z = -1.0\lambda)$, giving even larger angles with respect to horizontal for the extensions. For the pre-breaking surface, the change in extension affected the cross-sections less than 0.5 dB from incidence 60° to 90° . For the complete surface, the change was less than 0.5 dB from incidence 70° to 90° and 1.5 dB from 60° to 70° . Figures 6.2 and 6.5 are therefore reliable at all angles shown. This will be further demonstrated in the next section. Significant changes occur with the post-breaking surface, however. In this case, the leading edge point was moved from $(x = -2.5\lambda, z = -0.8\lambda)$ to $(x = -2.5\lambda, z = -1.0\lambda)$. The results are shown in Fig. 6.7b, VV1 and HH1 indicating the scattering with the original extension and VV2 and HH2 indicating the modified surface. The agreement from 60° to 70° is poor due the mainlobe reflection from the resistive taper. Good agreement was found from 70° to 90° , especially for VV. From these comparisons, it is concluded that the scattering cross-sections in Fig. 6.7a can only be considered accurate above 70° incidence. Only this range will be considered in the scattering from the post-breaking surface hereafter.

It should be noted that the cross-sections of the complete surface and pre-breaking surface are much larger than that of the post-breaking. Moreover, the extension angle in the pre-breaking region is less extreme. Combined, these factors reduce the overall effect of the extension loading to negligible levels.

B) 2-D synthesis of pre-breaking and post-breaking

3-D scattering cross-sections were again synthesized from the 2-D scattering results for the pre- and post-breaking surfaces. The results are shown in Figs. 6.8 and 6.9. The solid and crossed lines are the reference VV and HH MLFMA scattering, respectively, and the starred and circled lines are the corresponding synthesized VV and HH cross-sections. Very good agreement is achieved at all incidence angles with the pre-breaking surface in Fig. 6.8, with a maximum error of 2 dB at 65° . Agreement is within 1.5 dB from 70° to 90° . However, the agreement is very poor with the post-breaking surface in Fig. 6.9.

This differing behavior results due to the differing surface roughness. The 2-D synthesis assumes that the individual profiles extend uniformly to infinity in azimuth. This provides a coherent reflecting surface in azimuth. With the pre-breaking surface, adjacent profiles change only slightly. The reflection remains coherent over a significant fraction of a wavelength, and can be predicted by the coherent addition of individual profiles. After breaking, the surface is much more random, and the profiles change dramatically within azimuthal widths on the order of a wavelength. There is no longer a coherent reflecting mechanism, so the scattering cannot be predicted by a simple coherent model.

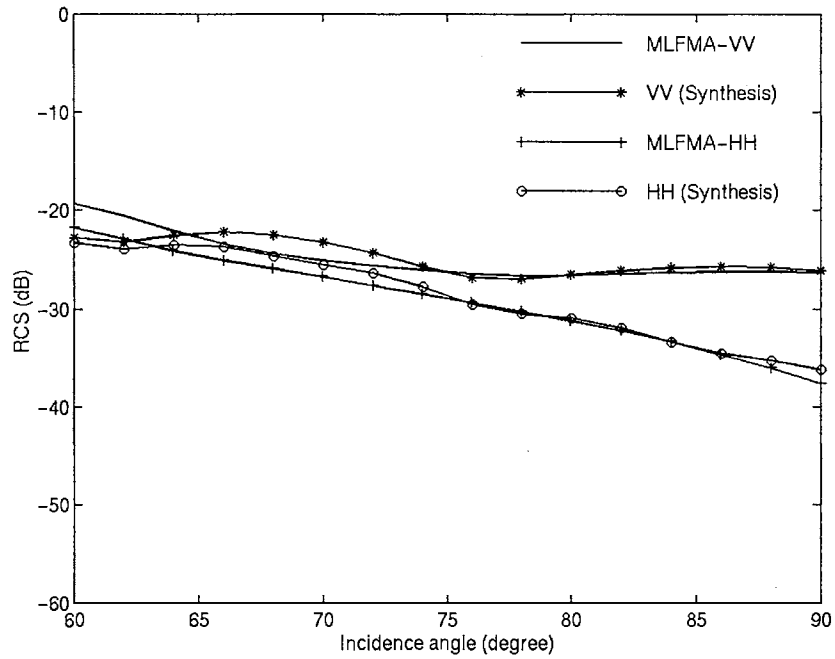


Fig. 6.8: Comparison of 2-D synthesis and 3-D MLFMA results of the pre-breaking speller.

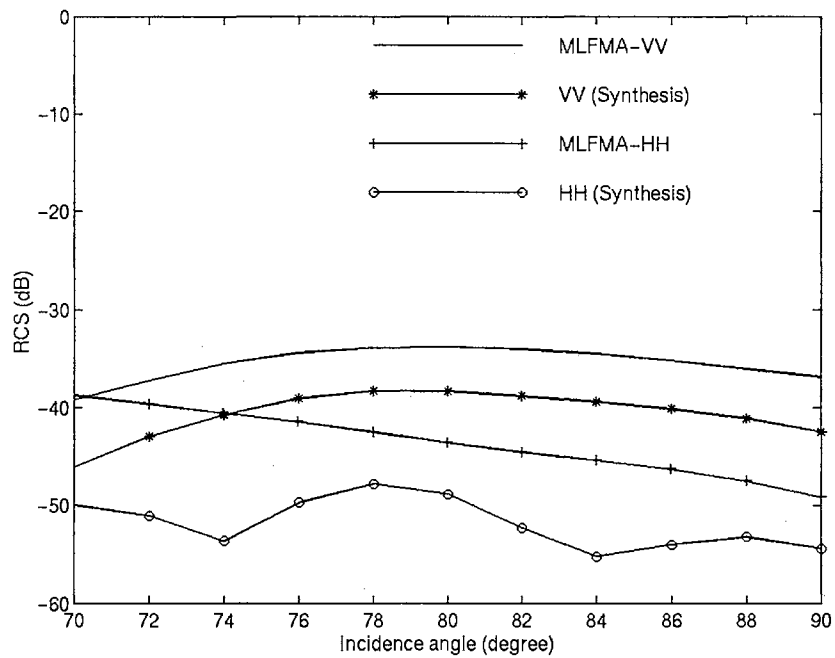


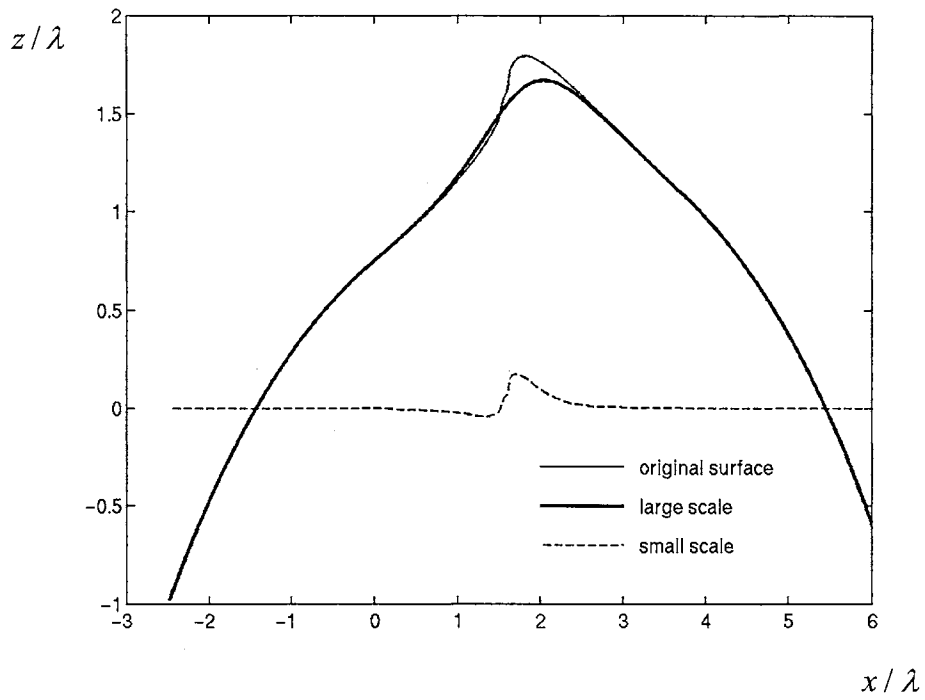
Fig. 6.9: Comparison of 2-D synthesis and 3-D MLFMA results of the post-breaking speller.

6.3.2 Two-Scale Treatment

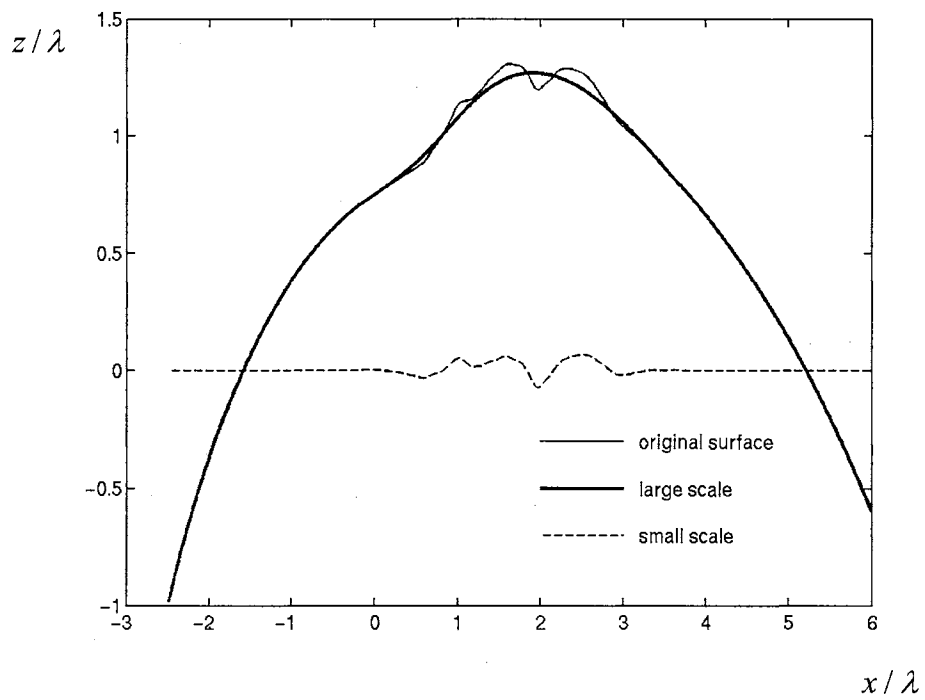
As mentioned, West and Ja [17] compared the predictions of the two-scale-model (TSM) with the numerically calculated scattering from the 2-D measured spilling breaker. Here, the analysis is extended to the 3-D profiles surfaces.

A) Surface Separation

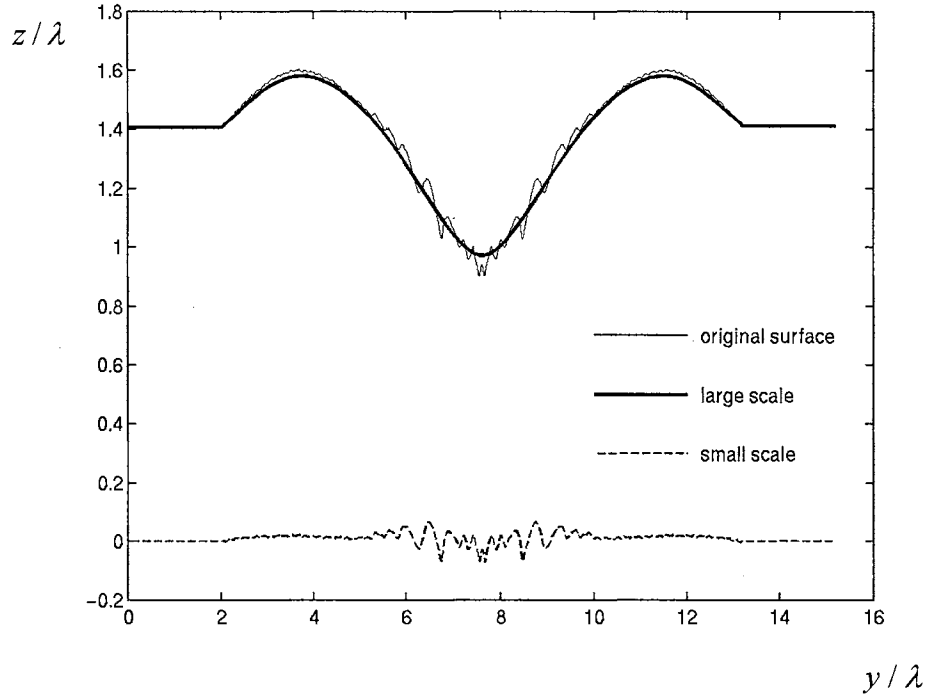
The two-scale model requires the separation of the surface into large- and small-scale rough components. This was accomplished using the procedure described in section 3.2. The surface was first sampled every 0.017λ in both the range and azimuth directions in the x - y plane projected below the surface. 850 passes of the moving average window therefore yield a scale-separation filter threshold of $K_T = k/1.7$. The number of passes was varied to give different thresholds. The cases shown use thresholds that were chosen to best demonstrate the dependence of the scattering on the threshold while providing the most accurate results. The range extensions needed for the application of the resistive loading were chosen to give very little backscatter. The moving average therefore was not applied in this region. Fig. 6.10 shows two range cuts and one azimuth cut of the surface after the filtering with $K_T = k/1.7$. Fig. 6.10a and 6.10b are the cuts along range direction for profile 150 and profile 260 respectively. Fig. 6.10c is the cut along the azimuth direction at $x=2.62\lambda$. The thin solid lines are the original profiles, the bold solid lines are the filtered large-scale surface, and the dashed lines are the small-scale surface.



a) Separation along range direction. (Profile 150).



b) Separation along range direction. (Profile 260).



c) Separation along azimuth direction. ($x \approx 2.62\lambda$).

Fig. 6.10: Separation of large-scale and small-scale surface in TSM.

B) Complete spilling-breaker wave

TSM was first applied to the complete spilling-breaker profile. Fig. 6.11 shows the results when the scale-separation filter threshold was set at $K_T = k/1.0$, while Fig. 6.12 used $K_T = k/2.0$. The solid lines show the reference MLFMA results and the starred lines show the full TSM scattering. The dashed lines show only the SPM contribution to TSM.

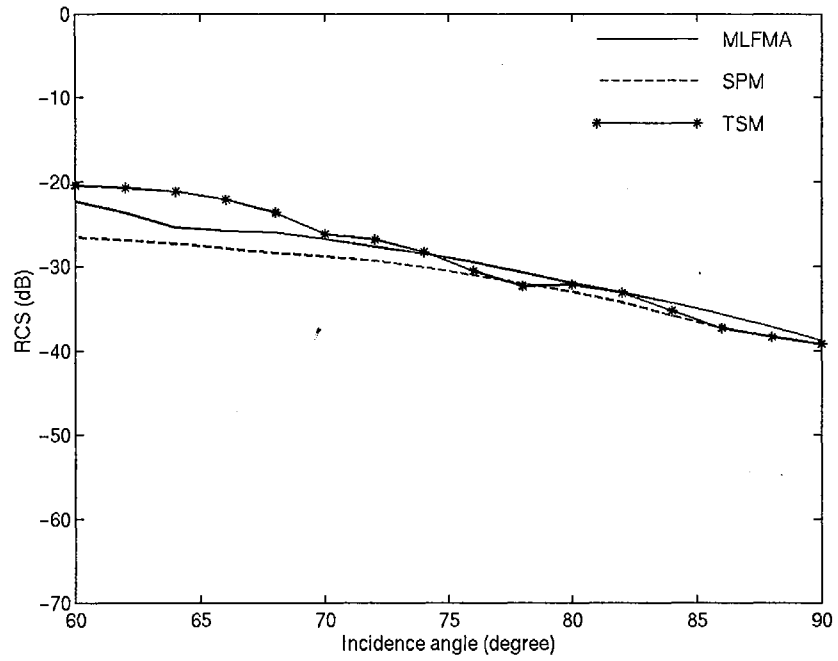
The HH TSM scattering matches the reference MLFMA results well when $K_T = k/1.0$. The average difference is about 1 dB. The agreement is poorer at VV. When the threshold is reduced to $K_T = k/2.0$, VV agreement improves at the expense of poorer HH agreement. No threshold could be found that yielded accurate results at both polarizations. This threshold dependence is likely due to the inclusion of the steep, pre-breaking portion of the wave. West and Ja [17] showed that TSM is unable to treat

scattering from the individual 2-D profiles that included steep features. This is also demonstrated by the large contribution of the KA field. The KA scattering is strong for near-specular reflection, which would result with the steep features. West and Ja also showed that the two-scale model was more effective with the 2-D profiles after breaking when there were no longer steep features. TSM is therefore now applied to the post-breaking profile of Fig. 6. 5.

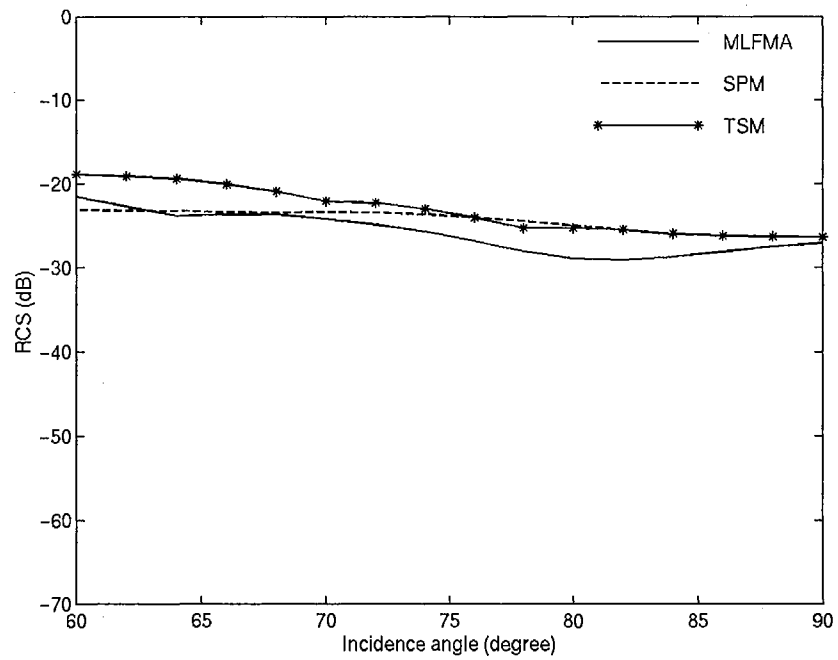
C) Post-breaking wave

Figs. 6.13-15 show the results of TSM applied to the post-breaking spiller with separation thresholds of $K_T = k/0.8$, $K_T = k/1.2$ and $K_T = k/1.6$. The results are less sensitive to the threshold than in the full wave case. Agreement is reasonably good at both polarizations with all thresholds with best overall agreement with $K_T = k/1.2$. In [17], West and Ja have shown that $K_T = k/1.6$ is the best choice for the 2-D case after breaking. Despite the good agreement that is obtained here, the need to arbitrarily choose a scale-separation threshold remains the most significant limitation of TSM.

The good agreement here provides further demonstration that the scattering in Fig. 6.7a is not significantly affected by the front-face extension above 70^0 .

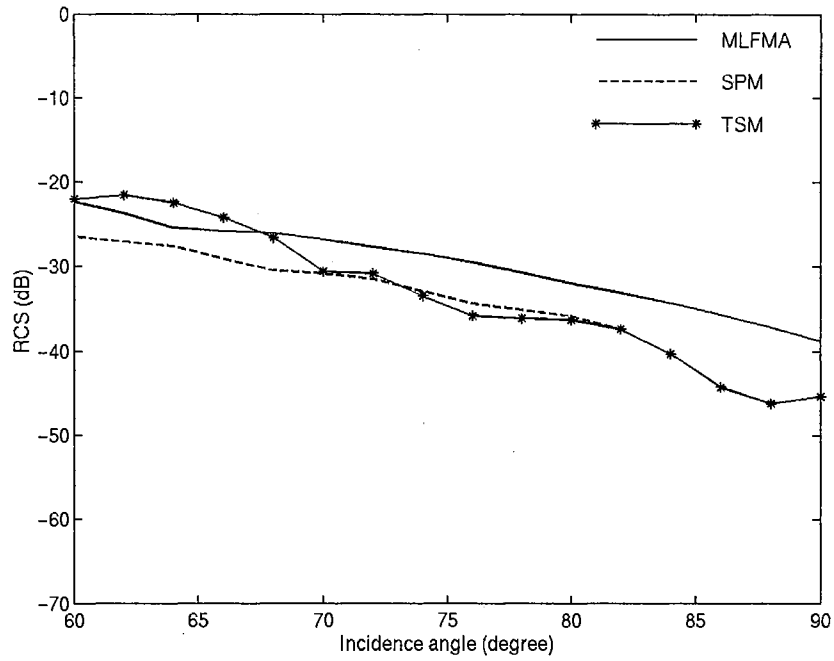


a) HH

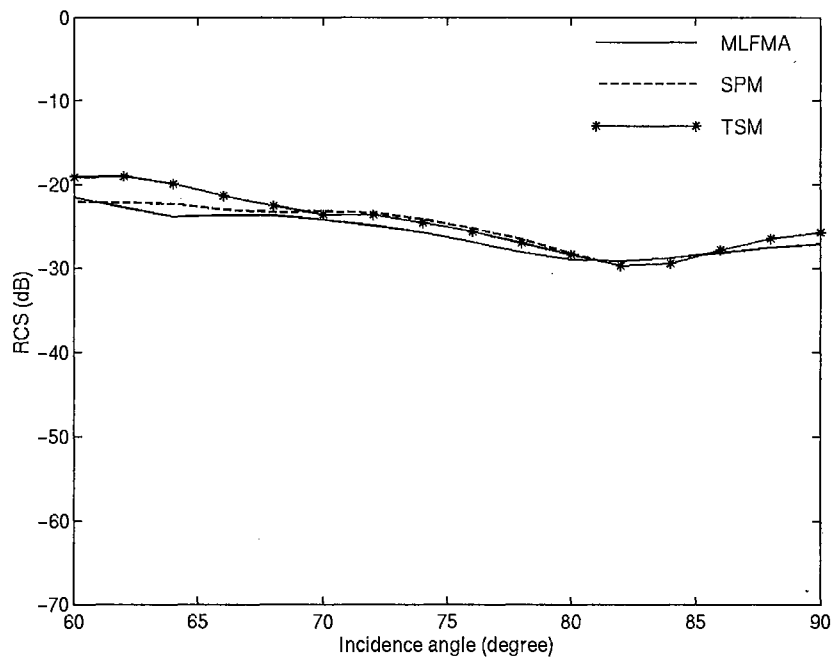


b) VV

Fig. 6.11: TSM scattering from complete spilling-breaker using $K_T = k/1.0$.

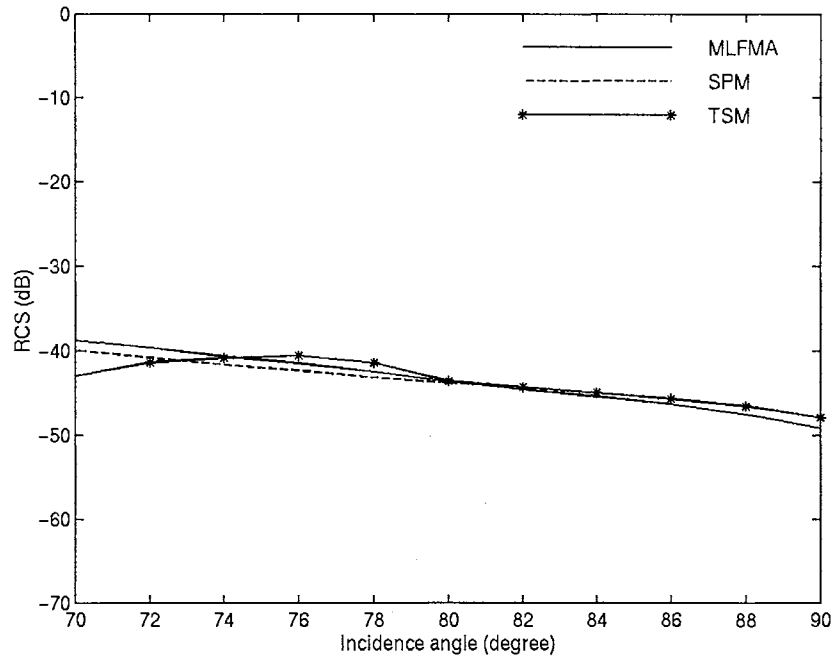


a) HH

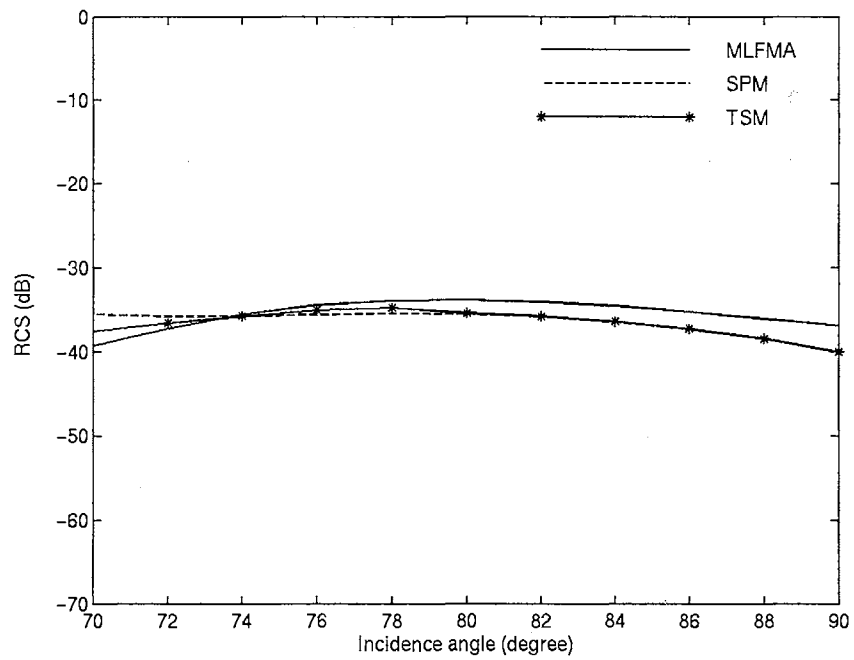


b) VV

Fig. 6.12: TSM scattering from complete spilling-breaker using $K_T = k/2.0$.

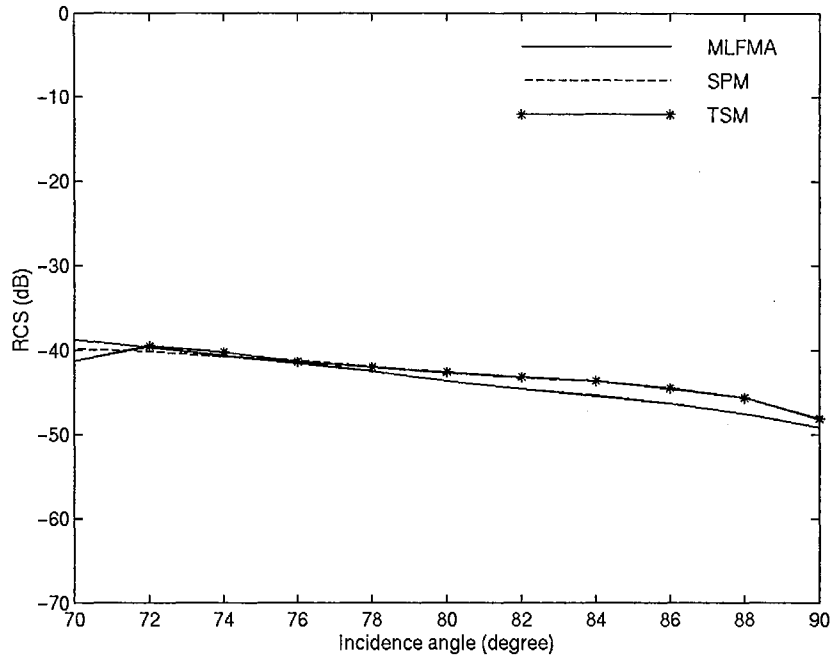


a) HH

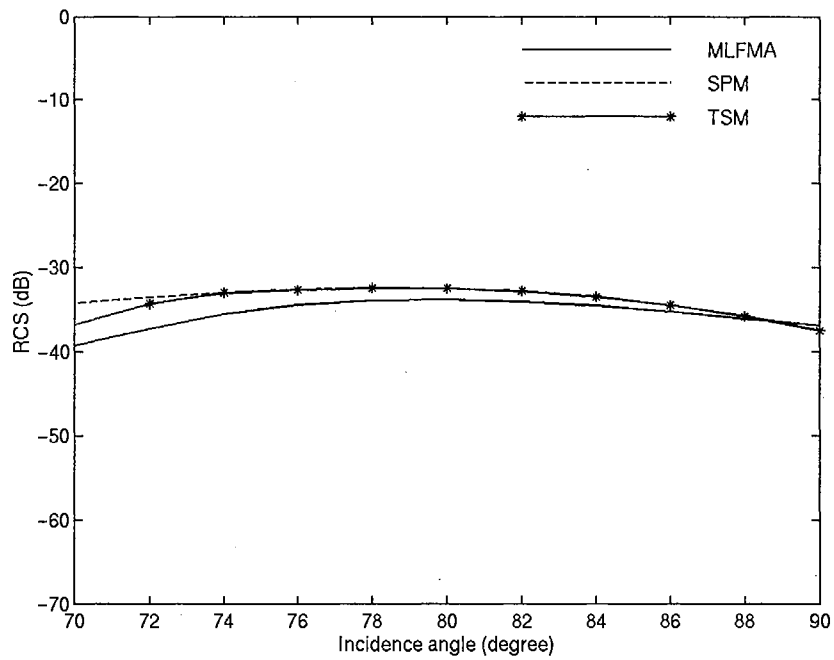


b) VV

Fig. 6.13: TSM scattering from post-breaking spilller using $K_T = k/0.8$.

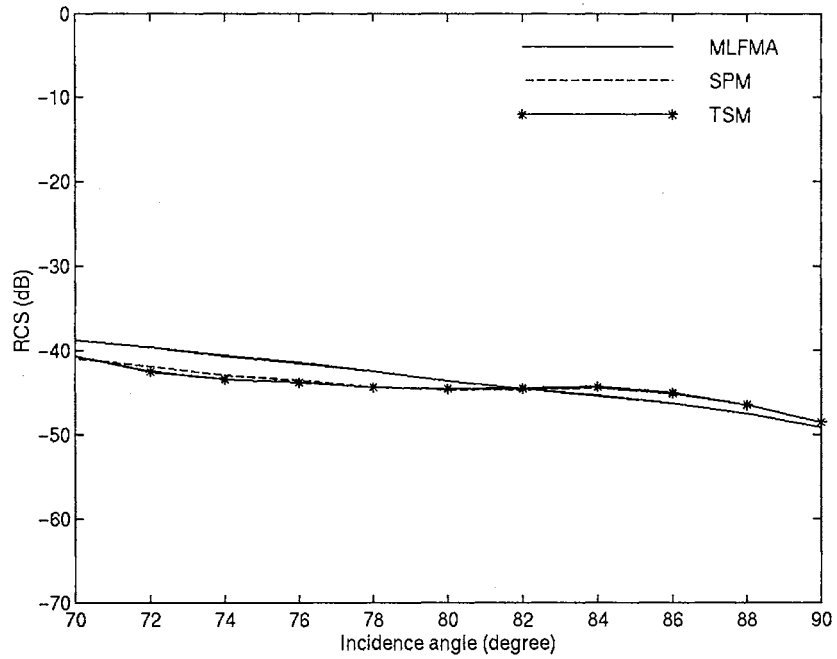


a) HH

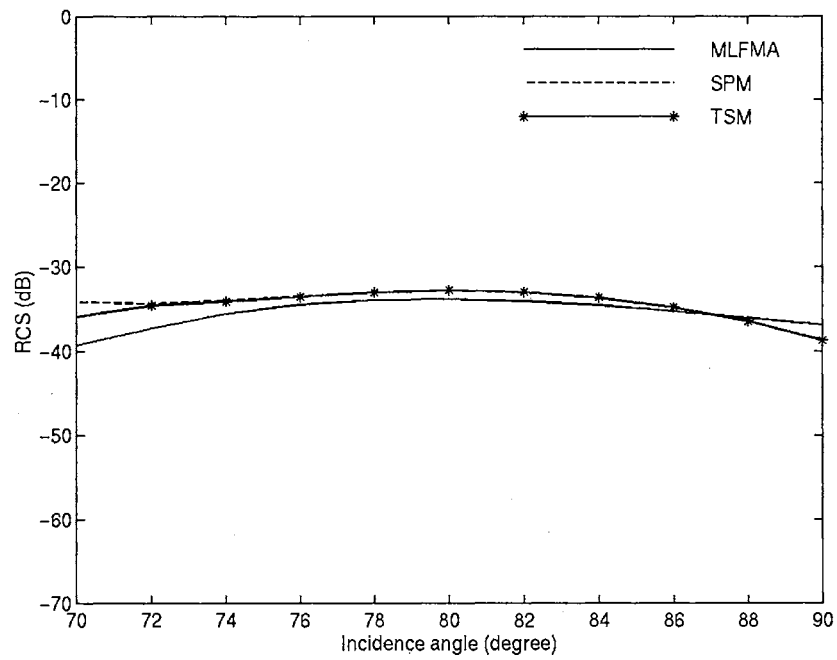


b) VV

Fig. 6.14: TSM scattering from post-breaking spillier using $K_T = k/1.2$.



a) HH



b) VV

Fig. 6.15: TSM scattering from post-breaking spilller using $K_T = k/1.6$.

CHAPTER 7

PLUNGING BREAKER SCATTERING

In this chapter, the MLFMA numerical routine is used to examine the backscattering from a 3-D profile derived from the measured 2-D wave tank history of a plunging breaker shown in Fig. 1.3. The calculated results are compared with the predictions of the EGO/GTD model as well as a 3-D cross-section synthesized from the 2-D MM/GTD scattering.

7.1 Scattering Surface

The original plunging breaker shown in Fig.1.3 was measured under similar conditions to the previous spilling breaker. However, a high concentration of soluble surfactant, Triton X-100, was added to the water. Surfactants produce a number of changes to the dynamical water surface properties, leading to more energetic breaking. In particular, there are two overturnings near profiles 160 and 206. These corresponded to the strong super events seen in the 2-D scattering in Fig. 2.6.

A 3-D plunging-breaker crest was formed from profiles 90 through 311 of the individual 2-D profiles of Fig. 1.3. Referring to Fig. 2.6, the 2-D scattering from profile 90, when the crest is still round, is small compared with the scattering at later times. This profile was therefore extended over 2λ in the azimuthal direction. The resistive loading

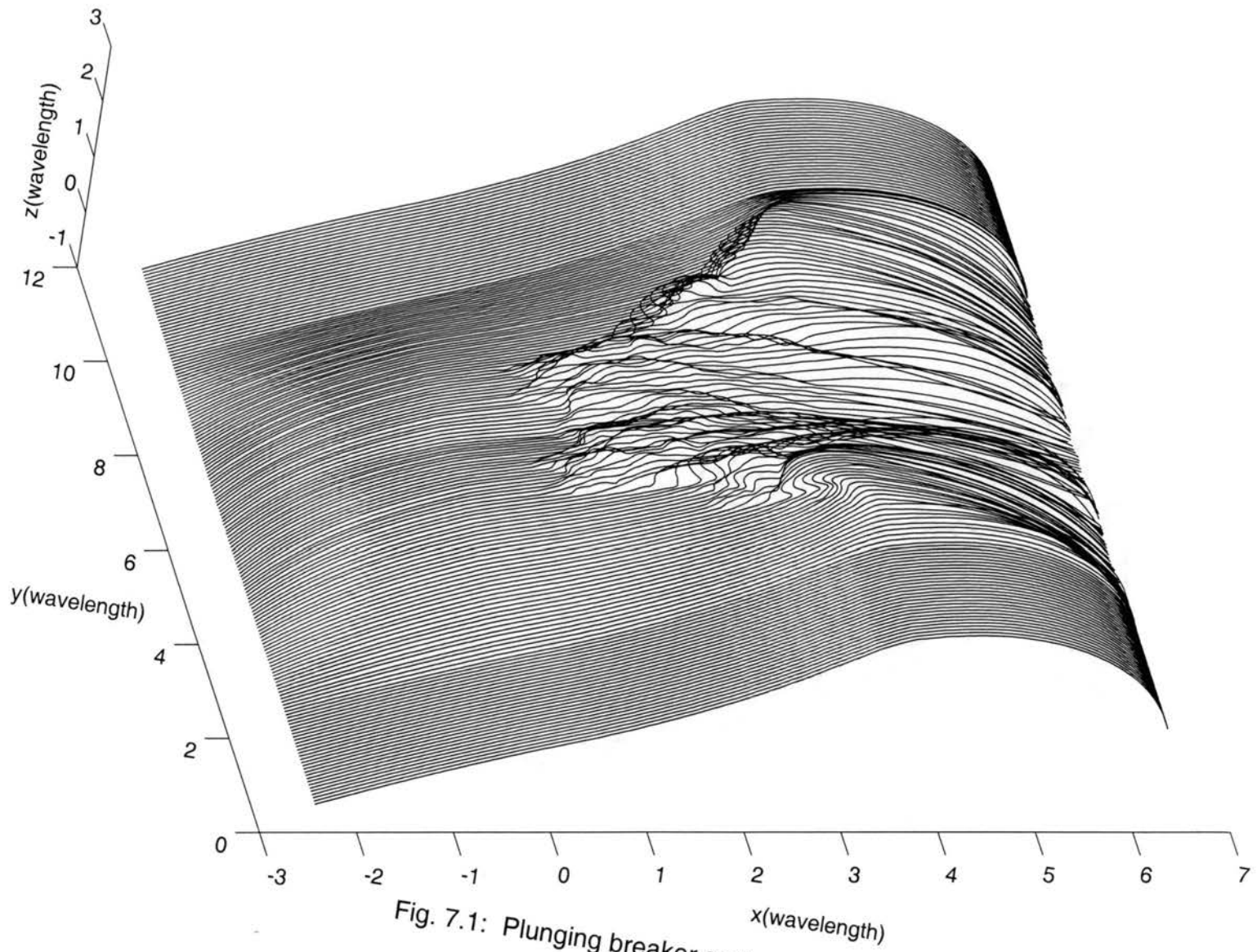


Fig. 7.1: Plunging breaker surface.

was applied over this width, and the total backscatter from this region was therefore assumed to be zero. The extension in the range direction followed the same steps as the spilling breaker in Chapter 6. Fig. 7.1 shows the complete of plunging-breaker surface with the extensions. The resistive taper was also applied over these extension areas in both the range and azimuthal directions.

7.2 MLFMA Scattering

The frequency of the following results was once again 10 GHz and the surface impedance was $Z_s = 44 + j13\Omega$ for seawater. The sampling step in the range direction (along the arc-length) was 0.05λ , and was 0.07λ in the azimuthal direction. In all of the following figures, the solid lines show VV backscattering, the dashed lines are for HH, the circled lines are for HV, and the starred lines stand VH.

7.2.1 Scattering of the Complete Surface

Fig. 7.2 shows the scattering from the plunging breaker profile of Fig. 7.1. Although the azimuthal extent of this crest is less than that of the spilling breaker, it has a scattering cross-section that is several dB larger. This results because the breaking is more energetic, giving more and larger steep sections that give large cross-sections. HH is consistently higher than VV by approximately 2 to 4 dB above 65° incidence. However, the large super events observed in the 2-D scattering from individual profiles is not evident. This is because the overturnings were of short duration, and only form a small part of the complete crest. The total energy contribution at these points is therefore small, and HH exceeds VV for only slightly for the complete surface. The HH and VV cross-sections show little dependence on the angle of incidence above 65° . The cross-

polarization cross-sections show some disagreement, indicating that they are affected by numerical error. However, it does appear that ratio of the cross-polarized to co-polarized scattering is higher than for the spilling breaker. This may be because that the surface of plunging breaker changes more rapidly azimuthally than the spilling-breaker, giving more multiple scattering.

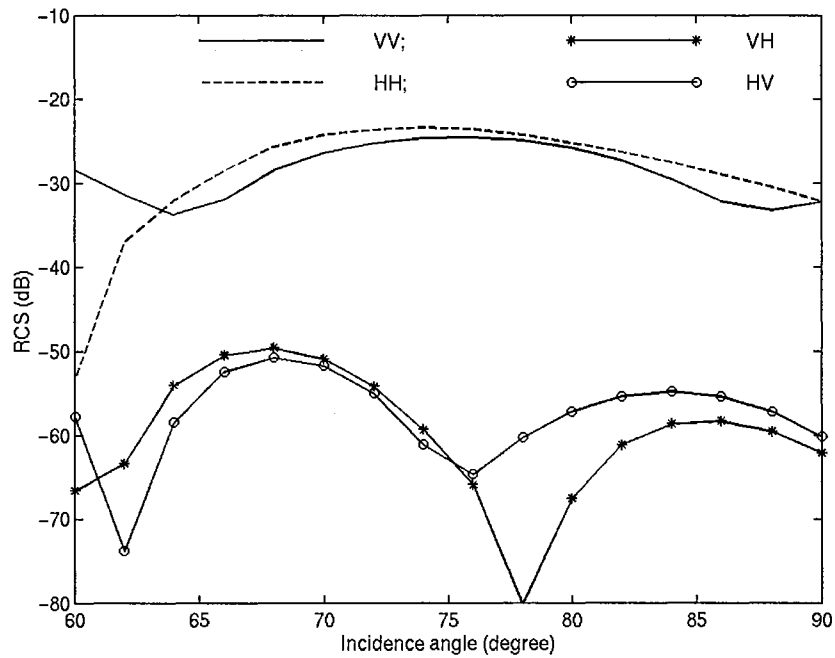


Fig. 7.2: Backscattering from complete plunging breaker by using MLFMA.

7.2.2 Initial Breaking

The full plunging-breaker surface is unrealistic because the surface features are too narrow. That is, the azimuthal width of the overturning and other sections are unrealistic. Efforts are currently under way to synthesize a more realistic 3-D profile from the 2-D measurements. For now, however, a narrower profile formed from only the first overturning will be used to test the analytical models. The surface used is shown in Fig. 7.3. It was formed from measured 2-D profiles 90 through 190, and therefore includes the

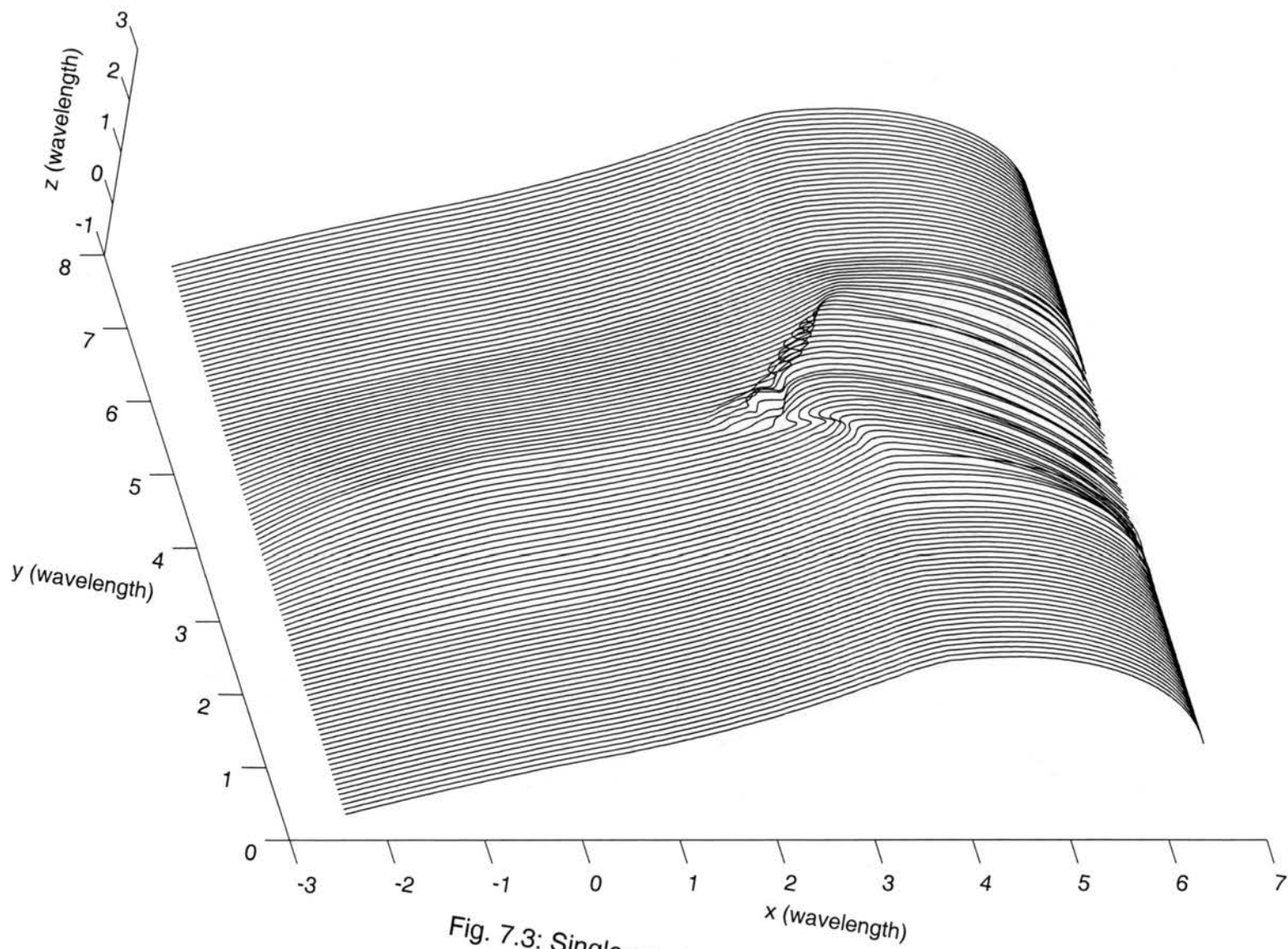


Fig. 7.3: Single-overturning plunging breaker.

first overturning only. Profile 90 was again extended over 2λ and the front and back faces extended as in Section 7.1 to allow the addition of the resistive loading.

Fig. 7.4 shows the backscattering from the initial-breaking surface. Here, there is a null in the VV backscatter at 86° that is not matched at HH, leading to a 30 dB super event. Below 80° incidence both HH and VV are approximately constant at -30 dB, which is several dB below that in Fig. 7.2. This indicates that, unlike the spilling breaker, the initial overturning alone does not dominate the scattering.

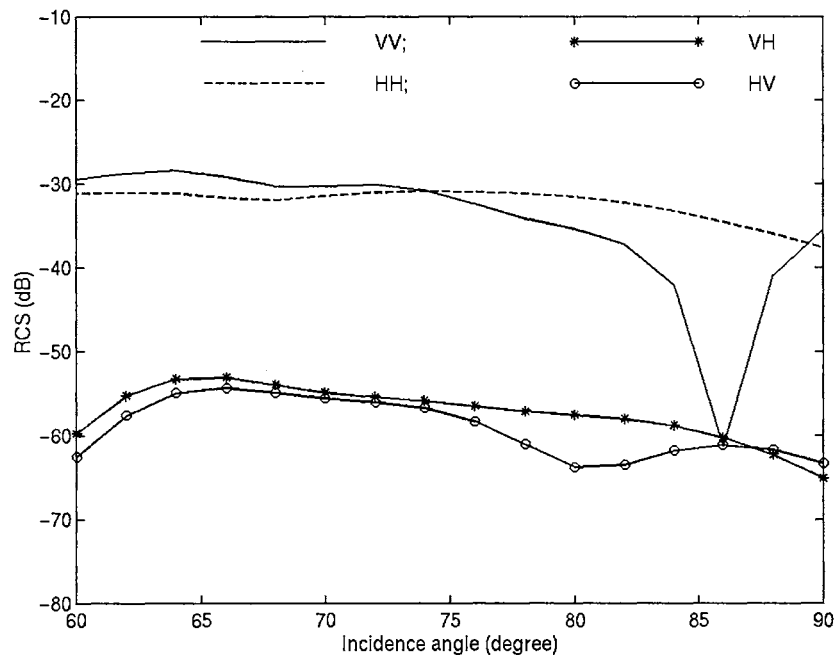


Fig. 7.4: Backscattering from initial-breaking surface by using MLFMA.

7.3 EGO/GTD in Breaker Water Wave

The null in Fig. 7.4 is similar to that observed in the 2-D scattering calculations of Fig. 2.6. Obviously with the specular-like reflection from steep features the two-scale model is not appropriate for examining the scatter [17]. Instead, EGO extended to 3-D surface is

used. Previously, 2-D EGO/GTD was used only with the numerically generated LONGTANK waves [91]. The EGO analysis here will therefore first treat the 2-D measured profiles to insure that the technique is useful with more realistic wave shapes. It will then be applied to the 3-D single overturning surface. The 2-D analysis is limited to sample profiles to compose the 3-D surface of Fig. 7.3.

7.3.1 2-D EGO/GTD in Plunging Breaker

Three different 2-D profiles from the initial overturning were considered in the 2-D EGO/GTD test, shown in Fig. 7.5. Profile 130 was taken from the initial steepening stage, while the jet is beginning form in profile 150. The jet is fully developed in profile 160. Note that the jet has likely blocked the view of the video camera of the cavity under the jet in profile 160, leading to a distorted measurement of the cavity. The calculated cross-sections are unlikely to be exact. However, this surface does give an opportunity to test EGO under realistic conditions.

The reference 2-D cross-sections were found using MM/GTD. Thus the surfaces were artificially extended in both sides by adding constant radii of curvature, concave downward arc sections to a slope from horizontal of 40° , and then extended to infinity on either side by planar sections of sloped at 40° . Fig. 7.6 shows profile 160 after the extensions. This extension induces two diffraction points on the front surface (the incidence wave is from right to left). The stars in Fig. 7.6 are two induced diffraction points on the front surface. The radii of the curved extensions are 20λ to minimize the introduced diffractions. The diffraction points of the back surface are shadowed and therefore they are neglected.

Fig. 7.7 shows an expanded view of the jet of profile 160. There are two specular reflection points on the crest at 90° incidence, shown by the circles. These points are treated using EGO reflection. Also shown is the inflection point where the surface transitions from concave to convex, marked by an asterisk. This is a source of diffraction, which is treated using EGO corrected GTD. The positions of the reflection points will change with incidence angle, while the diffraction point is fixed.

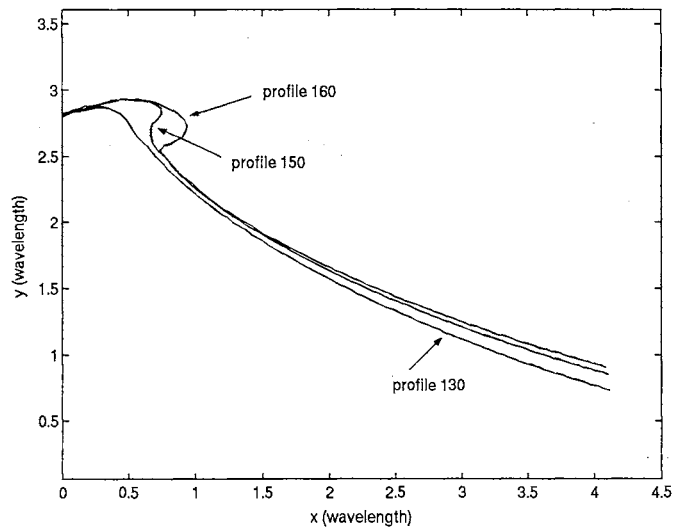


Fig. 7.5: Surfaces used in 2-D EGO/GTD.

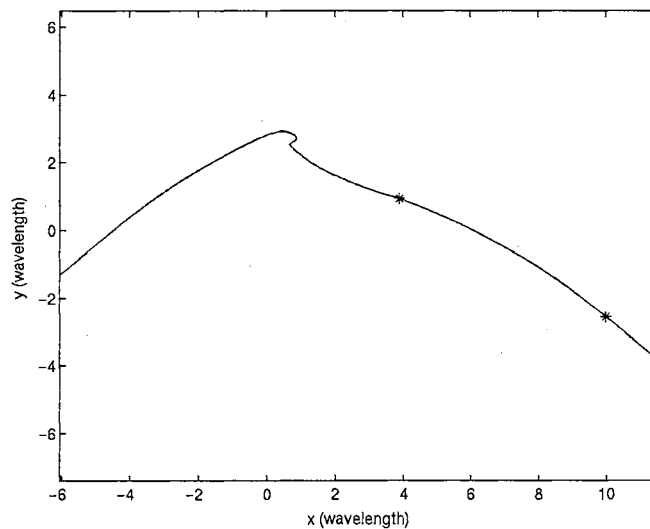


Fig. 7.6: Profile 160 with extensions at both sides.

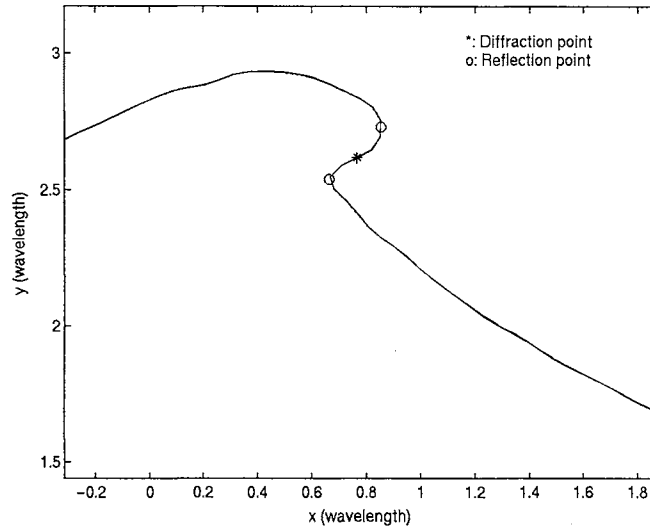


Fig. 7.7: Enlarged profile 160 with reflection points and diffraction point.

The radius of curvature is a critical parameter in calculating EGO and GTD scattering. Because these profiles are taken from measured plunging-breaker, the noise of the measurement makes the measured surface coarser than the real surface. Therefore averaging should be used to the either side of the reflection points and diffraction points to get more realistic radii of curvature. In initial tests, the averaging length is 0.125λ to either side of the reflection points and is 0.1λ to either side of the diffraction points. All test cases are again presented with an operating frequency of 10 GHz and a surface impedance of $Z_s = 44 + j13\Omega$, corresponding to seawater.

Fig. 7.8 shows the scattering from profile 130. From Fig. 7.5, this surface is just beginning to steepen. There are no specular reflection points when incidence angle is larger than 60° , so diffraction from the inflection point is the only source of scattered field. The solid and crossed lines show the reference MM/GTD results for VV and HH, respectively. The starred and circled lines are VV and HH found from EGO/GTD, respectively. Excellent agreement between MM/GTD and EGO/GTD is achieved at both

polarizations. GTD extended by EGO can therefore accurately predict the scattering from surfaces that include the initial plume steepening.

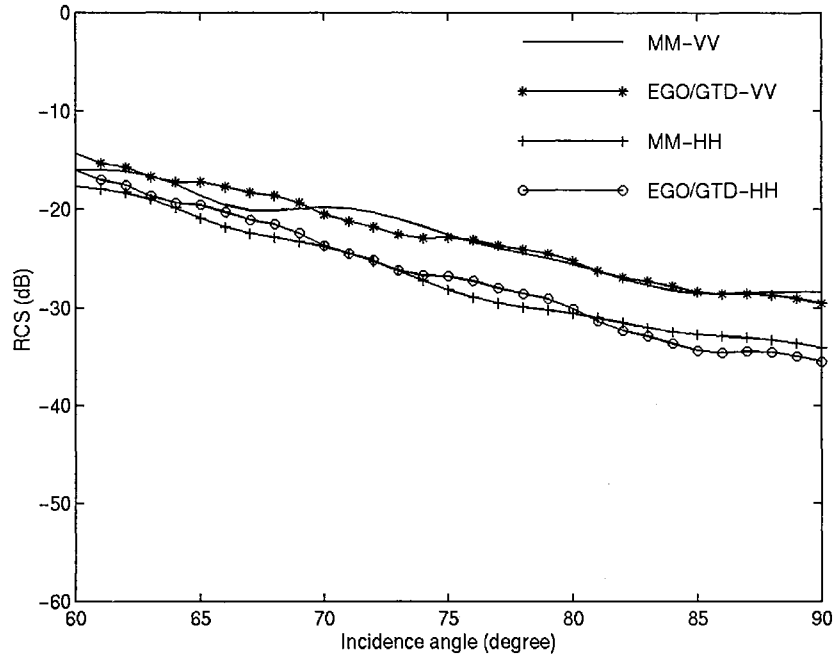


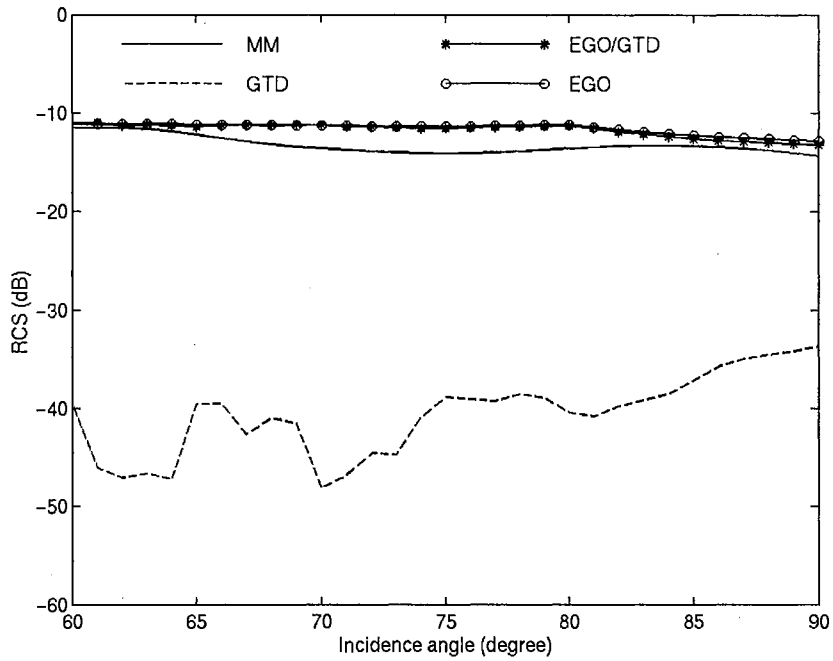
Fig. 7.8: Comparison of MM/GTD and EGO/GTD of profile 130.

Fig. 7.9 shows the scattering from profile 150. Here the jet has formed. There are two reflection points when the incidence angle is greater than 60° , one on the convex jet and the other on the concave cavity under the jet. There is also an inflection point between the convex and concave sections which gives rise to diffraction treated by GTD. The curvature was again averaged over 0.125λ on either side of the reflection points. The radii of curvature at the convex and concave reflection points after averaging are about $1/5\lambda$ and $1/4\lambda$ respectively near 90° incidence. The solid lines show the reference MM/GTD results, the dashed lines show the GTD contributions for the diffraction from the inflection point, the circled lines show the EGO reflection contribution, and the starred lines are the combined EGO/GTD contribution. The GTD contribution is very

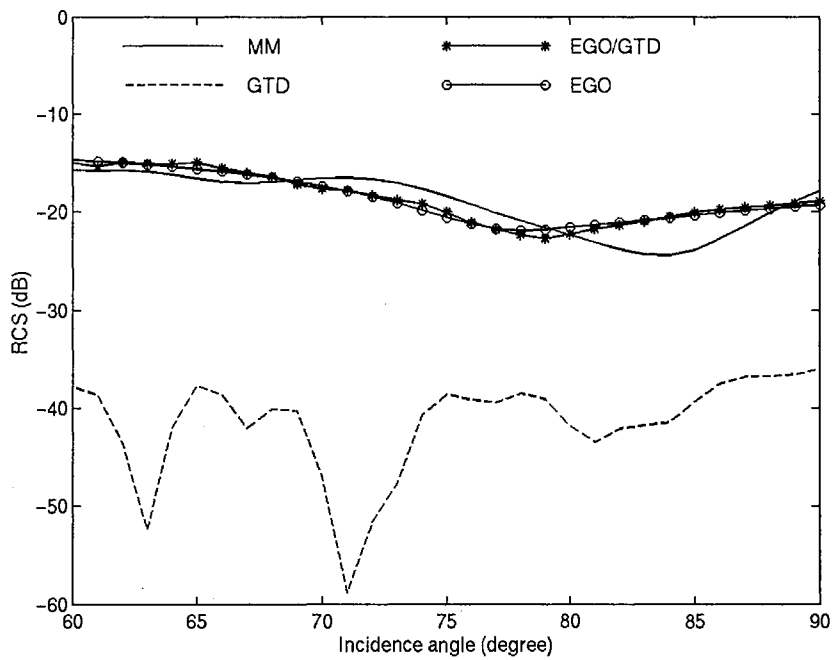
small. The main contribution of the total modeled scattering comes from the EGO reflection. The EGO/GTD results match well with that of MM/GTD overall, with a maximum error of 3 dB. The HH>VV super event is accurately predicted.

EGO/GTD was further investigated using the more complicated profile 160. A very strong super event occurs with this profile (up to 20 dB). Again there are two reflection points and one inflection point. Because the jet of profile 160 is obviously larger than that of profile 150, the average lengths used to get the radii of the convex and concave reflection points were increased to 0.5λ and 0.28λ (both sides together), respectively. The EGO contribution again dominates the scattering. The radii at the convex and concave reflection points after averaging are about $1/4\lambda$ and $1/7\lambda$, respectively, near 90° incidence. Fig. 7.10 shows the calculated scattering from profile 160. EGO/GTD shows good agreement with MM/GTD at HH. VV agreement is poorer above 75° . In particular, EGO/GTD underestimates the depth of the null at 78° , and then underestimates the magnitude at higher incidence.

The averaging length used in the previous figure is somewhat arbitrary. Because the results may be sensitive to the radii of curvature of the reflection points, other averaging lengths were used here. Fig. 7.11 shows the scattering when different averaging lengths were used on the convex reflecting surface for profile 160. The averaging length for the reflection point at the concave was 0.28λ in all case, giving a $1/7\lambda$ radius of the concave near 90° incidence. The resulting radius at the convex reflection point was $1/4\lambda$, $1/3\lambda$ and $1/4.5\lambda$ for cases 1, 2 and 3 plotted in Fig. 7.11, respectively. (Case 1 was shown in Fig. 7.10). Fig. 7.11 shows that HH is almost unchanged in the three cases. It is not sensitive to the change in radius. VV shows strong changes around the null, how-

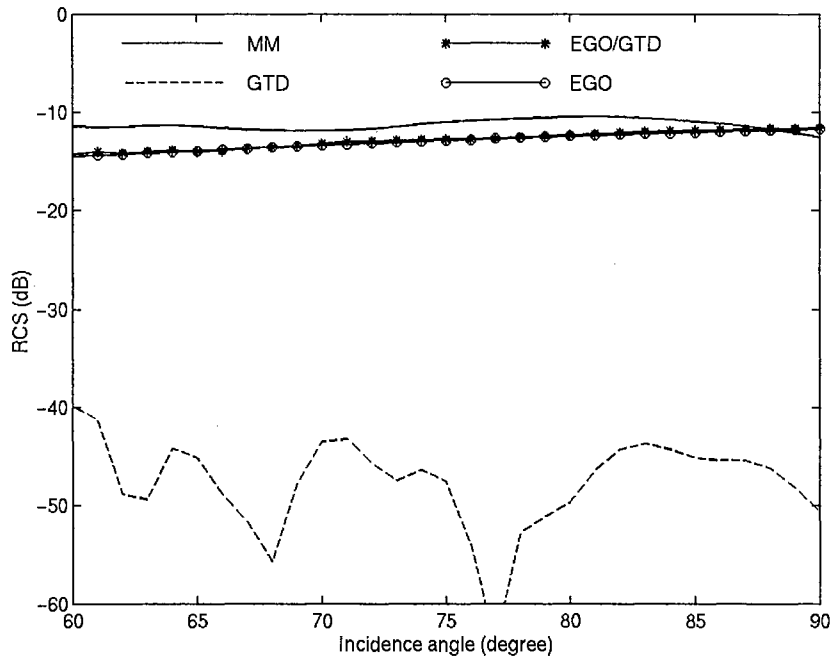


a) HH

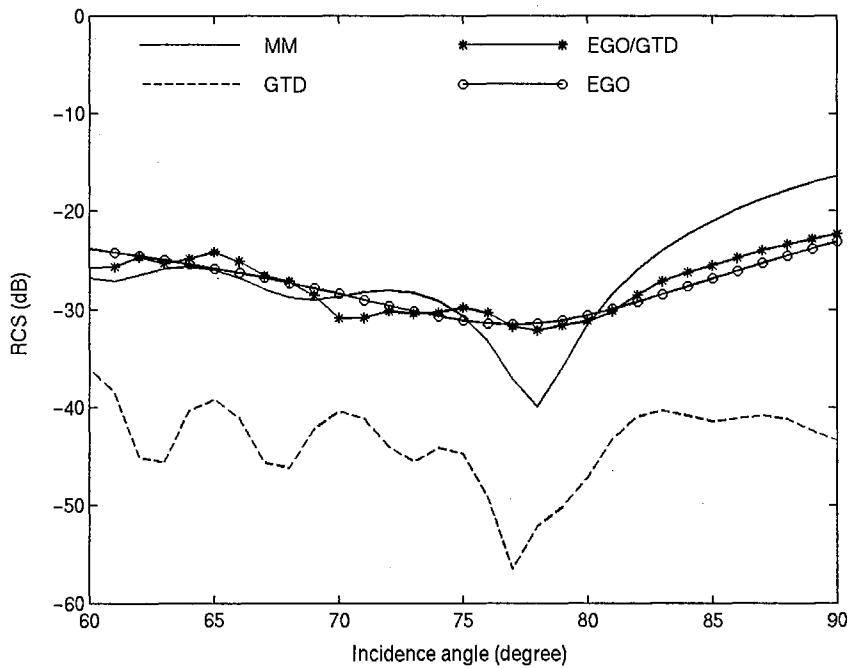


b) VV

Fig. 7.9: Comparison of MM/GTD and EGO/GTD of profile 150.

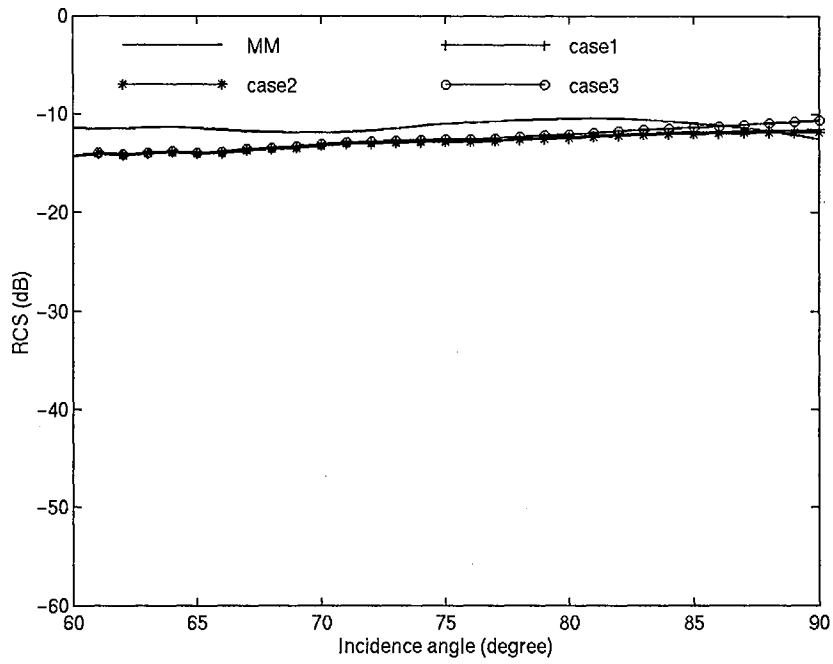


a) HH

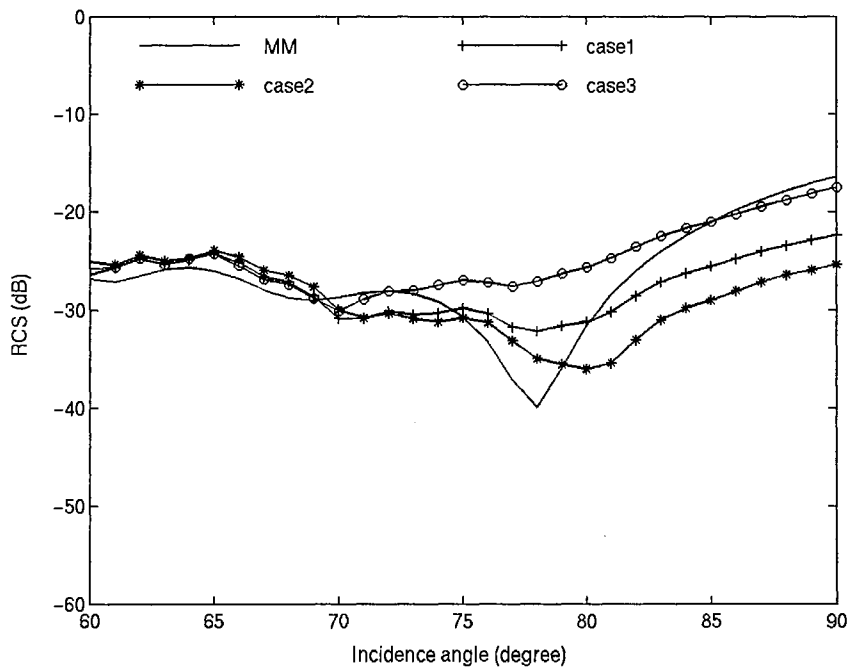


b) VV

Fig. 7.10: Comparison of MM/GTD and EGO/GTD of profile 160.



a) HH



b) VV

Fig. 7.11: Comparison of MM/GTD and EGO/GTD of profile 160 with different smooth length.

ever. This results because the null is due to destructive interference in the EGO reflection from the two specular points. The phase of the reflection varies quickly with changing radius, changes the interference.

EGO/GTD works fair well for these different profiles. The results showed that interference of the field reflected from the two reflection points form the nulls of profiles 150 and 160. EGO/GTD can predict the nulls and the super events though they are not very accurate. Little change of radii may bring big change in phases and big differences around the null. The null in profile 160 is even deeper. It is even sensitive to the radii of curvature. However, EGO/GTD is still useful in the analysis of dominant scattering of surfaces. The positive conclusion of 2-D EGO/GTD motivated us to investigate EGO/GTD in 3-D surfaces.

7.3.2 3-D EGO in Plunging Breaker

Three-dimensional EGO was applied to the initial plunging surface shown in Fig. 7.3. This surface was chosen because it includes a well defined breaking that should be treatable using quasi-specular reflection points. The later stages are quite artificial and not likely to represent conditions in open sea. As the 2-D study showed that the specular reflection overwhelmed diffraction when overturning occurs, GTD based diffraction is ignored. It is stressed that the 3-D EGO study presented here is preliminary. The wave surface is not likely to be realistic, and the results should not be applied to actual cases. It is simply presented as a test.

No automated procedure was developed to apply EGO to the 3-D profile. Instead, the reflection points were first identified in the 2-D profiles, and those were used to identify the 3-D reflection points. The radii of curvature of these reflection points in the along-

track direction were first coarsely approximated from the radii of 2-D profiles. The radii of curvature across-track (azimuthal) were coarsely presumed according to geometry in this direction. The locations and the radii of these reflection points were then manually adjusted. This is a somewhat arbitrary procedure. An automatic procedure is clearly needed in the future. Fig 7.12 shows the scattering surface with the identified reflection points designated numerically. Five reflection points were identified. The adjusted radii and locations associated with each reflection point used in the EGO calculations are list in Table 7.1. ρ_r stands for the radius of curvature in the range direction and ρ_a is the radius of curvature in the azimuth (transverse) direction. A negative value means that the surface curvature was concave at the reflection point in the plane of interest, and a positive value indicates convex curvature.

Table 7.1 Parameters of reflection points.

Point number	1	2	3	4	5
ρ_r (wavelength)	0.40	0.40	0.40	0.25	-0.1
ρ_a (wavelength)	0.38	0.60	-0.22	0.18	0.1
Location: x	2.60	2.905	2.68	2.33	2.30
(wavelength) y	1.43	1.02	1.735	1.735	1.735
z	2.43	2.85	2.575	2.248	2.135

Fig. 7.13 shows a comparison of the modeled EGO and reference MLFMA scattering. The solid and dashed lines show the MLFMA VV and HH results, respectively. The starred and circled lines show the EGO VV and HH results. Fig. 7.13a is the result with all the five reflection points, 1 through 5. Both VV and HH appear fairly accurate. In particular, VV EGO predicts the null at 86° . However, it should again be

stressed that manual adjustment of the parameters in Table 7.1 was needed to get such good agreement. Without the adjustment the null depth was inaccurate, and larger oscillations appeared in the scattering below 80° incidence.

Fig. 7.13b shows the EGO results when reflection point 2 was omitted. In this case, the VV null is not predicted. The scattering is dominated by the reflection from point 1, and therefore is approximately constant at all grazing angles. Interestingly, the superevents in the 2-D scattering from the individual profiles resulted in interference between concave and convex reflection points. The phase difference in the VV and HH reflections due to the EGO corrections led to differing interferences, giving the superevent. Here, it appears that the VV null results from interference between two convex reflections. Again, the EGO corrections change the phases at the two polarizations, however, which again leads to VV cancellation.

As mentioned, efforts are currently underway to synthesize more realistic 3-D plunging breaker from the 2-D measurements. An automated EGO procedure should be possible with these more realistic profiles. The limited success of these preliminary results indicates that there is merit in continuing the EGO analysis with the more realistic surfaces.

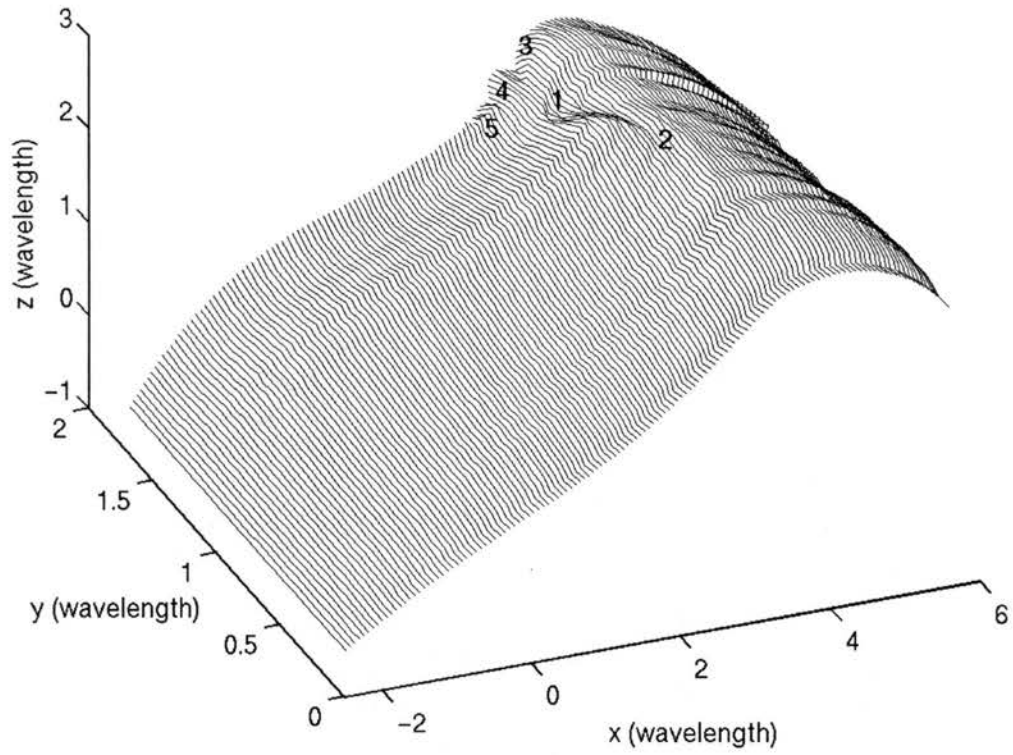
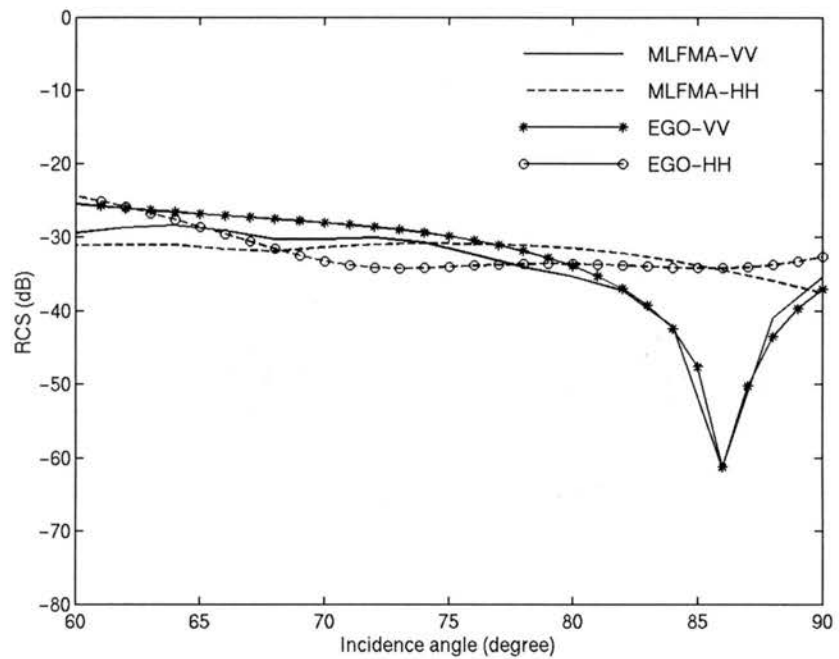
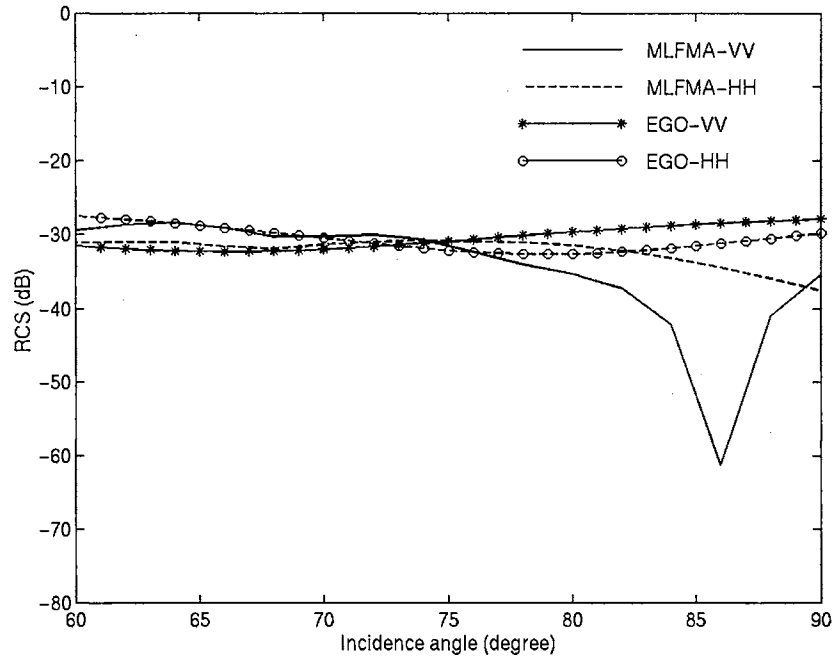


Fig. 7.12: Surface used for 3-D EGO.



a) Using reflection points 1 through 5.



b) Using reflection points 1, 3 and 4 and 5.

Fig. 7.13: Comparison of 3-D EGO and MLFMA results.

CHAPTER 8

SUMMARY AND CONCLUSIONS

A numerical method to analyze the backscattering from rough water surfaces approximating breaking water wave has been implemented. A moment method code was implemented using RWG basis functions to model arbitrary, three-dimensional surfaces. The moment method was accelerated using the multilevel fast multipole algorithm (MLFMA). Impedance boundary conditions were used to represent the finite conductivity of the sea water.

The resistive taper loading method of suppressing edge diffraction that was developed for 2-D scattering was extended to the 3-D problem in this paper. Comparison between the scattering from sample 3-D profiles that were uniform in one dimension with reference 2-D calculations confirmed the effectiveness of the resistive loading. MLFMA with resistive loading was then used to analyze the scattering from 3-D breaking waves for the first time. Some important conclusions were obtained. These 3-D MLFMA results were compared with 2-D results found using MM/GTD. The standard moment method is critically limited by the resources of computer. Especially for large 3-D surfaces, computer resources become a bottleneck for the numerical method. MLFMA dramatically reduces the computational loads allowing 3-D profiles to be treated. However, computational load is still a problem. On the other hand, analytical models are

more efficient, but are only valid under specific conditions that must be ascertained. MLFMA provides a tool to evaluate the effectiveness of analytical models. In this paper, the validities of several analytical models were investigated when applied to 3-D breaking waves for the first time. MLFMA was used as the reference to evaluate these models. It was demonstrated that a 2-D synthesis of the 3-D cross-section could be used to accurately predict the scattering from the pre-breaking part of the spilling breaker.

The numerical method provided insight into the previously used analytical methods. TSM performed poorly with both the pre-breaking and complete spilling-breaker surfaces. The results proved very sensitive to the scale-separation threshold used. It proved more effective with the post-breaking surface. The results of TSM matched the MLFMA results well with a separation threshold of $K_T = k/1.2$. The results were not as sensitive to K_T as with the complete surface. EGO/GTD was also applied to measured water waves for the first time. It was demonstrated that EGO/GTD worked reasonably well with the 2-D breaking profiles even when the surface radii of curvature at the reflection points were as small as $\lambda/5$. Super-events were predicted using this simple mode. A preliminary study applying EGO/GTD to 3-D breaking crests was performed. The initial results demonstrated that EGO/GTD may have the potential to model the backscattering from realistic 3-D plunging crests, although more work is required to develop automated routines to find the appropriate reflection points.

The numerical scattering code was used to find the scattering from 3-D rough surface profiles that represent the crests of breaking water wave. No directly measured 3-D crests profiles were available. Instead, 3-D profiles were synthesized by azimuthally aligning consecutive 2-D profiles measured from waves mechanically generated in a wave tank.

The profiles are therefore not expected to be entirely realistic. However, they have provided test cases to which the numerical technique may be applied, allowing the testing of existing analytical models under realistic conditions. Two different wave profiles were considered. The first was obtained from a low-energy spilling breaker that had minimal overturning. The second had more energetic plunging breaking with extensive jetting.

The spilling breaker was naturally divided into two different regions, pre-breaking and post-breaking. The pre-breaking sections included a bore feature on the steep crest while the post-breaking region showed regions of turbulence. Separate surfaces were formed from the pre- and post-breaking regions, as well as from the complete surface. The scattering from the pre-breaking surface proved consistent with that expected from quasi-specular reflection from the bore feature. HH and VV backscattering were approximately equal at 60° incidence, with HH decreasing as the incidence angle increased. Little cross-polarized backscattering was observed. The post-breaking surface scattering, on the other hand, had no steep features to give specular-like reflection. The scattering was therefore Bragg-like from the turbulent roughness. VV backscatter exceeded HH at all incidence angles. The backscattering was 10 dB below the pre-breaking scattering at VV and 15 dB below at HH. The cross-polarized backscatter was stronger here indicating weak multiple scattering. The scattering from the complete surface agrees with that from the pre-breaking surface to within 1 or 2 dB at all incidence angles. The quasi-specular reflection from the pre-breaking bore therefore dominates the Bragg scattering from the post-breaking region.

A 3-D spilling-breaker scattering was synthesized from the 2-D scattering found from the individual measured profiles. A 3-D cross-section was found from the effective

profile width used, and the scattered fields were added coherently to give the full 3-D cross-section. The synthesized cross-sections showed good agreement with the numerical MLFMA cross-sections for both the complete surface and the pre-breaking surface. This results because the bore feature gives a reflecting surface that remains coherent over an electromagnetically large width. The post-breaking surface, however, is much more random, and loses coherence quickly. Therefore the synthesis from 2-D scattering was not accurate for any incidence angle.

The two-scale model was applied to the spilling-breaker profiles. When the complete surface was considered, the results depended strongly upon the wavenumber threshold used to filter the roughness into large- and small-scale components. This is most likely due to the steep bore feature on the pre-breaking section. The scattering of the post-breaking-only surface was less sensitive to the threshold. Reasonably accurate results (to within 3 dB) could be obtained with a threshold of $K_T = k/1.2$ at incidence angles ranging from 70° to 90° . This suggests that TSM may be used to obtain reasonable scattering coefficients at small grazing angles with surface that include only distributed-surface roughness with no steep features.

The plunging-breaker surface proved to have a scattering cross-section that was several dB larger than that of spilling breaker. This is because that the breaking is more energetic, giving several overturning that give larger cross-sections. HH is higher than VV by approximately 2 to 4 dB above 65° incidence. However, the large super events observed in the 2-D scattering from individual profiles were not evident in the 3-D scattering from the complete surface. The ratio of the cross-polarized to co-polarized backscattering was higher for the plunging breaker than it was for the spilling breaker.

This results since the plunging wave crest was more random overall, giving more multiple scattering.

As the complete plunging-breaker surface is unlikely to be realistic, a smaller surface was synthesized from only the first overturning. A deep null appeared in the VV scattering with this surface, giving a super event of 25 dB. The EGO model previously developed for 2-D scattering was extended to 3-D to treat this surface. 2-D EGO was first applied to the measured 2-D profiles to ensure its accuracy when applied to directly measured wave shapes. Several reflection points were identified on the 3-D surface, and EGO then applied. Accurate prediction of the VV null required that the parameters used in the EGO model be manually adjusted. However, the preliminary results show that the model may be useful in modeling the scattering from more realistic 3-D wave profiles that will be synthesized in the future.

BIBLIOGRAPHY

- [1] C. A. Balanis, *Advanced Engineering Electromagnetics*, New York: John Wiley and Sons, 1989.
- [2] F. T. Ulaby, R. K. Moore, and A. K. Fung, *Microwave Remote Sensing: Active and Passive*, vol.2, Norwood, Massachusetts: Artech House, 1986.
- [3] R. F. Harrington, *Field Computation by Moment Methods*, Malabar, Florida: Robert E. Krieger Publishing Company, 1968.
- [4] R. Bancroft, *Understanding Electromagnetic Scattering Using the Moment Method: A Practical Approach*, Artech House, Inc., 1996.
- [5] W. Weaver, Jr. Paul R. Johnston, *Finite Elements for Structural Analysis*, Englewood cliffs, New Jersey: Prentice-Hall, Inc., 1984.
- [6] A. G. Voronovich, *Wave Scattering from Rough Surfaces* (2nd edition), Heidelberg, Germany: Springer-Verlag, 1999.
- [7] M. J. Smith, E. M. Poulter, and J. A. McGregor, "Doppler Radar Measurements of Wave Groups and Breaking Waves," *J. Geophys. Res.*, vol. 101, pp.14269-14282, June 1996.
- [8] D. Holliday, L. L. Deraad, Jr. , and Gaetan J. St-Cyr, "Sea-Spike Backscatter from a Steepening Wave," *IEEE Trans. on Antennas and Propagation*, vol. 46, no.1, pp.108-113, Jan. 1998.
- [9] J. C. West, "LGA Sea-spike Backscattering from plunging Breaker Crests," *Geoscience and Remote Sensing Symposium, (IGRASS)*, vol.7, pp.3120-3122, 2000.
- [10] S. O. Rice, "Reflection of Electromagnetic Wave from Slightly Rough Surfaces," *Communications in Pure and Applied Mathematics*, vol. 4, no. 2, pp. 351-378, Aug. 1951.
- [11] J. W. Wright, "Backscattering from Capillary Waves with Application to Sea Clutter," *IEEE Trans. on Antennas and Propagation*, vol. 14, no. 6, pp.749-753, Nov. 1966.
- [12] J. W. Wright, "A New Model for Sea Clutter," *IEEE Trans. on Antennas and Propagation*, vol. 16, no. 2, pp.217-223, March 1968.

- [13] M. L. Burrows, "A Reformulated Boundary Perturbation Theory in Electromagnetism and Its Application to a Sphere," *Canadian Journal of Physics*, vol. 45, pp. 1729-1743, May 1967.
- [14] G. S. Brown, "Backscattering from a Gaussian-Distributed Perfectly Conducting Rough Surface," *IEEE Trans. on Antennas and Propagation*, vol. 26, no. 3, pp.472-482, May 1978.
- [15] J. T. Johnson, R. T. Shin, J. A. Kong, L. Tsang, and K. Pak, "A Numerical Study of the Composite Surface Model for Ocean Backscattering," *IEEE Trans. on Geoscience and Remote Sensing*, vol. 36, no. 1, pp. 72-83, Jan. 1998.
- [16] J. C. West, B. S. O'leary, and J. Klinke, "Numerical calculation of electromagnetic scattering from measured wind-roughened water surface," *Int. J. Remote Sensing*, vol. 19, no.7, pp.1377-1393, 1998.
- [17] J. C. West and S. J. Ja, "Two-Scale Treatment of LGA Scattering from Spilling Breaker Water Waves," *Radio Science*, in press.
- [18] B. G. Smith, "Geometrical Shadowing of a Random Rough Surface," *IEEE Trans. on Antennas and Propagation*, vol. 15, no.5, pp. 668-671, 1967.
- [19] M. I. Sancer, "Shadow Corrected Electromagnetic Scattering from a Randomly Rough Surface," *IEEE Trans. on Antennas and Propagation*, vol. 17, no.5, pp.577-585, 1969.
- [20] G. S. Brown, "Shadowing by Non-Gaussian Random Surface," *IEEE Trans. on Antennas and Propagation*, vol. 28, no. 6, pp.788-790, 1980.
- [21] J. C. West, "Effect of Shadowing on Electromagnetic Scattering from Rough Ocean Wavelike Surfaces at Small Grazing Angles," *IEEE Trans. on Geoscience and Remote Sensing*, vol. 35, no.2, pp.293-301, March 1997.
- [22] A. G. Voronovich and V. U. Zavorotny, "Theoretical Model for Scattering of Radar Signals in Ku- and C-bands from A Rough Sea Surface with Breaking Waves," *Waves in Random Media*, 11, pp. 247-269, 2001.
- [23] A. G. Voronovich, "Small-Slope Approximation for Electromagnetic Wave Scattering at A Rough Interface of Two Dielectric Half-Spaces," *Waves in Random Media*, 4, pp. 337-367, 1994.
- [24] S. T. McDaniel, "Acoustic and Radar Scattering from Directional Seas," *Waves in Random Media*, 9, pp.537-549, 1999.
- [25] G. Soriano, C. A. Guerin, and M. Saillard, "Scattering by Two-Dimensional Rough Surfaces: Comparison Between the Method of Moments, Kirchhoff and Small-Slope Approximations," *Waves in Random Media*, 12, pp.63-83, 2002.

- [26] D. H. Berman, "Simulation of Rough Interface Scattering," *J. Acoust. Soc. Am.*, vol. 89, no.2, pp.623-636, Feb. 1991.
- [27] E. I. Thorsos and S. L. Broschat, "An Investigation of the Small Slope Approximation for Scattering from Rough Surfaces. Part I. Theory," *J. Acoust. Soc. Am.*, vol. 97, pp.2082-2093, 1995.
- [28] S. L. Broschat and E. I. Thorsos, "An Investigation of the Small Slope Approximation for Scattering from Rough Surfaces. Part II. Numerical Studies," *J. Acoust. Soc. Am.*, vol. 101, pp.2615-2625, 1997.
- [29] T. Yang and S. L. Broschat, "A Comparison of Scattering of Scattering Model Results for Two-Dimensional Randomly Rough Surfaces," *IEEE Trans. on Antennas and Propagation*, vol. 40, no. 12, pp.1505-1512, Dec. 1992.
- [30] H. T. Ewe, J. T. Johnson, and K. S. Chen, "A Comparison Study of the Surface Scattering Models and Numerical Mode," Geoscience and Remote Sensing Symposium, IGARSS'01, IEEE 2001 International, vol.6, pp. 2692-2694, 2001.
- [31] H. Kim and J. T. Johnson, "Radar Images of Rough Surface Scattering: Comparison of Numerical and Analytical Models," *IEEE Trans. on Antennas and Propagation*, in press.
- [32] D. Winebrenner and A. Ishimaru, "Investigation of a Surface Field Phase Perturbation Technique for Scattering from Rough Surfaces," *Radio Science*, vol. 20, no. 2, pp. 161-170, Mar. -April 1985.
- [33] D. Winebrenner and A. Ishimaru, "Application of the Phase Perturbation Technique to Randomly Rough Surfaces," *J. Opt. Soc. Am.*, vol. 2, pp.2285-2294, 1988.
- [34] S. L. Broschat, "The Phase Perturbation Approximation for Rough Surface Scattering from a Pierson-Moskowitz Sea Surface," *IEEE Trans. on Geoscience and Remote Sensing*, vol. 31, no. 1, pp. 278-283, Jan. 1993
- [35] E. I. Thorsos, "The Validity of the Kirchhoff Approximation for Rough Surface Scattering Using a Gaussian Roughness Spectrum," *J. Acoust. Soc. Am.*, vol. 83, no.1, pp.78-92, 1988.
- [36] E. I. Thorsos and D. R. Jackson, "The Validity of the Perturbation Approximation for Rough Surface Scattering Using a Gaussian Roughness Spectrum," *J. Acoust. Soc. Am.*, vol. 86, no.1, pp.261-277, 1989.
- [37] E. I. Thorsos, "Acoustic Scattering From a "Pierson-Moskowitz" Sea," *J. Acoust. Soc. Am.*, vol. 88, no.1, pp.335-349,1990.
- [38] T. Chan, Y. Kuga, A. Ishimaru, and Charlie T. c. Le, "Experimental Studies of Bistatic Scattering from Two-Dimensional Conducting Random Rough Surfaces,"

- IEEE Trans. on Geoscience and Remote Sensing*, vol. 34, no.3, pp.674-680, May 1996.
- [39] M. F. Chen and A. K. Fung, "A Numerical Study of the Regions of Validity of the Kirchhoff and Small-perturbation Rough Surface Scattering Models," *Radio Science*, vol. 23, no.2, pp.163-170, 1988.
- [40] W. D. Burnside, C. L. Yu, and R. J. Marhefka, "A Technique to Combine the Geometrical Theory of Diffraction and the Moment Method," *IEEE. Trans. on Antennas and Propagation*, vol. 23, no.4, pp.551-558, July 1975.
- [41] J. C. West, J. Michael Sturm, and S. J. Ja, "Low Grazing Scattering Breaking Water Waves Using an Impedance Boundary MM/GTD Approach," *IEEE. Trans. on Antennas and Propagation*, vol. 46, no.1, pp.93-100, Jan. 1998.
- [42] J. M. Sturm and J. C. West, "Numerical Study of Shadowing in Electromagnetic Scattering from Rough Dielectric Surface," *IEEE Trans. on Geoscience Remote Sensing*, vol. 36, no.5, pp.1477-1484, Sept. 1998.
- [43] S. J. Ja, *Numerical Study of Microwave Backscattering from Breaking Water Waves*, Ph. D. Dissertation, Oklahoma State University, 1999.
- [44] S. J. Ja, J. C. West, H. Qiao, and J. H. Duncan, "Mechanisms of Low-Grazing-Angle Scattering from Spilling Breaker Water Waves," *Radio Science*, vol. 36, no.5, pp. 981-98, Sept.-Oct. 2001.
- [45] J. C. West, Z. Zhao, X. Liu, and J. H. Duncan, "LGA Scattering from Measured Breaking Water Waves: Extension to Jetting Surfaces," *Geoscience and Remote Sensing Symposium, 2001, IGARSS*, vol: 5, pp. 2454 -2456, 2001.
- [46] A. W. Glisson and D. R. Wilton, "Simple and Efficient Numerical Methods for Problems of Electromagnetic Radiation and Scattering from Surfaces," *IEEE Trans. on Antennas and Propagation*, vol. 28, no.5, pp.593-603, Sept. 1980.
- [47] S. M. Rao, *Electromagnetic Scattering and Radiation of Arbitrarily-Shaped Surfaces by Triangular Patch Modeling*, Ph. D. Dissertation, Univ. Mississippi, 1980.
- [48] S. M. Rao, D. R. Wilton, and A. W. Glisson, "Electromagnetic Scattering by Surfaces of Arbitrary Shape," *IEEE Trans. on Antennas and Propagation*, vol. 30, no.3, pp.409-418, May 1982.
- [49] A. W. Glisson, "Electromagnetic Scattering by arbitrarily shaped surface with impedance boundary conditions," *Radio Science*, vol. 27, no. 6, pp.935-943, Nov.-Dec. 1992.

- [50] T. Yu, B. Zhu, and W. Cai, "MIX-RWG Current Basis Function And Its Simple Implementation in MOM," *Microwave Symposium Digest, IEEE MTT-S International*, vol. 2, pp. 1105-1108, 2000.
- [51] P. C. Hammer, O. J. Marlowe, and A. H. Stroud, "Numerical Integration Over Simplexes and Cones," *Mathematical Tables and Other Aids to Computation*, vol. 10, pp. 129-139, Issue 55, July, 1956.
- [52] V. Rokhlin, "Rapid Solution of Integral Equations of Classical Potential Theory," *Journal of Computational Physics*, 60, pp.187-207, 1983.
- [53] V. Rokhlin, "Rapid Solution of Integral Equations of Scattering Theory in Two Dimensions," *Journal of Computational Physics*, 86, pp.414-439, 1990.
- [54] N. Engheta, W. D. Murphy, V. Rokhlin, and M. S. Vassilious, "The Fast Multipole Method (FMM) for Electromagnetic Scattering Problems," *IEEE Trans. on Antennas and Propagation*, vol. 40, no. 6, pp.634-641, Dec. 1992
- [55] V. Rokhlin, "Diagonal Forms of Translation Operators for the Helmholtz Equation in Three Dimensions," *Applied and Computational Harmonic Analysis*, vol. 1, pp.82-93, 1993.
- [56] R. Coifman, V. Rokhlin, and S. Wandzura, "The Fast Multipole Method for the Wave Equation: A Pedestrian Prescription," *IEEE Antenna and Propagation Magazine*, vol. 35, no. 3, pp.7-12, June 1993.
- [57] C. C. Lu and W. C. Chew, "Fast algorithm for Solving Hybrid Integral Equations," *IEE Proceedings-H*, vol. 140, no. 6, pp.455-460, Dec. 1993.
- [58] C. C. Lu and W. C. Chew, "A Multilevel Algorithm for Solving Boundary Integral Equations of Wave Scattering," *Microwave and Optical Technology Letters*, vol. 7, no.10, pp.466-470, July 1994.
- [59] J. M. Song and W. C. Chew, "Fast Multipole Method Solution Using Parametric Geometry," *Microwave and Optical Tech. Letters*, vol. 7, no.16, pp.760-765, Nov. 1993.
- [60] J. M. Song and W. C. Chew, "Multilevel Fast-Multipole Algorithm for Solving Combined Field Integral Equations of Electromagnetic Scattering," *Microwave and Optical Tech. Letters*, vol. 10, no. 1, pp.14-19, Sept. 1995.
- [61] J. M. Song and W. C. Chew, "Fast Multipole Method Solution of Three Dimensional Integral Equation," *Antennas and Propagation Society International Symposium, AP-S*, vol. 3, pp.1528-1531, 1995.
- [62] J. Song, C. C. Lu, and W. C. Chew, "Multilevel Fast Multipole Algorithm for Electromagnetic Scattering by Large Complex Objects," *IEEE Trans. on Antennas and Propagation*, vol. 45, no. 10, pp. 1488-1493, Oct. 1997.

- [63] R. Wagner, J. Song, and W. C. Chew, "Monte Carlo Simulation of Electromagnetic Scattering from Two-Dimensional Random Rough Surfaces," *IEEE Trans. on Antennas and Propagation*, vol. 45, no.2, pp.235-245, Feb. 1997.
- [64] M. F. Gyure and M. A. Stalzer, "A Prescription for the Multilevel Helmholtz FMM," *IEEE Computational Science & Engineering*, pp.39-47, July-Sept. 1998.
- [65] J. M. Song, C. C. Lu, W. C. Chew, and S. W. Lee, "Fast Illinois Solver Code (FISC)," *IEEE Antennas and Propagation Magazine*, vol. 40, no. 3, pp. 27-34, June, 1998.
- [66] L. Rossi, P. J. Cullen, and C. Brennan, "Implementation of a multilevel fast far-field algorithm for solving electric-field integral equations," *IEE Proc. Microw. Antennas Propag.*, vol. 147, no. 1, pp19-24, Feb. 2000.
- [67] N. Geng, A. Sullivan, and L. Carin, "Multilevel Fast-Multipole Algorithm for Scattering from Conducting Targets Above or Embedded in a Lossy Half Space," *IEEE Trans. on Geoscience and Remote Sensing*, vol. 38, no. 4, pp. 1561-1573, July, 2000.
- [68] L. Tsang, C. H. Chan, and K. Pak, "Monte Carlo Simulation of a Two-Dimensional Random Rough Surface Using the Sparse-Matrix Flat-surface Iterative Approach," *Electronics Letters*, vol. 29, no.13, pp.1153-1154, June, 1993.
- [69] L. Tsang and C. H. Chan, H. Pak, H. Sangani, "Monte-Carlo Simulations of Large-Scale Problems of Random Rough Surface Scattering and Applications to Grazing Incidence with the BMIA/Canonical Grid Method," *IEEE Trans. on Antennas and Propagation*, vol. 43, no.8, pp.851-859, Aug. 1995.
- [70] R. Barrett, et al, "Templates for the Solution of Linear Systems: Building Bocks for Iterative Methods", in Chapter 3, www.netlib.org/templates
- [71] J. T. Johnson, "A Numerical Study of Low-Grazing-Angle Backscatter from Ocean-Like Impedance Surfaces with the Canonical Grid Method," *IEEE Trans. on Antennas and Propagation*, vol. 46, no. 1, pp.114-120, Jan. 1998.
- [72] R. Devayya and D. J. Wingham, "The Numerical Calculation of Rough Surface Scattering by the Conjugate Gradient Method," *IEEE Trans. on Geoscience and Remote Sensing*, vol. 30, no.3, pp.645-648, May, 1992.
- [73] J. C. West and J. M. Sturm, "On Iterative Approaches for Electromagnetic Rough – Surface Scattering Problems," *IEEE Trans. on Antennas and Propagation*, vol. 47, no.8, pp.1281-1288, Aug. 1999.
- [74] R. L. Haupt and V. V. Liepa, "Synthesis of Tapered Resistive Strips," *IEEE Trans. on Antennas and Propagation*, vol. 35, no.11, pp.1217-1225, Nov. 1987.

- [75] Y. Oh and K. Sarabandi, "Improved numerical simulation of electromagnetic wave scattering from perfectly conducting random surfaces," *IEE Proc. Microw. Antennas Propag.*, vol. 144, no.4, pp256-260, Aug. 1997.
- [76] J. C. West, "Resistive Treatment of Edges in Numerical LGA Scattering From Rough Surfaces," *IEEE Antennas & Propagation Society International Symposium*, July 8-13, Boston, Massachusetts, pp508-511, 2001.
- [77] J. C. West, "On the control of Edge Diffraction in Numerical Rough Surface Scattering Using Resistive Tapering," submitted to *IEEE Antennas & Propagation Letters*.
- [78] L. B. Wetzel, "Electromagnetic Scattering from the Sea at Low Grazing Angles," in *Surface Waves and Fluxes* (G. L. Geernaert and W. L. Plant, eds.), vol. II-Remote Sensing, pp.109-171, Dordrecht, The Netherlands: Kluwer, 1990.
- [79] D. B. Trizna, "A Model for Brewster Angle Damping and Multipath Effects on the Microwave Radar Sea Echo at Low Grazing Angles," *IEEE. Trans. on Geosci. Remote Sensing*, vol.35, no.5, pp.1232-1244, Sept. 1997.
- [80] P. Wang, Y. Yao, and M. P. Tulin, "An Efficient Numerical Tank for Non-Linear Water Waves, Based on the Multi-Subdomain Approach with BEM.," *Int. J. Num. Meth. Fluids*, vol. 20, pp. 1315-1336, June 1995.
- [81] J. C. West and Mark A. Sletten, "Multipath EM Scattering from Breaking Ocean Waves at Grazing Incidence," *Radio Science*, vol. 32, no.4, pp.1455-1467, 1997.
- [82] J. C. West, "Ray Analysis of Low-Grazing Scattering from a Breaking Water Wave," *IEEE. Trans. on Geosci. Remote Sensing*, vol.37, no.6, pp.2725-2727, Nov. 1999.
- [83] J. C. West and Z. Zhao, "Electromagnetic Modeling of Multipath Scattering from Breaking Water Waves with Rough Faces," *IEEE. Trans. on Geosci. Remote Sensing*, vol. 40, no.3, pp. 583-592, March, 2002.
- [84] T. B. A. Senior and J. L. Volakis, "Generalized Impedance Boundary Conditions in Scattering," *Proceedings of the IEEE*, vol. 79, no.10, pp.1413-1420, Oct. 1991.
- [85] P. H. Y. Lee, et al, "X Band Microwave Backscattering from Ocean Waves," *Journal of Geophysical Research*, vol. 100, no. C2, pp.2591-2611, Feb. 1995.
- [86] W. J. Plant, " A Model for Microwave Doppler Sea Return at High Incidence Angles: Bragg Scattering from Bound, Tilted Waves," *J. Geophys. Res.*, vol. 102, pp. 21,131-21,146, Sept. 1997.
- [87] P. H. Y. Lee, et al, "What Are Mechanisms for Non-Bragg Scattering from Water Wave Surfaces?" *Radio Science*, Vol. 34, pp. 1123-1138, 1999.

- [88] J. H. Duncan, V. Philomin, H. Qiao, and J. Kimmel, "Formation of a spilling breaker," *Physics of Fluids*, vol. 6, no. 8, pp. 2560-2561, Aug. 1994.
- [89] M. F. Sultan and R. Mittra, "An iterative moment method for analyzing the electromagnetic field distribution inside inhomogeneous lossy dielectric objects," *IEEE Trans. on Microwave Theory and Techniques*, vol. 33, no.2, pp.163-168, Feb. 1985.
- [90] H. T. Chou and J. T. Johnson, "Formulation of forward-backward method using novel spectral acceleration for the modeling of scattering from impedance rough surfaces," *IEEE Trans. on Geosci. Remote Sensing*, vol. 38, Issue: 1, Part:2, pp.605-607, Jan. 2000.
- [91] J. C. West, "Low-Grazing-Angle (LGA) Sea-Spike Backscattering From Plunging Breaker Crests," *IEEE Trans. on Geosci. Remote Sensing*, vol. 40, no.2, pp.523-526, Feb. 2002.
- [92] J. B. Keller, "Geometrical theory of diffraction", *J. Opt. Soc. Amer.*, vol. 52, no.2, pp. 116-130, Feb. 1962
- [93] R. G. Kouyoumjian and P. H. Pathak, "A uniform geometrical theory of diffraction for an edge in a perfectly conducting surface," *Proc. IEEE*, vol. 62, pp. 1448-1461, Nov. 1974
- [94] D. R. Voltmer, *Diffraction by Doubly Curved Convex Surfaces*, Ph. D. Dissertation, Ohio State University, 1970.
- [95] W. L. Stutzman and G. A. Thiele, *Antenna Theory and Design*, 2nd edition New York: Wiley, 1998, pp.587-588 and pp. 619
- [96] D. A. McNamara, C. W. I. Pistorius and J. A. G. Malherbe, *Introduction to The Uniform Geometrical Theory of Diffraction*, MA: Artech House, 1990
- [97] A. Guissard and P. Sobieski, "An approximate model of the microwave brightness temperature of the sea," *Int. J. Remote Sens.*, vol. (8), pp. 1607-1627, 1987
- [98] J. C. West, "Application of SSA to Spilling Breaker Waves at Small Grazing Angles," to be submitted to the 2003 *International Geoscience and Remote Sensing Symposium*.
- [99] R. L. Jordan, "The Seasat-A Synthetic Aperture Radar System," *IEEE J. Oceanic Eng.*, vol. (5), Apr. 1980
- [100] R. L. Jordan, "The SIR-C/X-SAR Synthetic Aperture Radar System," *Proceedings of the IEEE*, vol. 79, no. 6, pp. 827-838, June 1991

VITA

Zhiqin Zhao 2

Candidate for the Degree of

Doctor of Philosophy

Thesis: NUMERICAL STUDY OF ELECTROMAGNETIC SCATTERING FROM
THREE-DIMENSIONAL WATER WAVES

Major Field: Electrical Engineering

Biographical:

Personal Data: Born in Hunan, the People's Republic of China, June 10, 1969, the son of Junhua Zhao and Manxiu Yin.

Education: Received Bachelor of Science and Master of Science degrees in Electrical Engineering from University of Electronic Science and Technology of China, Chengdu, China in July 1990 and March 1993, respectively. Completed the requirement for the Doctor of Philosophy degree in Electrical Engineering at Oklahoma State University in December 2002.

Professional Experience: Lecturer from June 1996 to June 1997, Associate Professor from July 1997 to December 1999, Department of Electronic Engineering, University of Electronic Science and Technology of China; Research Assistant at Department of Electrical and Computer Engineering, Oklahoma State University, January 2000 to December 2002.